博士論文

Compact photonic crystal cavities and microdisk InGaAs LEDs for on-silicon monolithic light sources

（シリコン上のモノリシック光源に向けた省面積フォトニック結晶共振器とInGaAs微小ディスクLEDの研究）

by

ケルマン ジョン オユイン
Jon Øyvind Kjellman

For the degree of
Doctor of Philosophy
Under the supervision of
Yoshiaki Nakano

Department of Advanced Interdisciplinary Studies
Graduate School of Engineering
The University of Tokyo

2014

Jon Øyvind Kjellman: *Compact photonic crystal cavities and microdisk InGaAs LEDs for on-silicon monolithic light sources* （シリコン上のモノリシック光源に向けた省面積フォトニック結晶共振器とInGaAs微小ディスクLEDの研究）, © 2014
SUPERVISOR:
Yoshiaki Nakano

ACKNOWLEDGMENTS

This dissertation is the culmination of almost four years at the University of Tokyo in Japan, 8000 km from home. It has been an adventure with ups and downs, joys and hardship with many lessons for me to treasure. But all adventures must come to an end and as I now move on, it is time to acknowledge those who have made the journey what it was.

First of all I would like to thank Professor Yoshiaki Nakano for accepting me into his group and giving me the opportunity to study under his supervision at such a distinguished institution as the University of Tokyo. The support given here is highly impressive. I would also like to thank his colleagues at the lab. Associate Professor Takuo Tanemura who has been a great support and his advice on theoretical and practical research matters has been invaluable particularly with regards to photonic integrated circuits and their design. Associate Professor Masakazu Sugiyama has been another important support particularly in the areas of growth.

In addition I must extend my thanks to Professor Shinji Yamashita and Professor Yasunobu Nakamura for serving on my PhD committee and offering valuable insight into which parts of my research required clarifications.

Furthermore, I would like to thank Assistant Professor Akio Higo, Assistant Professor Kentaro Watanabe, Assistant Professor Masanori Kubota and Assistant Professor Hassanet Sodabanlu for their research guidance and assistance in all technical matters. Their knowledge in processing and characterisation has been especially valuable. A special thanks to Assistant Professor Wang Yunpeng for his invaluable assistance with MOCVD operations and for his support and friendship throughout my years here.

The journey would not have been the same without my fellow students. A particular thanks goes to PhD students Wang Hongbo, Liu Cai and Manish Mathew with whom I have had many good times. Our exchange of ideas and perspectives has been enlightening both personally and professionally.

I also send my regards to Ayata Masafumi, Jakob Helander, Zhang Baifu, Yu Fujimoto, Watanabe Shota, Fu Yufeng, Watanabe Tohma and Okimoto Takuya whos personal friendship and

co-inciding research interests have fostered mutually beneficial ideas, thoughts and results. To the dozens of other members of Nakano, Sugiyama, Tanemura Laboratory, I also extend my gratidute for their support, friendship and assistance has been essential to complete this work.

Furthermore, for their assistance in all practical matters I thank the secretaries Tadokoro-san and Ui-san.

The Japanese government, represented by the Ministry of Education, Culture, Sports, Science and Technology and the Japanese embassy in Norway, also deserves my gratitude for financially supporting me. Without their scholarship I would not have had the opportunity to experience living and studying in Japan.

My entire family also deserves my thanks for I have their support and belief in me has been invaluable despite the vast distance separating us.

Finally, to my better half who I met during my stay here. We came here alone on the same mission and ended up taking this journey together. For your companionship and support through all the ups and downs and for your patience I thank you with all my heart.

ABSTRACT

Large scale systems integrating photonics and electronics at low cost is a future target of the semiconductor industry with potential application areas ranging from single chip gas sensors to sophisticated biological sensors, and to optoelectronic communication systems for distances down to the millimeter scale. Photonics/electronics convergence on a silicon platform is ideal since silicon has low substrate cost, mature processing technologies and dominates the electronics industry. photonic integrated circuits (PIC) implemented in silicon-on-insulator (SOI) is already an established technology with several key advantages such as strong confinement of light and low absorption at near-infrared (NIR) wavelengths useful for optical communication and sensing. However, due to silicon's indirect bandgap nature, silicon is not an efficient light emitter. Thus for truly convergent photonics/electronics systems, it is necessary to realize an efficient light source on silicon. Current solutions entering the market space rely on wafer- and chip-scale bonding of III/V materials onto silicon. These wafers are not homogeneous, bulk III/V material, but require epitaxial growth to realize functional optoelectronic devices such as lasers and photo-detectors. Intuitively, costs can be saved by removing the bulk III/V wafers from the equation and growing III/V material directly on silicon.

Previous works have established the growth of InGaAs microdisks on (111) oriented silicon by micro selective-area growth (μSAG) using metalorganic chemical vapor deposition (MOCVD). These disks have high crystalline quality and are grown with lateral overgrowth to diameters as large as 8 μm and with thicknesses as thin as 200 nm having been demonstrated. This makes these disks ideal for in-plane silicon photonics integration where the device layer is typically on the order of 200 nm to 300 nm. However, previous studies of these disks have focused only on growth with no demonstrations of functional electro-optical components. Due to the disks compact size, their direct band-gap nature and selective area growth, they are excellent candidates for future integration as on-silicon light sources.

In this dissertation, the first opto-electronic devices in the form of proof-of-concept NIR light emitting diodes (LEDs) are demonstrated. By introducing dimethylzinc (DMZn) and hydrogen sulfide (H_2S) into the growth, *p*- and *n*-doped regions can be formed, respectively. Room temperature electroluminescence (EL) is demonstrated from ensembles of 300 to 400 microdisks with *pin* junctions. The luminescence spectra has a maxima at 1.78 µm which is attributed to recombination in the doped regions. A local maxima at 1.65 µm is attributed to recombination in the un-doped region. As a first order approximation, this indicates a indium content of 47 %. The spectrum is broad banded with a full-width at half-maximum (FWHM) of 290 nm. This broadness is attributed to inter- and intra-disk variations in composition. The structure presented here was not optimized and for future applications, it is necessary to perform optimization with regards to reducing FWHM and supressing the long wavelength peak.

In addition to exhibiting EL, the microdisk ensembles were also found to detect infrared (IR) light. Under IR illumination with photon energies smaller than the silicon bandgap, a weak, but reproducible shift in the I-V characteristics indicating the generation of a photo current in the InGaAs disks. Again, further optimization of the growth and the device is required to improve performance.

For the realization of a future, hypothetical InGaAs-on-silicon laser, it is proposed that a cavity is formed using photonic crystals (PhCs). The advantage of using photonic crystal cavitys (PhCCs) is the possibility of high quality factors (Q-factors) and small mode volumes which for laser applications generally reduces the threshold current and improves modulation speed due to both the quantum mechanical Purcell effect as well as a pure reduction of the modal density. PhCCs also allows a high degree of field tailoring allowing a certain flexibility in the design of the mode profile.

However, despite potentially sub-cubic-wavelength mode volumes the total device area is generally large because a large number of PhC lattice periods are required to provide strong confinement. This makes it challenging to realize compact PhCCs. Within constraints determined by the hexagonal shape of the InGaAs-on-Si disks, a novel PhCC is proposed. Since few reports have been published on the challenges of compact PhCCs the problem is here approached in a manner which elucidates the general challenges of compact PhCCs in optically

thin slabs. This part of the research is carried out using well established computational methods such as finite-difference time-domain (FDTD) and plane wave expansion method (PWEM) for solving Maxwell's equations.

The cavity design is inspired by line defect heterostructure PhCCs. Such cavities can be optimized using a gentle confinement method where the field at the surface is shaped to have a Gaussian envelope in order to maximize the confinement to the slab by total internal reflection. This methodology has been applied to larger scale PhCCs achieving record high Q-factors on the order of 1×10^9, but here it is shown that the methodology can also be applied to compact cavities with diameters of less than 8 µm. For the case of an air suspended cavity, relatively high Q-factors of 75 100 are achieved. However, a strong dependence on the boundary is identified. A suboptimal boundary thickness between the outermost rows of holes and the surrounding cladding, can reduce the Q-factor by more than a factor of six. It is suggested that the optimum boundary width can be estimated using a simple Fabry-Pérot model. It is believed that this lesson on the importance of boundary optimization is general to all compact PhCCs.

One major advantage of the proposed design and optimization strategy is that the cavity can be designed for a specific resonance wavelength by using the computationally cheap PWEM. Deviation between the design wavelength and the resonance frequency calculated by FDTD was 0.5 %, or 8 nm when scaling the cavity to a C-band resonance wavelength of 1538 nm.

In conclusion, it has been shown that InGaAs-on-silicon disks do have potential as a future on-silicon light source. Although the LED structure was not optimized, clear EL could be observed at room temperature. Furthermore, it has been shown that it is possible to design a sophisticated PhCC within the constraints of the InGaAs microdisk geometry. This open ups the possibility of creating complementary metal-oxide-semiconductor (CMOS) compatible on-silicon lasers with in-plane coupling for advanced applications utilizing monolithic silicon photonics and electronics circuits.

RELATED PUBLICATIONS

JOURNAL PAPERS

[1] **Jon Øyvind Kjellman**, Masakazu Sugiyama, and Yoshiaki Nakano, "Near-infrared electroluminescence and photo detection in InGaAs p-i-n microdisks grown by selective area growth on Si (111)" Appl. Phys. Lett. **104**, 241103 (2014).

[2] **Jon Øyvind Kjellman**, Takuo Tanemura, and Yoshiaki Nakano, "Compact photonic crystal disk cavity optimized using the gentle confinement method and boundary design" Jpn. J. Appl. Phys. (2014), (accepted pending revisions) .

INTERNATIONAL CONFERENCES

[3] **Jon Øyvind Kjellman**, Takuo Tanemura, Masakazu Sugiyama, and Yoshiaki Nakano, "Monolithic InGaAs-on-Si micro-disk ensemble LED with peak luminescence at 1.58 µm" 26th *International Conference on Indium Phosphide and Related Materials* (2014) .

[4] **Jon Øyvind Kjellman**, Takuo Tanemura, and Yoshiaki Nakano, "Optimization of compact photonic crystal cavity using the gentle confinement method" *IEEE Photon. Soc. Summer Topical Meeting* (2013) pp. 44–45.

[5] **Jon Øyvind Kjellman**, Akio Higo, and Yoshiaki Nakano, "Design of photonic crystal cavity for hexagonal islands" *IEEE Photonics Conference* (2012) pp. 272–273.

[6] Yufeng Fu, Baifu Zhang, **Jon Øyvind Kjellman**, Takuo Tanemura, and Yoshiaki Nakano, "Numerical Study on Hollow Hexagonal InGaAs Microdisk Laser on Silicon" 26th *International Conference on Indium Phosphide and Related Materials* (2014) .

[7] Tohma Watanabe, **Jon Øyvind Kjellman**, Masakazu Sugiyama, and Yoshiaki Nakano, "Impact of doping

and mask pattern in selectively-grown InGaAs microdiscs on Si" 17th *International Conference on Metalorganic Vapor Phase Epitaxy* (2014) .

[8] Yu Fujimoto, Akio Higo, **Jon Øyvind Kjellman**, Shota Watanabe, Masakazu Sugiyama, and Yoshiaki Nakano, "Photoluminescence of InGaAs islands on Si (111) substrate grown using micro-channel selective-area MOVPE" Int. Conf. Opt. MEMS Nanophoton. , 200 (2012) .

CONTENTS

Abstract i

Related publications iv

List of Figures vii

List of Tables vii

Acronyms vii

1 INTRODUCTION 1
- 1.1 The case for silicon photonics 1
- 1.2 On-silicon light sources 3
- 1.3 This work 8

2 INGAAS-ON-SI 9
- 2.1 III/V on silicon 9
- 2.2 Challenge of on-silicon growth 9
- 2.3 Micro selective area growth 12
- 2.4 InGaAs-on-silicon 15
- 2.5 Disk geometry 21
- 2.6 CMOS compatibility 23

3 INGAAS-ON-SI NIR LED 25
- 3.1 Doping and morphology 25
- 3.2 Diode growth 29
- 3.3 Morphology 31
- 3.4 Device processing 33
- 3.5 IV characteristics 34
- 3.6 Electroluminescence 36
- 3.7 Photo detection 42
- 3.8 Band structure 44

4 PHOTONIC CRYSTALS 47
- 4.1 Definition 48
- 4.2 Photonic bands and band gap 50
- 4.3 Photonic crystal slab structure 52
- 4.4 Confinement and cavities 53
- 4.5 Q-factor 55
- 4.6 Computer modelling and simulations 56

5 PHOTONIC CRYSTAL CAVITY DESIGN AND OPTIMIZATION 59
5.1 Key considerations 59
5.2 The hybrid cavity 66
5.3 Simulation tools 68
5.4 Basic parameters 68
5.5 Lattice 68
5.6 Optimization 69
5.7 Optimization results 74
5.8 Wavelength predictability 78
5.9 Glass clad cavity 80
5.10 Mode competition 83
5.11 Output coupling 84

6 CONCLUSION 88
6.1 Future work 90

A FABRICATION 92
A.1 Growth template fabrication 92
A.2 Growth template cleaning 94
A.3 Ensemble diode processing 95

BIBLIOGRAPHY 98

LIST OF FIGURES

Figure 1 SEM images of InGaAs on silicon growths. 6
Figure 2 Artists vision of future InGaAs-on-Si platform 7
Figure 3 Map of lattice constant and bandgap energy for selected III/V semiconductors 10
Figure 4 SEM of growth mask for selective area growth 12
Figure 5 Multiple nuclei forming within a growth window creating a grain boundary and polycrystalline growth. 13
Figure 6 Extinction of threading defect in selective area growth. 13
Figure 7 The fundamental steps of epitaxial lateral overgrowth. 14
Figure 8 Cross section of the growth of InGaAs on (111) silicon 16
Figure 9 Growth mask layout. 21
Figure 10 Geometrical parameters of InGaAs disks 22
Figure 11 SEM image of polycrystalline growth. 22
Figure 12 Example confocal image 27
Figure 13 Scatter plots of disk diameter vs thickness 28
Figure 14 Cross section of (a) *pin* structure and (b) *pn* structure. 31
Figure 15 Distribution of disk geometry for *pin* disks. 32
Figure 16 Cut-through model of fabricated structure (not to scale.) 34
Figure 17 IV characteristics for (a) *pn* disk ensembles and (b) *pin* disk ensembles. 35
Figure 18 SEM image of short between gold electrode and the silicon substrate 35
Figure 19 Schematic of setup for measurement of InGaAs electroluminescence. 36
Figure 20 Electroluminescence spectrum for various injection currents. 37

Figure 21 Room temperature electroluminescence from three distinct *pin* disks within the same ensemble. 38
Figure 22 Integrated intensity (circles) as a function of current for sample at room temperature and sensor. 40
Figure 23 Fit of relative quantum efficiency as a function of current. 43
Figure 24 I-V characteristics 44
Figure 25 Following the dashed path the disk cross section is simplified into a one-dimensional structure. 45
Figure 26 Sketch of band structure of ideal InGaAs *pn*-junction. 45
Figure 27 Sketch of band structure of ideal InGaAs *pin*-junction. 46
Figure 28 Opal gemstones owe their colors to natural photonic crystal structures. 47
Figure 29 Different dimensionality for PhC structures. 49
Figure 30 2D hexagonal PhC lattice geometry. 49
Figure 31 Example band diagram with 51
Figure 32 TE-like band structure for hexagonal slab PhC. 53
Figure 33 Example photonic crystal cavities cavity in a hexagonal lattice 54
Figure 34 Cut-through sketch of the possible active region designs. 61
Figure 35 Schematic cavity model. 67
Figure 36 Algorithm for gentle confinement method on line-defect hetero structures. 71
Figure 37 Simplified Fabry-Pérot model of the boundary region. 72
Figure 38 Q-value as a function of tapering and boundary width. 74
Figure 39 Total Q-factor decomposed into $Q_{\parallel}$ and $Q_{\perp}$. 75
Figure 40 Logarithm of the optical intensity at the surface of the cavity. 77
Figure 41 k-space distribution of field at the cavity surface. 79
Figure 42 Relative resonance frequency as a function of tapering. 80

Figure 43 Attenuation as a function of line defect width. 81
Figure 44 Q-factor relations in glass clad cavity. 82
Figure 45 Full spectrum for $H_{\perp}$ field in high-Q cavity. 84
Figure 46 Waveguide coupling concept 85
Figure 47 Field distribution when coupling into two waveguides. 85
Figure 48 Decomposed Q-factor and accumulated coupling efficiency to six output ports. 86

LIST OF TABLES

Table 1 Thermal expansion coefficients for the $In_{1-x}Ga_xAs$ ternary system. 10
Table 2 Common growth conditions for thermal cleaning, nucleation and InAs growth. 19
Table 3 Mask layout parameters. 21
Table 4 Growth condition for morphology investigation. 26
Table 5 Morphology statistics 29
Table 6 Growth condition for *pn* and *pin* diodes. 30
Table 7 Summary of statistics for ten arbitrarily selected areas on as-grown *pin* samples. 32
Table 8 Geometrical constraints of cavity. 60
Table 9 Simulation parameters for glass-clad cavity. 81
Table 10 Oxidation settings 93

Table 11 Etch condition for Anelva L-201D-SLA ICP-RIE 94

ACRONYMS

1D	one-dimensional
2D	two-dimensional
3D	three-dimensional
µSAG	micro selective-area growth
BHF	buffered hydrofluoric acid
BOX	buried oxide
CMOS	complementary metal-oxide-semiconductor
cw	continuous wave
DFT	discrete Fourier transform
DI	de-ionized water
DMZn	dimethylzinc
DWDM	dense wavelength division multiplexing
EB	electron beam
ELO	epitaxial lateral overgrowth
EL	electroluminescence
EQE	external quantum efficiency
FCA	free-carrier absorption
FDTD	finite-difference time-domain
FP	Fabry-Pérot
FWHM	full-width at half-maximum
H_2S	hydrogen sulfide
ICP-RIE	inductively coupled plasma reactive-ion etch
IPA	isopropyl alcohol
IR	infrared
IQE	internal quantum efficiency
LED	light emitting diode
MIR	mid-infrared
MOCVD	metalorganic chemical vapor deposition
MOSFET	metal-oxide-semiconductor field-effect transistor
MQW	multiple quantum wells
NIR	near-infrared
OE	optoelectronic
OEM	original equipment manufacturer
PBG	photonic bandgap
PhC	photonic crystal
PhCC	photonic crystal cavity

PhCS	two-dimensional photonic crystal slab
PIC	photonic integrated circuits
PWEM	plane wave expansion method
QD	quantum dot
QW	quantum well
RT	room temperature
SEM	scanning electron microscopy
SOG	spin-on-glass
SOI	silicon-on-insulator
SRH	Schockley-Read-Hall
SRS	stimulated Raman scattering
TBAs	tertiarybutyl arsine
TBP	tertiarybutyl phosphine
TE	transverse electric
TED	transmission electron diffraction
TM	transverse magnetic
TMGa	trimethylgallium
TMIn	trimethylindium
TPA	two photon absorption
WDM	wavelength division multiplexing
XRD	x-ray diffraction

1 INTRODUCTION

Monocrystalline silicon is widely considered an attractive substrate for photonic devices due to low cost, mature manufacturing and excellent material properties [10–15]. However, in order to fully leverage the benefits of mature silicon complementary metal-oxide-semiconductor (CMOS) manufacturing processes and the low substrate costs the challenges presented by silicon's indirect bandgap must be overcome. First and foremost, the indirect nature of silicon's band structure prevents efficient light generation. Pure silicon sources utilizing interband transitions have reported efficiencies of 1% or less [16–18].

1.1 THE CASE FOR SILICON PHOTONICS

There are several reasons why silicon is such an attractive platform for optoelectronic (OE) applications. The primary reason being economics. Silicon is cheap and abundant. It accounts for 28% of Earth's crust by mass [19] and can be refined into large ingots of extremely high purity ($> 99.9999999\%$). Due to the development in the integrated electronics industry since the 1960's, silicon wafers are readily obtainable at low cost. These wafers are also available in large sizes which enables a large number of devices to be fabricated simultaneously, driving cost down.

At the same time monocrystalline silicon has quite favorable material properties for photonics such as high mechanical strength and a high refractive index of $n_{Si} \approx 3.5$ [20]. High quality oxide layers with refractive index of $n_{SiO_2} \approx 1.45$ are also readily formed by oxidation resulting in a high index contrast. This enables strong confinement of light making silicon highly suitable for photonic integrated circuitss (PICs)[10–15]. The formation of native oxides has also enabled the creation of high quality silicon-on-insulator (SOI) substrates [21] which are highly suitable and widely employed for silicon PICs [22].

Currently, CMOS fabrication technology is being used to fabricate silicon PICs, leveraging decades of process experience from the CMOS industry[23–25]. Currently, the technology has matured to a point where silicon photonics foundry services

are readily available[26–31]. These CMOS and CMOS-derived processes are also generally cheap as is evident by the many cheap consumer electronics devices incorporating silicon electronics micro-processors. This further compounds the economic argument for silicon photonics.

Another attraction of silicon photonics is the potential for opto-electronic convergence. Today, we are surrounded by opto-electronic systems. Common examples include optical disc storage such as DVD and Blu-ray, LED lighting, the internet (i. e. fiber optical telecommunication), bar-code readers, gas sensors etc. All these systems, however, are built from discreet optical and electronic components. The creation of systems by combination of discreet components naturally adds cost and complexity. Convergence of optical and electronic technologies are therefore desired in order to reduce complexity and cost. Imagine for instance the convenience of a single chip with a tunable infrared (IR) light source, diffraction gratings, optical detectors and digital circuitry for signal processing. It could be used as a low cost spectrometer for gas analysis or biological sensing.

Furthermore, a major application area is within optical communication. Optical communication has a history dating back to 1880 and the invention of the photophone by Alexander Graham Bell. The first practical applications of optical communication arrived in the 1970s with the first non-experimental optical communication system being installed in 1975 for the Dorset Police. In the following decade, the first transatlantic fiber-optical cables was installed, carrying unprecedented amounts of communication between the continents[32]. Ever since, there's been a race to increase bandwidth, reduce cost and to bring the advantages of optical communication into new areas. In the last decade, optical networking has reached all the way into peoples homes [33] and into the data centers for inter-rack communication [34, 35] with optical backplanes for intra-rack communication appearing as the next logical step due to reduced power consumption and simplified cabling. [36–38]

Moving beyond rack-level optical communication and into the sub-metre scale, optical communication is presently being investigated as a high-bandwidth alternative for board-to-board communication. [39, 40] Looking further ahead, research on chip-to-chip communication appears promising. [39] If chip-to-chip communication is proven viable, many believe that the next frontier for optical communication is on-chip commu-

nication [41]. The trend is for CPU designers to increase the number of CPU cores, but to do so, ever higher bandwidths are required. This could soon be the next frontier for photonic integrated circuits.

1.2 ON-SILICON LIGHT SOURCES

The major issue preventing silicon photonics from reaching its potential lies with silicon's band structure. Silicon has an indirect bandgap which significantly reduces the efficiency of light generation. Indeed, the highest reported efficiencies for silicon electroluminescence at wavelengths longer than 1100 nm—where the photon energy is smaller than the silicon bandgap energy and absorption is weak—are on the order of 1% [16, 18]. With the challenges of silicon's band structure one must either modify the bandgap or rely on some other mechanism than band-to-band recombination in order to achieve efficient light generation.

There are several approaches to realize light sources on silicon. This section will present three common approaches and their current state of development. The first approach is pure silicon lasers which through various methods try to overcome the indirect bandgap nature of silicon. Next there are hybrid solutions where III/V active materials are bonded to silicon. These two technologies will be introduced briefly for comparison with the subject matter of this dissertation. Finally, there is monolithic integration where materials—primarily III-I/V compounds—are grown directly on silicon. This will be presented in somewhat more detail.

1.2.1 *Si lasers*

As mentioned, silicon has an indirect bandgap which is unsuitable for efficient light generation. Thus, to achieve efficient light generation, one must either modify the bandgap or rely on some other mechanism than band-to-band recombination.

A completely native approach to light amplification and lasing in silicon is through a process known as stimulated Raman scattering. Raman scattering is a non-resonant process where a scattered photon emerges at a slightly different frequency than the incident photon. The difference in energy between the incident and scattered photon corresponds to a change in energy of rotational and/or vibrational states in the material. If the en-

ergy of the scattered photon is larger than the incident photon's energy, it is called Stokes scattering while the opposite case is called anti-Stokes scattering. [42, Chapter 13.5]

In stimulated Raman scattering (SRS), two photons are required; one pump photon of frequency ν_p and one signal photon of frequency $\nu_s < \nu_p$. When SRS occurs, the signal photon stimulates Raman-Stokes scattering in a fashion analogous to stimulated emission. As with stimulated emission, this process can be used to achieve amplification and lasing.

SRS in silicon for lasing and amplification has been a research target since it's first observations in silicon waveguides by Claps et al. [43, 44]. The first silicon Raman laser was demonstrated in 2004 [45] integrating a silicon waveguide in a fiber loop cavity. The main issue of silicon Raman lasers is low efficiency due to free-carrier absorption (FCA) caused by two photon absorption (TPA) carriers. This first demonstration overcame this by using pulsed excitation. To achieve continuous wave excitation, reverse-biased *pin* junctions were introduced to sweep away carriers, reducing FCA [46, 47]. Further developments reduced the threshold power to a few mW [48] while recent research has shown a photonic crystal (PhC) silicon Raman laser with $1\,\mu W$ threshold. [49] This PhC device was relatively compact with micrometer scale size and did not require a reverse biased *pin* junction to achieve room temperature (RT) continuous wave (cw) lasing.

Yet, the fact remains that SRS is an all optical scattering process and thus an external, optical pump source is always required. Thus, it arguably does not represent the ultimate micro or nano laser.

1.2.2 *Hybrid integration*

III/V lasers bonded onto silicon has been an area of research for more than two decades, with several room temperature cw lasers demonstrated in the 1990's [50, 51]. These early attempts merely used silicon as a host substrate without implementing devices in the silicon. Efficient coupling to silicon waveguides was realized with a novel hybrid silicon laser in 2005 by Park et al. [52] and in the last decade, several other groups have published on various implementations of hybrid silicon lasers [53–56].

The principle of the hybrid silicon laser is to bond III/V chips or wafers onto a processed silicon photonic circuit. The

resonant cavity is usually implemented in the silicon, but engineered such that the mode overlaps with the bonded III/V material which provides optical gain. Several topologies have been investigated including ring lasers, racetrack lasers, Fabry-Pérot (FP) lasers and DFB lasers.

This technology is to date, the most successful technology for coherent on-silicon light sources and is now being used in commercially available products. Intel, for instance, offers board-to-board interconnect modules to original equipment manufacturers (OEMs).

The main advantage of hybrid silicon lasers is that it is a rapidly maturing technique with commercial applications already being used. It relies on familiar III/V and Si processing technologies with minor adjustments. Furthermore, the epitaxial know-how from the growth of "conventional" III/V semiconductor lasers is available and thus no exotic growth techniques are necessary.

The main disadvantage is the bonding step. For a hybrid laser, three steps are required:

1. III/V epitaxial growth
2. III/V on Si bonding
3. Device fabrication

This is one step more than for monolithic integration by epitaxial or hetero-epitaxial growth where the two steps are simply:

1. III/V epitaxial growth
2. Device fabrication

However, the question of economics is perhaps more nuanced. For instance, the III/V epitaxial growth may have lower yield than III/V growth on silicon due to silicon being available as larger wafers reducing edge area and increasing throughput. On the other hand, chip bonding is a viable option which may reduce overall material consumption if the III/V substrate can be reused, but it requires much more advanced alignment and time as each chip must be placed individually. Furthermore, there may not be a cost effective way to integrate III/V-on-Si growth into a CMOS or even silicon photonics process. As such, the question of economics for hybrid vs. monolithic integration is still very much open.

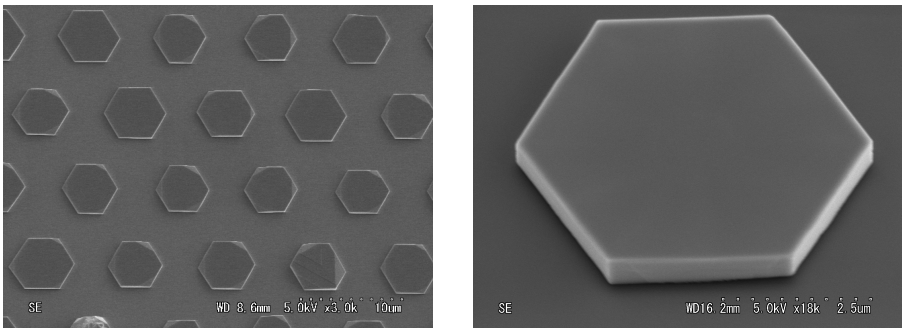

(a) (b)

Figure 1: SEM images of InGaAs on silicon growths. (a) Multiple disks are grown simultaneously in a regular lattice. (b) Each disk has a large diameter-to-height ratio.

1.2.3 *Monolithic integration*

One highly promising approach to solve the problem of on-silicon light sources is monolithic integration of group IV or III/V materials on silicon. Several approaches exists, with bonding of III/V epitaxial substrates on silicon gaining traction in industry [53, 57]. However, monolithic growth of group IV or III/V materials on silicon would simplify processing, by removing the bonding step and is therefore in principle preferred.

Again there are several approaches. Germanium has been successfully applied for photo detectors [58] and there has been some recent progress in Ge-on-Si lasers [59], but since germanium is also an indirect bandgap semiconductor efficiency remain low. Research from the 1990's produced some promising results for III/V-on-Si including multiple quantum well lasers [60]. These, however, required very thick buffer layers to reduce defects which would make integration with silicon photonics challenging. More recently, the buffer layer thickness has been reduced by the use of off-cut substrates [61–63]. However, integrating such bulk growth with silicon photonics remains elusive. Other groups have reported promising GaAs/InGaAs nano-needle growth on silicon, demonstrating both optically pumped lasing [64] as well as electrically pumped light emitting diodes (LEDs) [65]. Again, however, integration with silicon photonics has not been demonstrated.

Previous research at the laboratory where this dissertation was written has also developed an interesting technology for monolithic III/V-on-silicon integration. Initially intended for high speed electronics, growth of InGaAs micro-disks on (111)

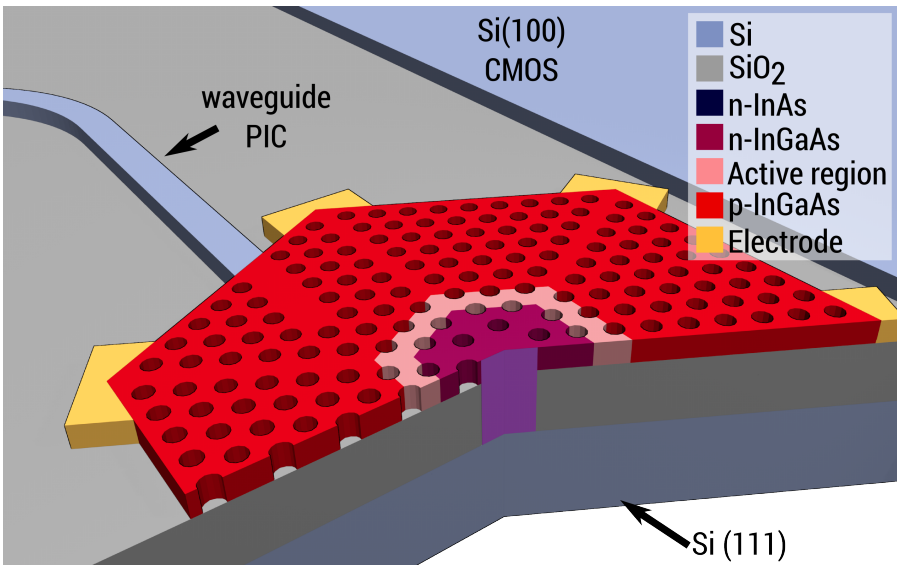

Figure 2: Artists vision of future device with photonic crystal laser implemented in InGaAs disk grown on (111) silicon and coupled to silicon photonics circuits and integrated with CMOS electronics circuits.

oriented silicon has been demonstrated. [66–74]. The disks are grown by metalorganic chemical vapor deposition (MOCVD) micro selective-area growth (μSAG). An scanning electron microscopy (SEM) image of such an InGaAs microdisk is shown in fig. 1. The area surrounding the disks is SiO_2 which serves as a growth mask and covers the underlying (111) silicon. The disks are grown through channels in this mask and by utilizing lateral overgrowth, relatively large disks with high diameter-to-height aspect ratios are achieved.

These disks have shown excellent crystal quality and promising optical qualities. One future vision for these disks is to realize a laser cavity within them and to allow them to couple into a silicon photonics device layer. Such a vision is illustrated in fig. 2 where the InGaAs disks are integrated with a SOI substrate where silicon photonics circuits and integrated with CMOS electronic circuits. Such monolithic systems could enable unprecedented photonics-electronics convergence. Besides short-range optical communication, this technology could enable single chip gas and medical sensors monolithically integrating measurement and analysis circuitry.

1.3 THIS WORK

This dissertation will contribute to the on-going research and development of on-silicon light sources in two ways. One is the demonstration of a near-infrared (NIR) LEDs based on μSAG of InGaAs micro-disks on (111) oriented silicon. The second is the design and optimization of a novel compact photonic crystal cavity (PhCC). The purpose of this design is to explore the possibility of creating an in-plane laser with high quality factor and low mode volume within the limited area presented by the InGaAs disks. If realized, the combination of such a laser and silicon photonic PICs should enable the creation of monolithically integrated, single chip solutions for applications such as gas sensing, biosensors, optical ranging, inter- and intra-chip communication etc.

This dissertation is divided into two main part related to on-silicon light sources. The first part concerns the growth and characterisation of *p-i-n* InGaAs disks on silicon. In this part, light detection and, for the first time, generation is demonstrated. This establishes InGaAs as a potential candidate for future monolithic on-silicon light sources and detectors.

The second parts takes the geometrical limitations of the InGaAs-on-silicon disks and explores how a novel, compact PhCC can be implemented in this structure. The goal is to provide a viable design for a InGaAs-on-silicon photonic crystal laser for short range communication. This study of a PhCC also provides some general conclusions related to compact photonic crystal cavities which should be useful to the PhCC-community.

This dissertation will present two important building blocks for the future realization of an InGaAs-on-silicon laser at telecommunication wavelengths. The first part will present the growth and characterization of *p-i-n* InGaAs-on-silicon light emitting diodes. The second part will then thoroughly investigate the design and optimization of a novel, compact PhCC. This cavity is specifically designed for applications where the area is limited such as in the case of InGaAs discs on silicon. These parts are tied together by considering the limitations the InGaAs discs impose on the design as well as considerations for future PhC laser performance.

2 INGAAS-ON-SI

In the next chapter, the growth of InGaAs-on-silicon NIR LEDs will be investigated and discussed. To facilitate the understanding of the growth-techniques this chapter will introduce certain key concepts as well as review the previous developments in this field. For completeness' sake, the last section of this chapter briefly addresses the issue of CMOS compatibility.

2.1 III/V ON SILICON

III/V materials are materials consisting of one or more elements from group-III (group 13 in the periodic table, also known as the Boron group) and one or more elements from group-V (group 15 in the periodic table, also known as the nitrogen group.) Crystalline III/V compounds can be synthesized with high quality using various deposition techniques and have favourable optical and electronic properties. Figure 3 shows the lattice constant, bandgap energy and corresponding emission wavelength for a selection of common III/V semiconductor compounds. As the illustration shows, the bandgap energy covers a wide range with corresponding wavelengths ranging from visible light into MIR-wavelengths. This flexibility in bandgap engineering combined with the fact that most of the compounds are direct bandgap makes III/V compounds an excellent choice for opto-electronic components such as amplifiers, LEDs and laser diodes.

2.2 CHALLENGE OF ON-SILICON GROWTH

The primary challenge of growing III/V materials on silicon is lattice mismatch. For instance, $In_{0.47}Ga_{0.53}As$ has a bandgap of 0.80 eV which corresponds to the very common telecommunication wavelength 1.55 µm and a lattice constant of 5.844 Å. This lattice constant is 7.6 % larger than the 5.431 Å of silicon. This represents a significant lattice mismatch which introduces stress and strain which can cause wafer warping and lattice defects.

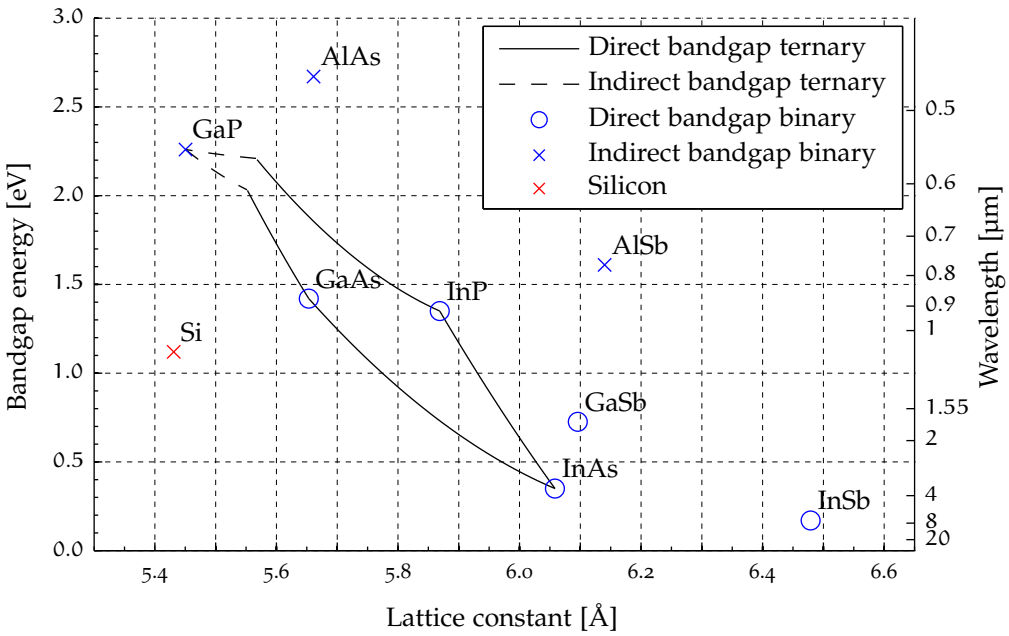

Figure 3: Map of lattice constant and bandgap energy for selected III/V semiconductors with silicon marked for comparison. The indicated lines show the transition for the four possible ternary combinations of the elements In, Ga, As and P. The quaternary $In_{1-x}Ga_xAs_yP_{1-y}$ has values inside the region bounded by these lines.

Table 1: Thermal expansion coefficients for the $In_{1-x}Ga_xAs$ ternary system.

	α_T
InAs	$4.52 \times 10^{-6}\,K^{-1}$
GaAs	$5.73 \times 10^{-6}\,K^{-1}$
$In_{1-x}Ga_xAs$	$(4.52 + 1.21x) \times 10^{-6}\,K^{-1}$

Another issue is mismatch in thermal expansion coefficients. As a material heats and cools it generally expands and contracts. The rate of this expansion/contraction is material dependent and is quantified by the thermal expansion coefficient α_T in units K^{-1}. For illustrative purposes, assume that α_T for $In_{1-x}Ga_xAs$ follows Vegard's law and varies linearly with the gallium fraction x between the binary compounds InAs ($x = 0$) and GaAs ($x = 1$). Using the numbers in table 1, $In_{0.47}Ga_{0.53}As$ then has $\alpha_T = 5.16 \times 10^{-6}\,K^{-1}$. This value is almost twice the value of $2.6 \times 10^{-6}\,K^{-1}$. This extreme mismatch is highly undesirable as even small thermal changes will rapidly build up stress in the epitaxial layer. This is a severe issue as growth techniques such as MOCVD generally require substrates to be heated to several hundred degrees. As a consequence, the inevitable cool-down after growth will generally cause stress to build up. This can lead to wafer warping, cracking and induce lattice dislocations. In the case of light generating devices there is also an issue of non-negligible heating during operation which—if not properly accounted for—would cause stress to build up which can induce strain and degradation of the crystal quality.

There are other issues such as silicon diffusion into the III/V lattice, but these are secondary to the two main issues mentioned here.

Mitigation of the mismatch in lattice constant and thermal expansion can be achieved by various approaches. The most straight forward approach is to introduce buffer layers of intermediate materials that have a lattice constant and thermal expansion constant between that of silicon and the desired III/V compound. This buffered approach has been previously applied to create III/V lasers on silicon using III/V buffer layers [60–63] and $Ge/Si_{1-x}Ge_x$ buffer layers [75, 76].

One major limitation of this approach is often that it requires thick buffer layers. For instance, Sugo et al. [60] demonstrated InGaAs/InGaAsP multiple quantum wells (MQW) lasers grown on silicon using a combination of GaAs, super lattice and InP buffer layers. The thickness of these buffer layers added up to 15 µm. This makes it hard to envision practical integration with silicon photonics. However, more recent approaches [61, 63] combined silicon (100) substrates 4° off-cut towards (111) with ~2 µm buffer layers which could potentially enable monolithic silicon photonics integration as this buffer thickness is on the order of SOI buried oxide (BOX) layers used for silicon photonics.

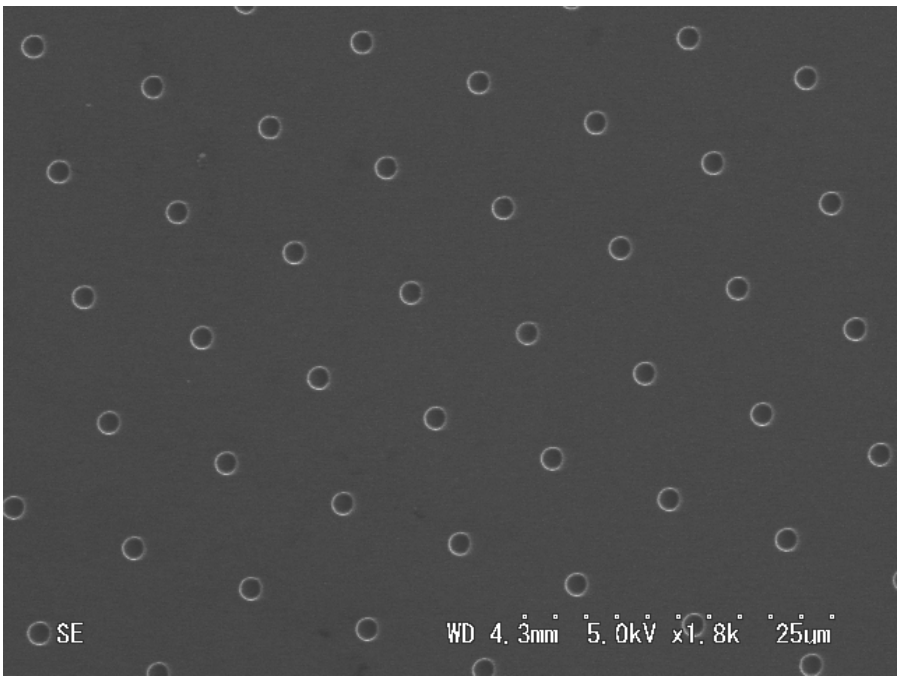

Figure 4: SEM birds-eye-view of growth mask for selective area growth. Bulk surface is SiO_2 with etched holes exposing an underlying silicon surface.

Alternative techniques for overcoming the lattice mismatch use patterning or structuring of the substrate on the nano- or micrometer-scale. Generally this is done to reduce the effective area over which stress can accumulate, greatly mitigating the negative effects of the lattice mismatch issue. There are several variations on this approach and it can be used to achieve both thin/thick-film growth or nano-wire growth[0]. For the InGaAs-on-silicon growth discussed in this dissertation, micro selective-area growth (μSAG) is used.

2.3 MICRO SELECTIVE AREA GROWTH

micro selective-area growth is a technique for growing materials of high crystal quality on lattice mismatched substrates. In this technique the substrate (e. g. silicon) is covered by a mask with micrometer-scale growth windows to expose only selected areas of the underlying substrate. An example with an SiO_2 mask covering silicon with circular growth windows is illustrated in fig. 4. By choosing the correct mask material, nucleation occurs only on the exposed substrate and not on the mask material. In the case of both InGaAs and InAs on silicon it has been found that nucleation will predominantly occur in

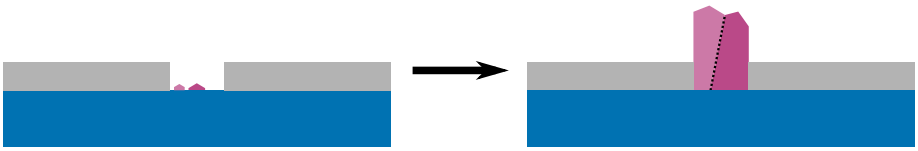

Figure 5: Multiple nuclei forming within a growth window creating a grain boundary and polycrystalline growth.

Figure 6: Extinction of threading defect in selective area growth.

the exposed silicon growth windows and not on the SiO_2 surface as long as the pitch is less than twice the surface diffusion length of the precursors [66, 77].

First, the primary advantage over plain selective area growth (i.e. not *micro* sized areas) is that if the growth window is small enough then, on average, only a single nucleus is formed in each growth window. This avoids the formation of grain boundaries where the growth from two or more nuclei meets. This greatly reduces threading defects and polycrystalline growth and ensures a defect free monocrystalline growth. Figure 5 illustrates how a grain boundary can form when there are two nuclei in a growth window. Furthermore, for high vertical growths the µSAG (and plain selective area growth) approach can ensure that threading dislocations are extinguished. In a pillar, threading dislocation can only propagate until it meets the growth window edge as illustrated in fig. 6. This greatly reduces defect densities at the extremities of the growth.

2.3.1 *Epitaxial lateral overgrowth*

If an area larger than the growth channel area is required, then epitaxial lateral overgrowth (ELO) is an option. The process is illustrated in fig. 7 where on a patterned substrate (fig. 7a), nucleation is initiated (fig. 7b) followed by filling out the growth window (fig. 7c). The defining characteristic of ELO is the occurrence of lateral growth (fig. 7d.) Lateral growth is achieved when the reactor conditions enable horizontal growth on the

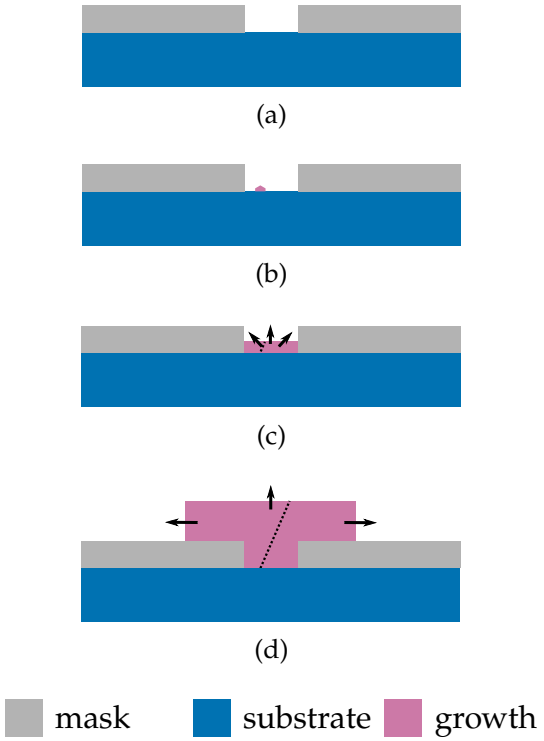

Figure 7: The fundamental steps of epitaxial lateral overgrowth: (a) preparation of patterned substrate, (b) nucleation, (c) growth window fill-out, and (d) lateral overgrowth. The dashed line shows how any potential threading defects are extinguished leaving the overgrown regions defect free.

vertical crystal facets in addition or exclusion to vertical growth on the horizontal facets. What these conditions are depends on the physical/chemical properties of the substrate and reactor atmosphere. μSAG lateral overgrowth gives a cross-sectional geometry as sketched out in fig. 7d. This figure also illustrates how any potential threading dislocations are extinguished near the center of such an overgrowth enabling defect free edge regions to be formed.

2.4 INGAAS-ON-SILICON

The interest in InGaAs-on-silicon was spurred by its suitability as a material for III/V metal-oxide-semiconductor field-effect transistor (MOSFET) integration on silicon due to InGaAs's suitable band gap and high electron mobility. To achieve thin layers for integration with SOI based CMOS technology nodes, the use of ELO was proposed by Hoshii et al. [66, 67]. These initial reports demonstrated successful formation of InGaAs films on (111) Si using MOCVD ELO. Furthermore, nucleation and growth of InGaAs was found to have good selectivity for growth on silicon over SiO_2 making SiO_2 the material-of-choice for growth mask. These reports also showed empirically that to achieve good crystal quality locally (111) oriented silicon was strongly preferred compared to (100) silicon. InGaAs on (111) Si showed flat surfaces locally while growth on (100) Si had rough surfaces and showed poor crystal quality as determined by x-ray diffraction (XRD). This research also established circular holes arranged in a hexagonal lattice as suitable for the growth of InGaAs disks without any grain boundaries [67].

These initial investigations used trimethylindium (TMIn), trimethylgallium (TMGa) and tertiarybutyl arsine (TBAs) precursors during growth in order to form $In_xGa_{1-x}As$. Investigations of the as-grown disks indicated that the central area (i. e. near the InGaAs/Si interface) had a low gallium composition compared to regions farther away from the center [68]. This again lead to investigations which showed that removing TMGa from the initial growth improved nucleation. It was also shown that despite InAs having larger lattice mismatch with Si than InGaAs, the crystal quality was better with InAs nucleation as compared to InGaAs nucleation. In the InAs case, dislocation misfits were extinguished within a few monolayers of the growth interface. This misfit extinction was attributed to the weak binding energy of InAs [69].

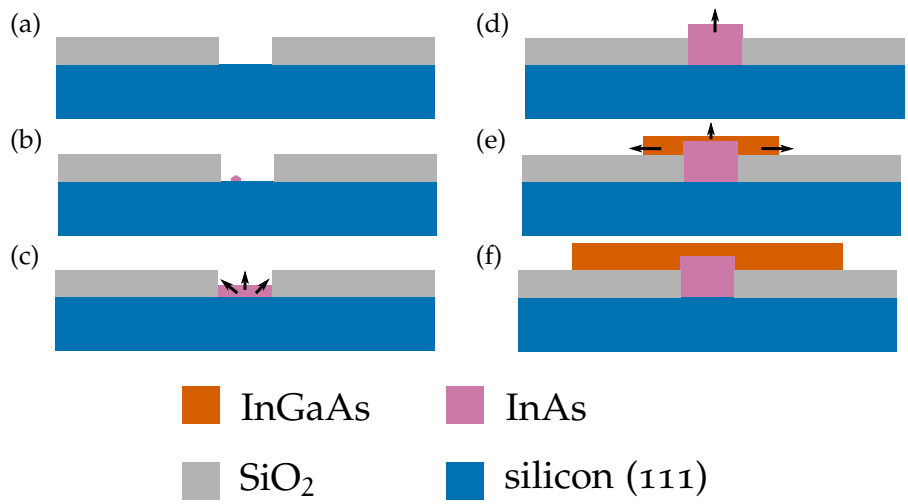

Figure 8: Progression of cross sections through the growth of InGaAs on (111) silicon. (a) the patterned substrate before growth and during thermal cleaning. (b) InAs nucleation. (c) InAs growth filling out the growth channel. (d) Vertical growth of InAs on $\bar{1}10$ facet.(e) Growth of InGaAs dominated by lateral overgrowth. (f) Completed InGaAs disk.

The adopted growth is illustrated in fig. 8 and consists of four main steps:

1. Thermal cleaning and tertiarybutyl phosphine (TBP) pre-flow (fig. 8a)
2. InAs nucleation (fig. 8b)
3. InAs pillar growth (figs. 8c and 8d)
4. InGaAs lateral overgrowth (figs. 8e and 8f)

2.4.1 *MOCVD system*

All growths were performed on a Aixtron AIX200/4 MOCVD system. This system has a horizontal, single-wafer reactor with the option of injecting various III/V precursors and dopants. The system has three main lines leading into the reactor, namely *run hydride*, *run Fe* and *run MO*. During operation, the flow rate for these lines are kept constant at 5500 sccm, 1500 sccm and 6000 sccm, respectively. The reactor pressure is also kept constant at 100 mbar by maintaining a constant controlling the exhaust flow with the indicated throttle valve. These values are system design values.

Precursors are injected into the growth chamber by bubbling hydrogen through a temperature controlled vessel containing the precursors in liquid form. The group-III precursors, TMIn and TMGa, and the *p*-type dopant precursor dimethylzinc (DMZn) are injected via the *run MO* line. The group-V precursors, TBAs and TBP, and *n*-type dopant hydrogen sulfide (H_2S) are injected via the *run hydride* line. The metalorganic precursors, TMIn, TMGa, DMZn, TBAs, TBP are injected by individually bubbling hydrogen through liquid form of these precursors. The key parameter for the precursors in the reactor is the partial pressure of each species. This is determined by controlling the source flow rate into the individual bubblers, dilution (i. e. adding pure hydrogen carrier gas to the flow), the injection flow rates and the bubbler pressure. Additionally, bubbler temperature is tightly controlled to manufacturer and supplier specifications.

Inside the reactor, the sample is kept on a susceptor which rotates to ensure uniform growth conditions across the sample area. The exact growth kinetics are beyond the scope of this dissertation, but generally the metalorganic precursors react with the surface with the group-III or group-V atoms forming bonds with on the surface lattice while the bonds to the organic components break off. These by-products are mostly swept away into the exhaust flow.

2.4.2 *Initial condition*

Prior to growth the samples are thoroughly cleaned to remove organic contaminants and the thin native oxide layer which forms inevitable when silicon is exposed to the oxygen of the atmosphere. To prevent re-oxidation of the surface, the samples are placed in an oxygen and H_2O free N_2 atmosphere immediately after cleaning. Growth is performed within 48 h of this. The cleaning procedure is detailed in appendix A.2.

To prevent contamination from previous growths in the same reactor, a bake-and-coat process with dummy samples is performed before any growths take place. In this process, the susceptor is heated to 650 °C while TMGa and TBAs is injected. The purpose of this is to coat the surface of the reactor vessel with a GaAs coating which acts as a barrier layer preventing contaminants (e. g. dopants used in preceding growths) from polluting the reactor atmosphere and being incorporated into the InAs/InGaAs lattices. The coating time is at least 15 min.

2.4.3 *Thermal cleaning*

The growth process is initiated by heating the susceptor to 850 °C. As the susceptor temperature passes 200 °C, the TBP run-line is opened, introducing TBP into the reactor. The temperature is kept at 850 °C for 5 min before it is cooled to a growth temperature of 610 °C. The TBP flow rate is given in table 2.

The purpose of this high-temperature step is to promote desorption of any H atoms terminating dangling Si bonds and any native oxide which may have formed on the silicon surface between cleaning and growth. However, this high temperature cleaning can also cause desorption of contaminants on the reactor walls and susceptor. These can then be absorbed on the silicon surface creating an undesirable surface structure. To prevent this absorption of contaminants, a group-V precursor is introduced to terminate the silicon surface and the best results in terms of nucleation uniformity have been demonstrated using TBP. This step has been amply illuminated by Kondo et al. [71] and Deura et al. [73]

2.4.4 *InAs nucleation*

After the susceptor has reached 610 °C the TBP run-line is closed while the TMIn and TBAs run-lines are opened. This causes InAs to nucleate on the silicon surface. After 20 s the TMIn run-line is closed terminating the nucleation. At no point during the following process is the TBAs run-line closed. This is done to prevent desorption of As from the already grown III/V material. The partial pressure ratios used for nucleation are listed in table 2.

On average the nucleation step will produce one nucleus per growth site. However, as this is a stochastic process there is a certain probability of two or more nuclei forming at each growth site. If this is to happen then the resulting InGaAs will most likely be polycrystalline and un-usable for further device processing.

2.4.5 *InAs pillar growth*

After nucleation, the TMIn and TBAs partial pressures are changed according to table 2 and the TMIn run-line re-opened. The change in partial pressure from the nucleation stage promotes lateral growth filling out the growth window as

Table 2: Common growth conditions for thermal cleaning, nucleation and InAs growth.

	Reactor pressure [Pa]	Temperature [°C]	Time	Partial pressure [Pa] Group III TMIn	Group III TMGa	Group V TBAs	Group V TBP	V/III-ratio
Thermal cleaning	10e3	RT→ 850	—	0	0	0	4.75	–
		850	5 min					
		850→ 610	—					
Nucleation	10×10^3	610	20 s	0.0681	0	2.76	0	41
InAs growth	10×10^3	610	thickness dependent	0.0443	0	5.40	0	122

illustrated in fig. 8c. [71] As the growth window is filled, a stable (111) top surface is created for further InAs growth. For the applied conditions it has been shown that growth on this surface is strongly preferential to growth on other facets. This leads to almost exclusively vertical growth of InAs as illustrated in fig. 8d. [74] The timing of the growth depends on the desired InAs pillar height. It has been shown that under the right InGaAs growth conditions, InAs pillar height above the SiO_2 surface determines the final InGaAs disk thickness. [74] The InAs growth is concluded by closing the TMIn run-line.

2.4.6 *InGaAs lateral overgrowth*

After changing the TMIn, TMGa and TBAs, the TMGa run-line is opened and the TMIn run-line is re-opened. The growth rate on the (111) and $\{\bar{1}10\}$ facets depend on the partial pressure ratios of the group III- and V-precursors.

2.4.7 *Cool down*

After growth, the IR-heaters are de-activated, cooling the susceptor and sample to room temperature. TBAs flow is maintained as long as the temperature is above 300 °C to prevent decomposition of the InGaAs disks due to dissociation of arsene.

2.4.8 *Doping*

It has been shown that the InAs grown by this recipe has an estimated background doping concentration of 2×10^{16} due to the incorporation of carbon [78]. The carbon stems from the organic by-products of the growth process.

In order to achieve *n*- and *p*- doping of InGaAs it is sufficient to introduce H_2S gas or DMZn precursors, respectively, into the reactor during InGaAs growth. A limited study on the effect of doping on disk morphology will be presented in section 3.1.

2.4.9 *Mask pattern*

The masks used for μSAG in this work have circular growth channels etched into SiO_2 in a hexagonal pattern. This geom-

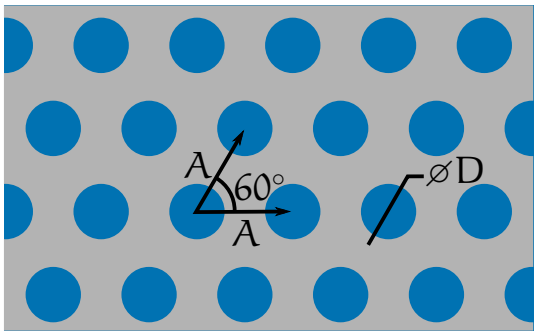

Figure 9: Growth mask layout. Circular growth channels arranged in a hexagonal latticed are etched into an SiO_2 layer, exposing the underlying (111) silicon surface.

Table 3: Mask layout parameters.

	Parameter	Value
Hole diameter	D	1 µm
Hole pitch	A	10 µm

etry is illustrated in fig. 9 with the parameters in table 3 being used for all growths treated in this dissertation. Compared to $D = 2\,\mu m$, a hole diameter of $D = 1\,\mu m$ has been shown to fill the growth surface faster (as illustrated in fig. 8c). [74] This is found to be preferential when using thin growth masks (~100 nm) and thin InGaAs disks are desired as a longer lateral filling time would also increases the vertical growth resulting in a higher minimum height of the InAs pillars. Although some growths in this dissertation utilizes thicker SiO_2, this nominal mask pattern has been adopted without further consideration.

The choice of hole-pitch $A = 10\,\mu m$ was based on qualitative evaluation of previous unpublished work. Although hole pitch does affect growth, this value has been found to support the growth of disks with adequate uniformity. Changing this parameter leads to changes in uniformity, thickness and diameter as it changes the growth kinetics due to changes in the local pressure and diffusion gradients both on the surface and the surrounding atmosphere.

2.5 DISK GEOMETRY

The InGaAs-on-silicon disks can be described by two parameters: corner-to-corner diameter $2A$ and thickness h as shown in fig. 10. Based on previous experience of InGaAs-on-silicon

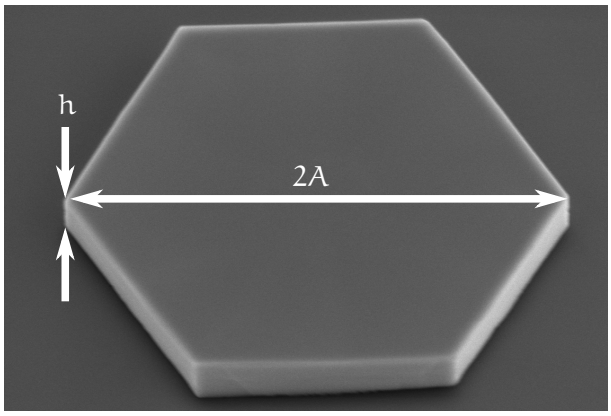

Figure 10: Geometrical parameters of InGaAs disks

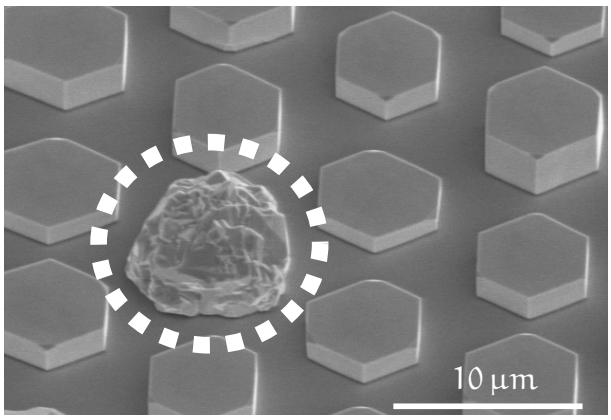

Figure 11: SEM image of polycrystalline growth (circled) surrounded by monocrystalline disks.

growth, disks with a diameter of more than 8 µm are achievable. Furthermore, highly uniform disks with high aspect ratios of $2A/h = 25$ have been demonstrated in a study by by Sugiyama et al. [74] which also suggest that there exists a strong correlation between final InGaAs thickness and the initial InAs height above the SiO_2 surface. This showed clearly that given the right conditions, InGaAs growth is almost exclusively lateral and that the island thickness is solely determined by InAs growth time. Thus it does not seem unreasonable to expect 8 µm disks with 200 nm to 300 nm thickness to be achievable, matching the device layer thicknesses commonly adopted for silicon photonics.

2.5.1 *Polycrystalline growths*

Figure 11 shows a SEM image of as-grown InGaAs-on-silicon disks. Most of the disks appear well formed, however the circled growth is obviously polycrystalline with a rough, multi-faceted surface. This image also illustrates how these growths are generally much taller than the desired, monocrystalline disks. The most likely sources for these growths is multiple nucleation within the growth window as was previously illustrated in fig. 5. Although high uniformity growths have been achieved [74], the issue has not been eliminated and must be taken into account when growing InGaAs-on-silicon for functional devices.

2.6 CMOS COMPATIBILITY

While silicon CMOS compatibility has not been strictly evaluated previously a brief mention of the main challenges is in place. Two main challenges are substrate orientation and process integration.

The former, substrate integration, is a challenge since (100) is by far the most common silicon substrate orientation in the CMOS industry. There are a couple of potential solutions to this. The first is to move CMOS processing to (111) substrates. This has been a topic of research and is technically possible [79, 80]. Another option is to target SOI platforms with a (111) oriented handle and (100) device layer. As 3D-integration (i. e. chip stacking) is being investigated for CMOS electronics [81], yet another option that presents itself is 3D-integration where InGaAs-on-silicon is part of a chip stack. [82] The choice of solution depends on application area and industrial/economic considerations which are beyond the scope of this dissertation.

When it comes to process integration, the main challenge is thermal limits. A common limit put on the process temperature for CMOS integration is 450 °C. [83, 84] The growth of InGaAs-on-Si utilizes a relatively low growth temperature of 610 °C, but benefits significantly from thermal cleaning at 850 °C. The 450 °C limit, however, is derived from degradation of interconnects [84]. Thus, it should be possible to achieve CMOS integration by modifying the CMOS process to allow for InGaAs before the deposition of metal vias and interconnects. Although more research and development is required, it is reasonable to assume that CMOS integration is within reach by implementing it

in the front end of line process where the thermal constraints are not as strict as for back end of line integration. [58, 83, 84]

Another thermal issue, is the limit on the acceptable temperature for InGaAs. High temperatures can lead to the decomposition of InGaAs due to dissociation of arsene. High temperatures can also lead to diffusion of zinc p-type dopants which degrades the doping profile. This means that any growth has to happen after any high temperature steps in the CMOS process. Thus InGaAs growth is believed to be possible, but should be performed after dopant activation and before metallization because of thermal considerations.

3 INGAAS-ON-SI NIR LED

The previous chapter covered the previous research on InGaAs on silicon growth. This research has mainly focused on growth mechanisms, uniformity and morphology, but no devices have yet been implemented. This chapter will present the growth and fabrication of proof-of-concept NIR LED based on InGaAs-on-Si disks.

3.1 DOPING AND MORPHOLOGY

In order to create a junction in the InGaAs island, it is necessary to introduce *n*- and *p*-type dopants to the growth. As mentioned in section 2.4.8 this is achieved by introducing H_2S or DMZn, respectively, during growth. It is not unreasonable to expect this to effect growth. In this section a brief investigation of the effect of doping on morphology is presented.

3.1.1 *Growth*

Six samples A–F were grown by µSAG MOCVD on Si (111) substrate with 80 nm thick SiO_2 growth masks with circular growth windows of 1 µm arranged in a hexagonal pattern of 10 µm pitch, prepared according to the procedure in appendix A.1 and cleaned according to appendix A.2. The growth was initiated by thermal cleaning, nucleation and 8 min 30 s growth of InAs using the standard conditions previously listed in table 2. For all samples, 100 min growth of InGaAs was performed with the conditions in table 4. For samples A–C, DMZn was injected at different D/V partial pressure ratios; for samples D–F, H_2S was injected at different D/III partial pressure ratios.

To analyse the samples, height maps such as the one in fig. 12 were captured using a *Lasertec H1200* confocal microscope with a nominal vertical resolution of < 0.1 µm. To analyse these images, a macro for the image processing suite *ImageJ* [85] was developed. Each growth is isolated based on image contrast and based on the circumference, area, diameter and surface roughness, the individual monocrystalline disks and their

Table 4: Growth condition for morphology investigation.

Sample		Reactor pressure [kPa]	Temperature [°C]	Time	Partial pressure [mPa] Group III TMIn	Group III TMGa	Group V TBAs	Dopants H_2S	Dopants DMZn	V/III-ratio	D/V-ratio	D/III-ratio
Thermal cleaning					See table 2							
InAs (A,B,C,D,E,F)		1×10^4	610	8 min 30 s	4.43×10^{-2}	0	5.40	0	122			
n-InGaAs	A	10	610	100 min	44.6	106	35.9	9.23	0	24	2.57×10^{-3}	0
	B							27.0	0		7.53×10^{-3}	0
	C							81.0	0		22.6×10^{-3}	0
p-InGaAs	D	10	610	100 min	4.46×10^{-2}	106	35.9	0	5.45	24	0	36.1×10^{-3}
	E							0	16.4		0	108×10^{-3}
	F							0	49.1		0	325×10^{-3}

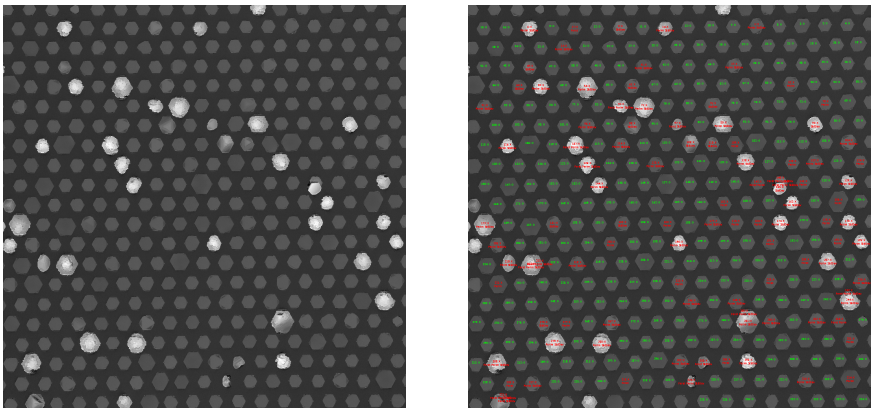

(a) (b)

Figure 12: Example of confocal image in (a) raw form and (b) processed form. The red text overlay signifies polycrystalline islands while the green text signifies mono-crystalline islands.

respective thicknesses is recorded. This enables rapid statistical analysis of a large number of disks using the rapid confocal microscopy technique. To illustrate the process, fig. 12 shows a confocal image from sample A with fig. 12b showing the identification of monocrystalline and polycrystalline growths as labeled with green and red text, respectively.

Scatter-plots and histograms of the disk thickness vs. diameter for the six growths A–F are shown in fig. 13. Table 5 lists the expectation values μ and standard deviations σ for the disk thickness and diameter. Another observation comes by defining the ratio of monocrystalline disks to total number of disks as monocrystalline yield

$$Y_{MC} \equiv \frac{\#\text{monocrystalline disks}}{\#\text{monocrystalline disks} + \#\text{polycrystalline disks}}. \quad (1)$$

Visually, this is equivalent to the ratio of red labels to total number of labels in fig. 12b.

For the n-doped samples A–C we observe that as the partial pressure ratio increases; there is a 20 % decrease in thickness when increasing the D/V partial pressure ratio from 0.26 % to 2.25 %. This indicates that either the growth on the $\{1\bar{1}0\}$ facets is enhanced or that growth on the (111) facet is suppresses. Looking at the statistics for the disk diameter we see no clear trend indicating that the $\{1\bar{1}0\}$ facet growth rate is unchanged. Thus we conclude that sulfur doping suppresses growth on the (111) top face.

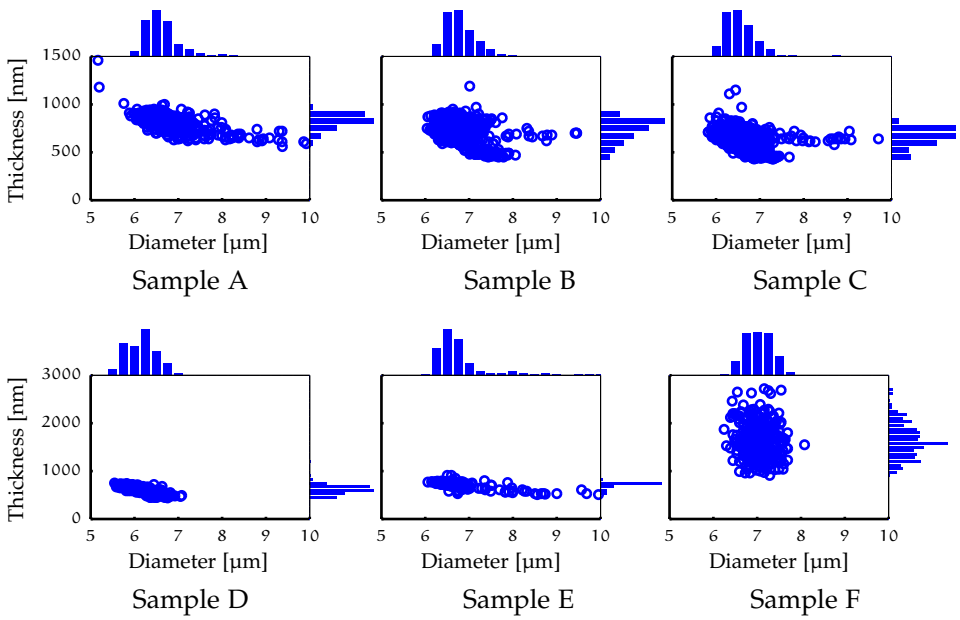

Figure 13: Scatter plots of disk diameter vs thickness for sulfur/*n*-doped samples A–C; and zinc/*p*-doped samples D–F. Histograms of the distribution are plotted on the horizontal and vertical axes.

Examination of the *p*-doped samples D–F shows that the thickness increases only slightly from 614 nm to 717 nm when increasing the D/III partial pressure ratio from 3.61 % to 10.8 %. However, when the D/III ratio it is further increased to 32.5 % there is a 130 % increase in the average thickness. At the same time, the standard deviation of the thickness σ_d also increases greatly from 74 nm to 360 nm. Not only is this a large increase in absolute value, but it also represents a increase in the thickness' coefficient of variation $c_{v,d} \equiv \sigma_d/\mu_d$ which increases from 10 % for sample E to 22 % for sample F. Interestingly, despite the increased non-uniformity in disk thickness, there is no decrease in monocrystalline yield. This arguably supports the idea that the polycrystalline growths are primarily caused during the initial nucleation and that these are not formed after stable growth facets have been established.

The investigation presented here is limited, but serves as a starting point. A more comprehensive review of the effect including the distribution of dopants is currently being undertaken by others. [7] Unpublished findings indicate that the dopants are not uniformly distributed within the disk which complicates establishing a relationship between partial pressure ratios and doping levels. Significant more research is re-

Table 5: Morphology statistics for *p*- and *n*-doped InGaAs disks on silicon. μ is the expectation value, σ the standard deviation and Y_{MC} is defined in eq. (1).

		Sulphur doped (*n*)			Zinc doped (*p*)		
		A	B	C	D	E	F
Partial pressure ratio		0.26 %	0.75 %	2.25 %	3.61 %	10.8 %	32.5 %
Thickness	μ_d [nm]	827	740	664	614	717	1640
	σ_d [nm]	78	135	123	93	74	360
Diameter	μ_d [µm]	6.7	6.8	6.6	6.1	6.8	7.0
	σ_d [µm]	0.6	0.4	0.5	0.4	0.8	0.3
Monocrystalline yield	Y_{MC}	70 %	71 %	65 %	76 %	82 %	88 %

quired to establish a useful model for dopant distribution and concentration.

3.2 DIODE GROWTH

Thick oxide layers with growth masks were prepared using wet oxidation, dry and wet etching according to the recipe in appendix A.1. The µSAG pattern consisted of 1 µm holes arranged in a hexagonal lattice with 10 µm pitch. The day before growth, the samples were cleaned using organic solvents, piranha etch and diluted buffered hydrofluoric acid (BHF) according to the recipe in appendix A.2; to prevent over-night oxidation the samples were kept in nitrogen atmosphere in the MOCVD system's glove box.

Growth was initiated with 850 °C thermal cleaning and surface passivisation with TBP as described in section 2.4.3. This was followed by InAs nucleation and fill-out of the growth channel by injecting TMIn and TBAs into the reactor with the susceptor at 610 °C as described in section 2.4.4. The detailed conditions for these steps were as previously listed in table 2.

Following nucleation, TMIn and TBAs partial pressures were adjusted to allow vertical growth of InAs for a growth time of 8 min 30 s as shown in table 6. This growth time was chosen as a shorter, 5 min growth time was found to produce lower yields of hexagonal, monocrystalline disks. Immediately after InAs growth, the partial pressure ratios are adjusted and TMGa and H_2S are added to the injection mix to form *n*-type InGaAs. For the *pin*-structure, the H_2S injection was terminated after 50 min and followed by 10 min of un-doped growth. In the

Table 6: Growth condition for *pn* and *pin* diodes.

	Step	Temperature	Time	Partial pressure [mPa] Group III TMIn	Group III TMGa	Group V TBAs	Dopants H_2S	Dopants DMZn	V/III-ratio	D/V-ratio	D/III-ratio
Common	Thermal cleaning and nucleation	Standard conditions cf. table 2									
	InAs	610 °C	8 min 30 s	44.3	0	5400	0	0	122	0	0
	n-InGaAs	610 °C	50 min	34.9	100	9480	71.1	0	70	0.75 %	0
pn	*p*-InGaAs	610 °C	110 min	34.9	100	9480	0	13.6	70	10 %	0
pin	*i*-InGaAs	610 °C	10 min	34.9	100	9480	0	0	70	0	0
	p-InGaAs	610 °C	100 min	34.9	100	9480	0	13.6	70	10 %	0

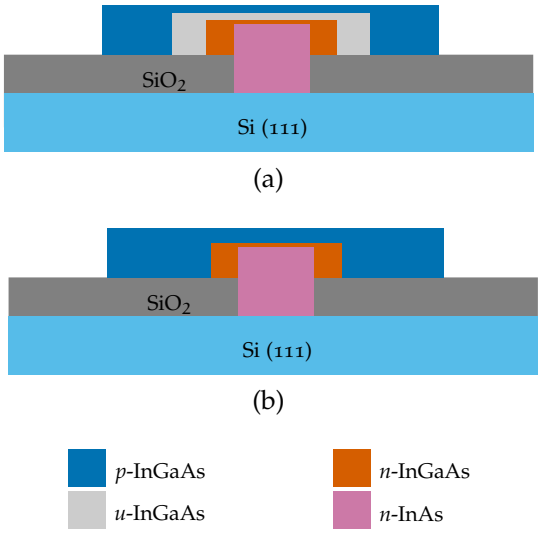

Figure 14: Cross section of (a) *pin* structure and (b) *pn* structure.

case of the *pn*-structure, the H_2S injection was terminated after 60 min. The process is then immediately followed by growth with DMZn added to the injection mix to form *p*-type InGaAs. The growth is terminated after an additional 100 min for a total InGaAs growth time of 160 min in both cases. The details of the condition is listed in table 6. The final structure should have a cross section as illustrated in fig. 14a and fig. 14b for the *pin* and *pn* cases respectively.

3.3 MORPHOLOGY

Due to a significant inhomogeneity in the mask thickness and properties there was a rather large intra-sample non-uniformity in growth morphology. This was measured for both *pn* and *pin* growths which showed similar results. Figure 15 shows the morphology of ten arbitrarily selected areas on a *pin* sample chip; each color represents disks from a distinct area. The areas are captured at the maximum magnification of 100× and each confocal microscope image covers a square area 177.4 µm × 177.4 µm. The statistics of these areas are summarized in table 7 with the last column showing the statistics for all monocrystalline disks within the area. The data shows that the uniformity within each area is comparable to the growths in section 3.1. However, the non-uniformity in morphology across the sample is significant. For instance (cf. table 7), area F has an average thickness of 900 nm and average diameter of 8.3 µm while area C has an average thickness of 2870 nm and an aver-

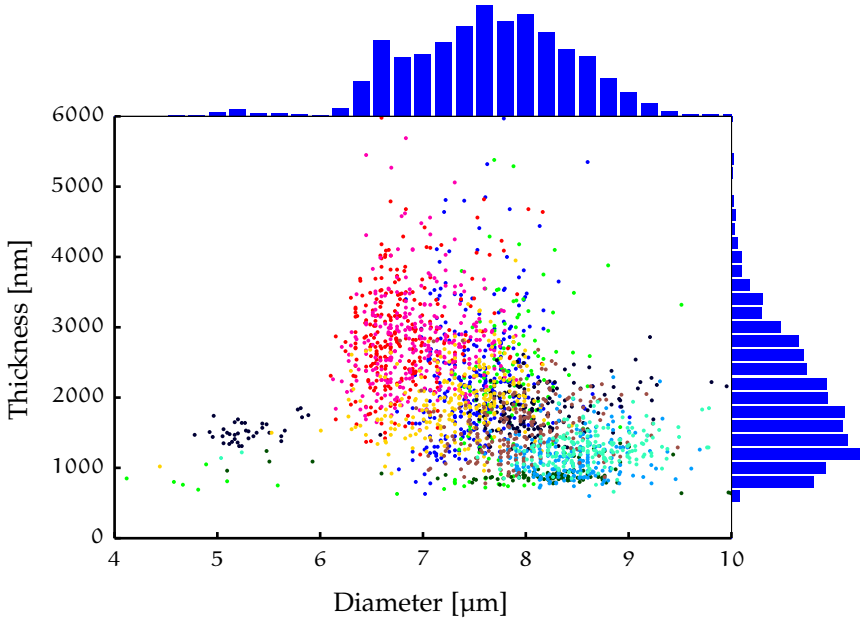

Figure 15: Distribution of disk geometry for *pin* disks. The colors represents different, arbitrarily chosen regions on the sample.

Table 7: Summary of statistics for ten arbitrarily selected areas on as-grown *pin* samples.

Region	Thickness		Diameter		Monocrystalline yield
	μ_t [nm]	σ_t [nm]	μ_d [µm]	σ_d [µm]	Y_{MC}
A	2280	847	7.5	0.37	86%
B	2130	943	7.7	0.74	42%
C	2870	724	6.8	0.38	78%
D	1790	316	7.6	1.18	57%
E	2810	651	7.0	0.39	87%
F	900	159	8.3	0.83	37%
G	1990	470	7.3	0.50	76%
H	1170	286	8.5	0.44	69%
I	1560	403	8.0	0.47	66%
J	1270	234	8.6	0.54	59%
Overall	1980	856	7.6	0.83	66%

age diameter of 7.6 µm. For all regions combined, the average disk thickness is 1980 nm with a comparably large standard deviation of 856 nm; the diameter has an average value of 7.6 µm with a standard deviation of 0.83 µm.

Qualitatively, inspection of fig. 15 does not reveal any strong correlation between diameter and thickness. This indicates that the lateral growth of has saturated. This is further supported by the relatively moderate standard deviation in diameter σ_d when all areas are considered. Thus for future experiments, reduction of the growth time is possible to reduce the disk thickness without compromising the diameter.

3.4 DEVICE PROCESSING

Ensembles of InGaAs disks were processed into diodes with topside gold electrodes. These electrodes has a honeycomb pattern with 5 µm openings for light extraction and collection. By isolating ensembles of diodes, the sample non-uniformity is eliminated. Here, the processing is briefly explained while a complete, illustrated explanation is contained in appendix A.3.

After growth, 3 µm AZ5214E photoresist was applied, exposed and developed to cover ensembles of 480 islands each. Since the polycrystalline disks are generally taller than the monocrystalline disks, they can be selectively exposed by ashing back the resist using O_2 plasma inductively coupled plasma reactive-ion etch (ICP-RIE). Wet etching for two minutes in a 1:15:30 mixture of (96 %)H_2SO_4:(30 %)H_2O_2:H_2O at room temperature removes the islands surrounding the covered ensembles as well as the exposed polycrystalline islands.

The resist is then stripped away and three layers of OCD T-12 spin-on-glass (SOG) is applied. Each layer is baked on hotplates in a two step process with 2 min at 80 °C followed by 2 min at 200 °C. The three layers are then cured at 300 °C for 30 min. This SOG layer is then etched back using a CHF_3/Ar ICP-RIE process, exposing the top of the islands. On top of the planarized structure, electrodes are formed in a honeycomb pattern with 5 µm hexagonal holes contacting the rim of the disks. For ohmic contacts, 10/30/80/300 nm Pt/Ti/Pt/Au electrodes without annealing are chosen [86]. The patterned were fabricated using photolithography and lift-off of electron beam (EB) evaporated metal. Finally an *n*-side electrode is formed on the un-polished Si backside by 300 nm thermally evaporated aluminum. The completed structure is illustrated in fig. 16. To facil-

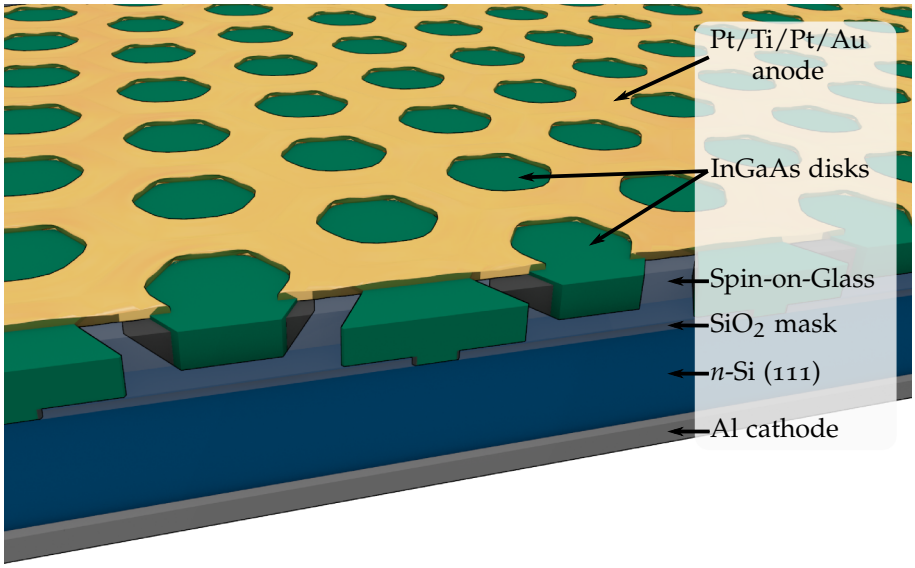

Figure 16: Cut-through model of fabricated structure (not to scale.)

itate measurement, the samples were mounted on copper using conductive silver paste.

3.5 IV CHARACTERISTICS

To verify that a functioning *pn* and *pin*-junctions have been formed, the current-voltage (IV) characteristics were measured under dark conditions. Results for *pn* and *pin* ensembles are shown in figs. 17a and 17b, respectively. Each plot shows three distinct ensembles on the same chip. We observe that there is significant intra-device variation in the characteristics. Some devices appear to have significant shunt resistance, which is attributed to two fabrication defects. One is shorts between the electrode pad and the silicon substrate. Such shorts can for instance occur if the SOG has peeled away in an area, revealing the un-occupied growth windows as illustrated in fig. 18.

However, we observe that several devices show good diode characteristics both for the *pn* and *pin* case. The threshold voltage is estimated to be approximately 0.5 V for *pin* ensembles and 0.4 V for *pn* ensembles. Due to the ensemble nature the devices must be considered as hundreds of diodes in parallel with non-uniform distribution of parameters such as series resistance, shunt resistance, idealty factor and threshold voltage. This is due to non-negligible non-uniformity between the disks in terms of composition as inferred from section 3.3 and fig. 15, doping distribution, disk geometry and contact align-

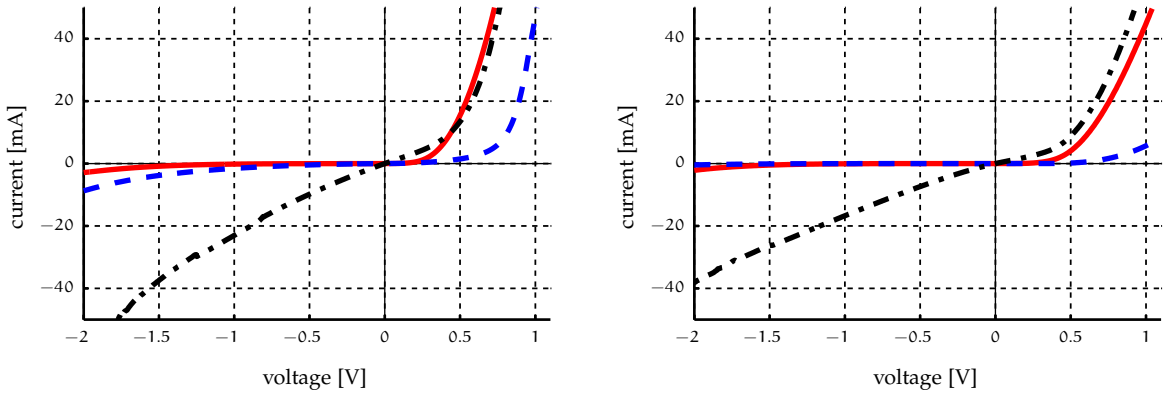

(a) (b)

Figure 17: IV characteristics for (a) *pn* disk ensembles and (b) *pin* disk ensembles.

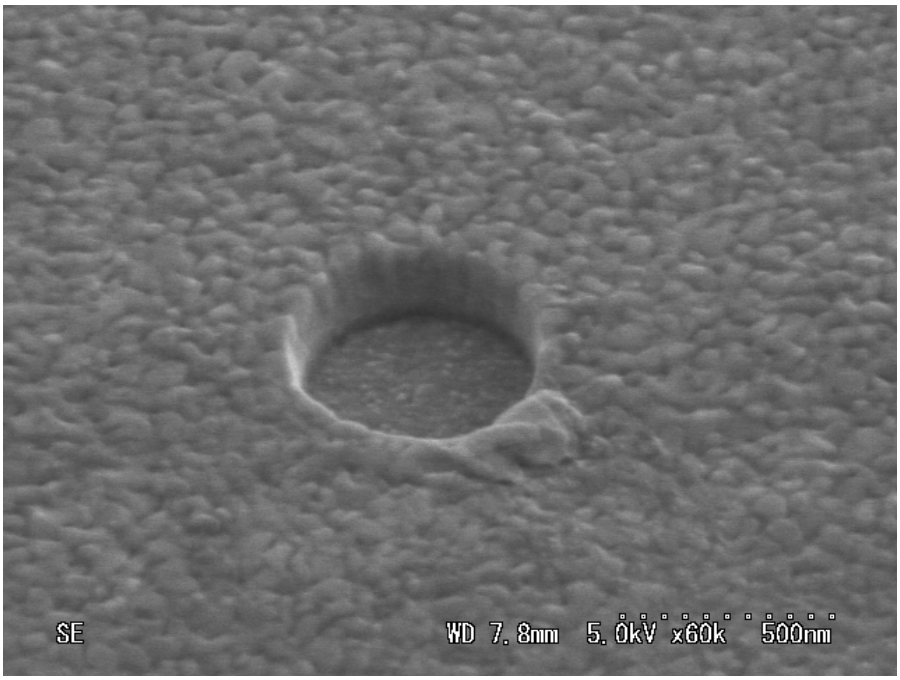

Figure 18: SEM image of short between gold electrode and the silicon substrate through an uncovered growth window.

ment/overlap. Thus quantifiable properties of the single junction are muddled and can not be extracted.

3.6 ELECTROLUMINESCENCE

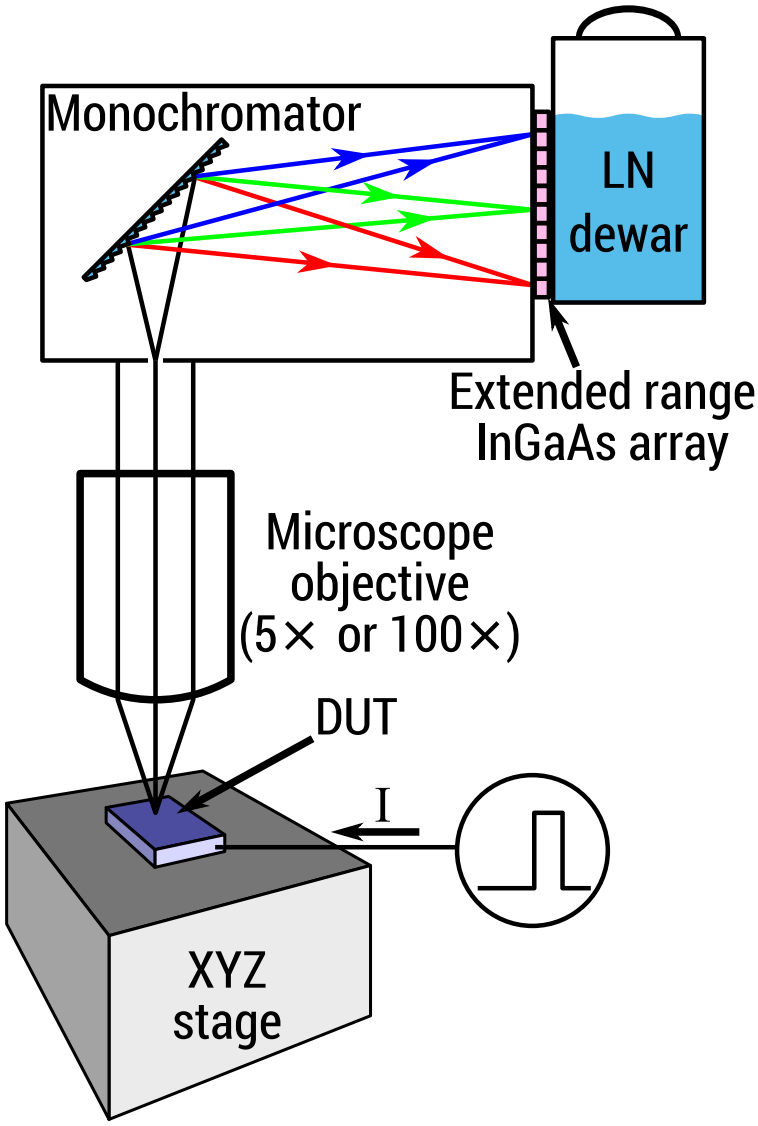

Figure 19: Schematic of setup for measurement of InGaAs electroluminescence.

Measurement of the electroluminescence (EL) for single ensembles of InGaAs disk were performed using a setup as illustrated in fig. 19. In the initial measurements, light was collected by a microscope objective and analyzed by a Princeton Instruments Acton SP2500 monochromator and detected by a Prince-

ton Instruments PyLoN-IR 1024-1.7 InGaAs linear sensor array cooled to −100 °C which has a cut-off at 1.6 µm.

With this setup no luminescence could be detected from any forward biased *pn* ensemble at room temperature. However, for the case of *pin* InGaAs ensembles, a good signal was detected. However, the spectrum extended beyond the sensor cut-off.

Consequently, measurements of the EL for a single ensemble of *pin* InGaAs disks was performed using a comparable setup for micro-EL, but with an extended range InGaAs array . Optical microscopy reveals that the ensemble under test has 307 disks which appear to be in contact with the top electrode remaining after removal of polycrystalline growths. The emitted light from these 307 disks is collected by a 5× microscope objective, analyzed by a monochromator and the spectrum measured with an Horiba Jobin Yvon 3LD-512x1-50-2200 extended range InGaAs sensor array. The sample was kept at room temperature with the sensor cooled to −120 °C and under pulsed current injection (10 % duty cycle, 10 kHz) the EL spectra in fig. 20 were obtained. These show a broad spectrum with a full-width at half-maximum (FWHM) in excess of 290 nm at 50 mA. We attribute the broadness of the spectrum to a non-uniform InGaAs composition throughout the disk. Peak luminescence is found at 1.78 µm which corresponds to a significantly larger energy than the band-gap of InAs and indicates that recombination occurs in the InGaAs regions.

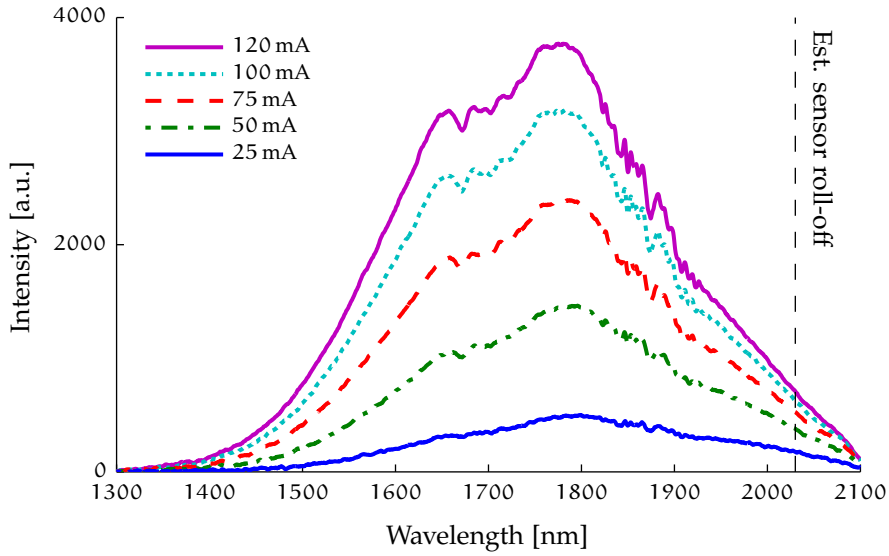

Figure 20: Electroluminescence spectrum for various injection currents with *pin* sample at room temperature.

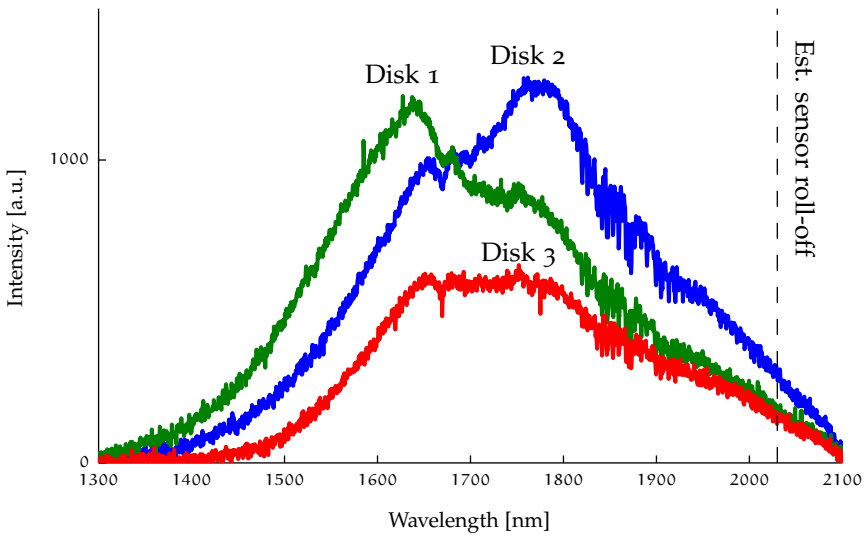

Figure 21: Room temperature electroluminescence from three distinct *pin* disks within the same ensemble forward biased at 50 mA.

The spectra also show a local maxima at 1.65 µm. To further clarify the origin of this, a 100× microscope objective is used to collect light from individual disks. Figure 21 shows the spectrum from three distinct disks when the entire ensemble is forward biased at 50 mA. The main conclusion from fig. 21 is that both maxima are present in each of the disks. This shows that the two maxima stem from radiative recombination in two distinct processes in each disk and not from variations between individual disks. The large difference in the spectrum shapes can be explained either by variations in the collection spot position; non-uniformity between the disks; or variations in current densities.

Since InAs has a narrow bandgap of 354 meV corresponding to a wavelength of 3.5 µm, the observed electroluminescence must be from the InGaAs regions. To explain the presence of two peaks we first discount differences in composition as unreasonable. While the InGaAs composition is expected to be non-uniform through the disk, no discontinuities are expected. A more reasonable explanation is to consider the different peaks to stem from regions of differing doping levels. This is reasonable because InGaAs has a strong doping dependent bandgap narrowing effect on the order of 10^1 meV to 10^2 meV [87]. Thus, we assume that the short wavelength peak stems from the intrinsic region and that longer wavelength peaks stems from doped regions. A peak wavelength

of 1.65 µm corresponds to a bandgap of 0.75 eV. According to Goetz et al. [88], the relationship between bandgap energy E_g and gallium content x can be expressed as

$$E_g = E_g^{InAs} + (E_g^{GaAs} - E_g^{InAs})x - Cx(1-x), \tag{2}$$

where $E_g^{InAs} = 0.354\,eV$ and $E_g^{GaAs} = 1.424\,eV$ are the binary bandgap energies and $C = 0.475$ is the bowing parameter. At 300 K the short wavelength peak at $E = 0.75\,eV$ indicates a gallium content of 48 % in the intrinsic region under the assumption that there is negligible incorporation of background dopants.

To compare with other methods of determining gallium content we consider the investigation of Deura et al. [70]. In a study by Deura et al. [70], InGaAs that study, disks were grown without the use of InAs nucleation and pillar growth (i. e. with InGaAs nucleation) and with partial pressures of $P_{TMGa} = 16\,mPa$, $P_{TMIn} = 13\,mPa$ giving $P_{TMGa}/P_{TMIn} = 1.2$, and $P_{TMAs} = 5.4 \times 10^3\,mPa$ giving a V/III-ratio of 186. For the *pin* diodes grown here the corresponding values are 2.9 and 70, respectively (cf. table 6.) Furthermore the masks were 100 nm thick with 2 µ growth windows and a pitch of 7 µ. These growths yielded disks of approximately 1 µm thickness and 5 µm diameter which is comparable to the aspect ratios of the *pin* disks reported here.

Using transmission electron diffraction (TED) to the perform localized measurements of the lattice constant the study inferred a gallium composition of 47 % to 67 % in areas away from the growth interface. This is a rather large compositional range and although the growth conditions are different it does indicate that the derived gallium composition of 48 % is reasonable.

The peak at 1.78 µm corresponds to approximately 50 meV bandgap narrowing. This is a reasonable value for weak *n*-type doping and strong *p*-type doping [87].

3.6.1 *Efficiency*

By integrating the measured intensity, the relationship between the injection current I and output integrated intensity L is established. For the device under test, this I-L relationship is shown in Figure 22. Assuming the measurement sensor's quantum efficiency is approximately wavelength independent and the system has approximately wavelength independent transmission coefficients then the intensity as measured by the sensor and

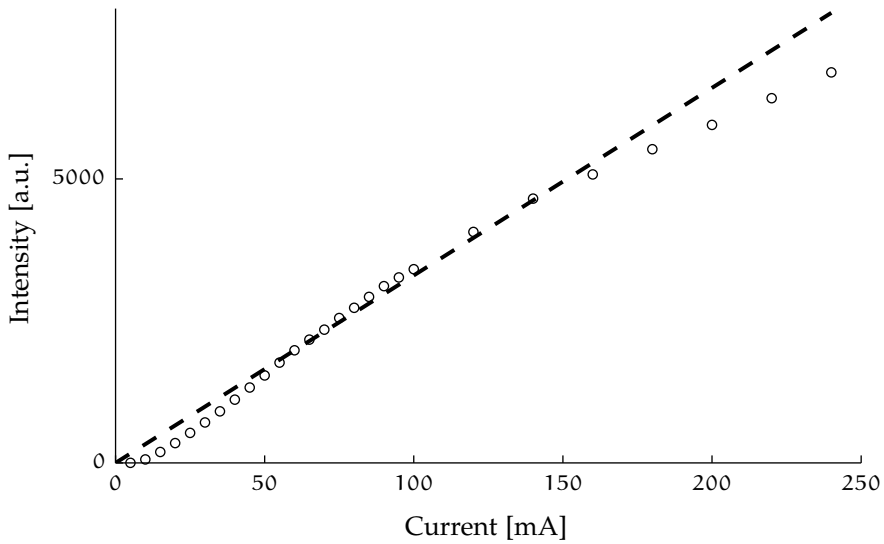

Figure 22: Integrated intensity (circles) as a function of current for sample at room temperature and sensor. The dashed line indicates a linear fit for current $< 100\,\mathrm{mA}$.

plotted in figs. 20 and 22 is proportional to the number of emitted photons. Furthermore, for an ideal device, every injected electron/hole-pair would recombine in the active region and generate one photon. Thus an ideal device with 100 % internal quantum efficiency (IQE) and intensity independent extraction coefficient would have a linear I-L relationship. I. e.

$$I \propto L. \tag{3}$$

However, for the device under test, the I-L relationship in fig. 22 shows that a linear fit cannot be obtained. The dashed line of the figure indicates a linear fit for $I < 100\,\mathrm{mA}$ which the intensity clearly deviates from at higher currents. This drop is due to a drop in external quantum efficiency which is defined as

$$\mathrm{EQE} = \eta_e \equiv \frac{\#\text{emitted photons}}{I/q}, \tag{4}$$

where I is the injection current and q the elementary charge (i. e. $I/q = \#\text{injected carriers}$.) This is related to the internal quantum efficiency which is defined as

$$\mathrm{IQE} = \eta_i \equiv \frac{\#\text{generated photons}}{I/q} = \eta_{\mathrm{ex.}}\,\mathrm{EQE}, \tag{5}$$

where $\eta_{\mathrm{ex}} \leqslant 1$ is the extraction coefficient which is usually significantly less than unity due to total internal reflection trapping photons which are then re-absorbed by the device. Thus

fundamentally the deviation from an ideal linear I-L relationship is due to a drop in IQE.

There are several possible explanations for this drop in IQE. The first to be considered is the possibility of non-radiative recombination. Ideally, recombination in an LED can be modelled by classical rate equations. If we ignore for a moment the geometry of this device and simply consider a double heterostructure LED where carriers are trapped by the active region, then the ideal, steady-state rate equations can be expressed as

$$\frac{\eta_j J}{qd} = AN + BN^2 + CN^3, \tag{6}$$

where J is the injection current density, η_j is the current injection efficiency, q is the elementary charge, d is the junction width, N is the active region carrier concentration and A, B, C are the recombination coefficients representing Schockley-Read-Hall recombination, radiative recombination and Auger recombination, respectively.

Under this model, it can be shown [89] that the relationship between the internal quantum efficiency $\eta_i = \text{IQE}$ and injection current density J can be written as

$$\eta_i = 1 - \frac{1-\eta_{max}}{2}\left(1 + \frac{\eta_i}{\eta_{max}}\frac{J}{J_{max}}\right)\sqrt{\frac{\eta_i}{\eta_{max}}\frac{J_{max}}{J}}, \tag{7}$$

where J_{max} is the injection current density at which peak IQE η_{max} is achieved. Here, trivially, the current density ratio J/J_{max} can be substituted by the absolute ratio I/I_{max} yielding

$$\eta_i = 1 - \frac{1-\eta_{max}}{2}\left(1 + \frac{\eta_i}{\eta_{max}}\frac{I}{I_{max}}\right)\sqrt{\frac{\eta_i}{\eta_{max}}\frac{I_{max}}{I}}. \tag{8}$$

Although η_i cannot be measured directly, it can be eliminated in eq. (8) by substitution with a relative quantum efficiency.

$$\eta_r \equiv \frac{\eta_i}{\eta_{max}} \tag{9}$$

yielding from eq. (8)

$$\eta_r = \eta_{max}^{-1} - \frac{1-\eta_{max}}{2\eta_{max}}\left(1 + \eta_r\frac{I}{I_{max}}\right)\sqrt{\eta_r\frac{I_{max}}{I}} \tag{10}$$

Here, the relative quantum efficiency can be quantified from measurements by assuming that

$$\eta_r = \frac{L/I}{\max(L/I)}, \tag{11}$$

where L is the integrated collected photon count. The justification for this is that since L is proportional to the photon count and I is proportional to the injected carrier count then

$$L/I \propto EQE \propto IQE \tag{12}$$

under the assumption that injection efficiency and extraction efficiency are independent of injection current. These are fair assumptions as long as the device's junction temperature is stable and effects such as free-carrier absorption is negligible.

Equation (10) then only has one unknown η_{max} for a set of measured $\eta_r(I)$. Under the assumption in eq. (12), I_{max} is given where $\eta_r = 1$.

However, applying this model to the I-L curve in fig. 22 does not yield good fits as can be seen in fig. 23. This figure shows the measured η_r based on fig. 22 together with plots of $\eta_r(I)$ for $I_{max} =$ at various values of the fitting parameter η_{max}. This implies that the reduced efficiency is due to other factors than Schockley-Read-Hall (SRH) and Auger recombination. The most likely explanation then is that at high currents the device temperature increases due to Joule heating. A reduced duty cycle for the driving current was applied to overcome this problem, but due to low light emission intensities it was not possible to record good spectrums.

A final note on the external quantum efficiency is to note that for a material with a refractive index of $n = 3.5$, the confinement due to total internal reflection limits the external quantum efficiency to 2 %. This number will be further reduced due to re-absorption in the disks, the limited area of the electrode windows as well as absorption in the metal contacts. The re-absorption problem is particularly important due to increased re-absorption due to band-gap narrowing.

3.7 PHOTO DETECTION

Next, photo detection is demonstrated by measuring the device I-V characteristics under three different conditions:

1. no-illumination

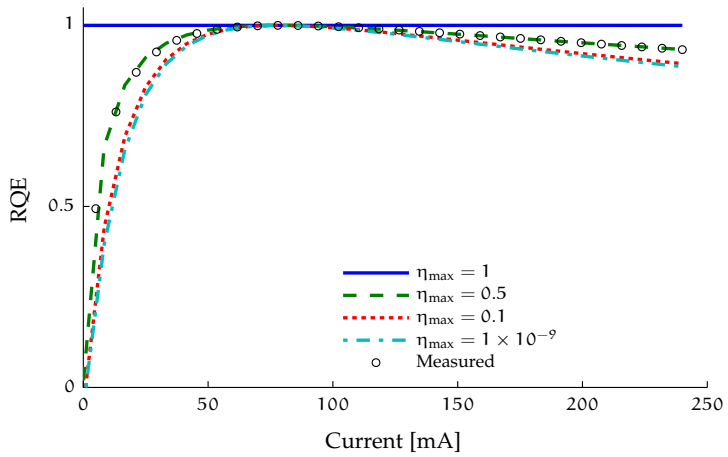

(a)

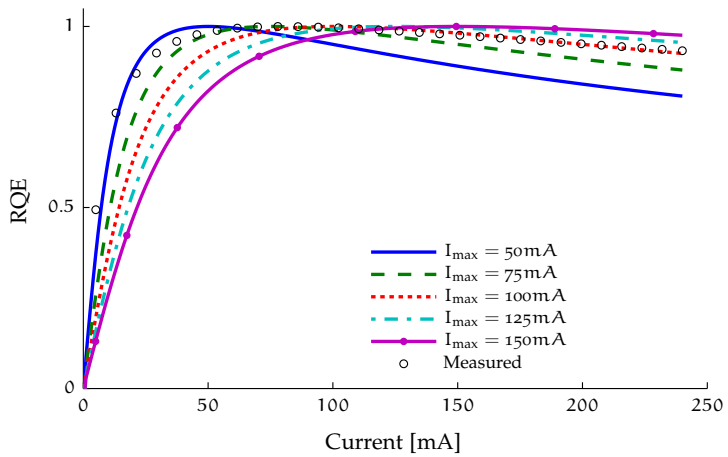

(b)

Figure 23: Fit of relative quantum efficiency as a function of current for various choices of (a) η_{max} with $I_{max} = 90$ given by the measured data and (b) I_{max} with $\eta_{max} = 0.001$. This illustrates how the rate-equation model in eq. (8) cannot explain the decreasing LED efficiency.

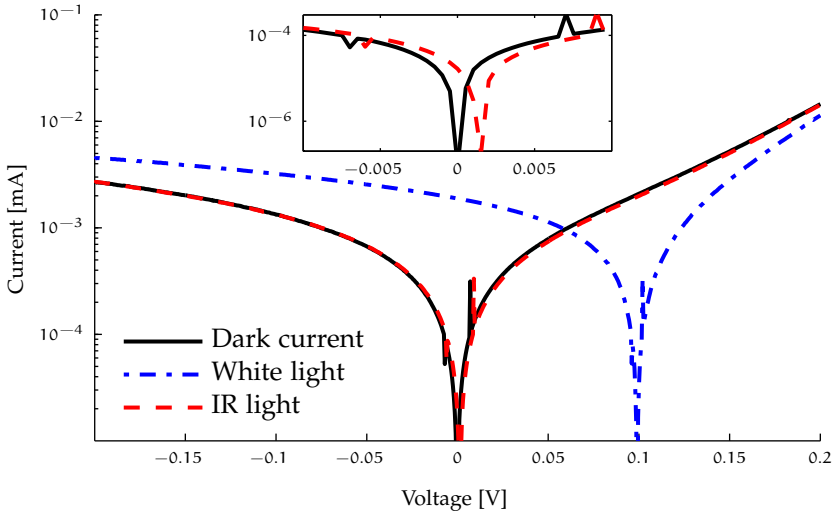

Figure 24: I-V characteristics under white light (0.5 µm to 1.7 µm) and IR (1.1 µm to 1.7 µm) illumination compared to dark I-V. The inset shows a magnified view around 0 V.

2. white light illumination
3. IR illumination

The white light illumination (2) has an intensity of 200 $\mu W\,cm^{-2}$ and a broadband spectrum from 0.5 µm to 1.7 µm. The IR illumination (3) is generated by the same source, but filtered by a Si-filter giving a spectrum from 1.1 µm to 1.7 µm. The results in fig. 24 show that a significant photo response is generated under white light conditions. This is attributed primarily to carrier generation in the InGaAs and not in the Si. First of all, there is no *pn*-junction in the Si region to support efficient carrier extraction. This is further supported by the fact that a photo current can be observed under Si-filtered IR illumination as is clearly demonstrated in the inset of Fig. 24. Even though this response is weak, it is reproducible and non-negligible with short-circuit current $I_{SC,IR} = 17\,nA$ and open-circuit voltage $V_{OC,IR} = 1.5\,mV$. The large reduction in signal strength is attributed to the power in the IR-region of the source's spectrum being significantly weaker than the power for wavelengths shorter than 1.1 µm. The overall weakness of the signal is attribute to a combination of small device area, narrow *i*-region, low optical intensity in the IR band and poor collection efficiency due to the high index contrast and gold electrodes.

An upper bound can be put on the collection efficiency by considering the collection area and the Fresnel reflection coefficient of the material. For 5 µm diameter electrode windows

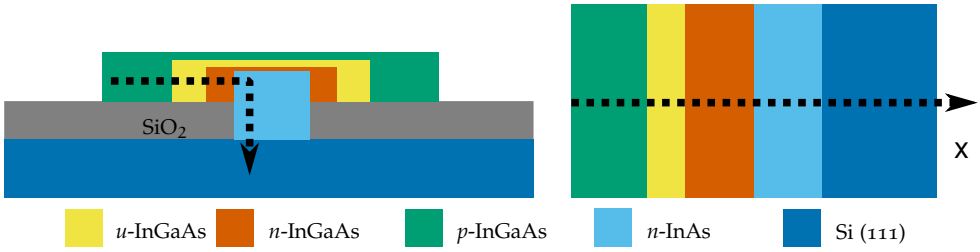

Figure 25: Following the dashed path the disk cross section is simplified into a one-dimensional structure.

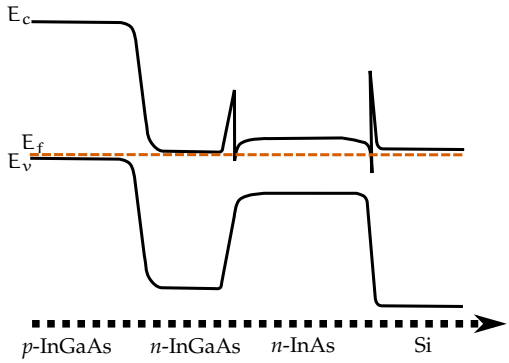

Figure 26: Sketch of band structure of ideal InGaAs *pn*-junction.

the window area is only 6.25 % of the total area. Furthermore, for a perpendicular, collimated incident light from air onto a surface with index of refraction $n = 3.5$, only 30.8 % is transmitted. Thus the overall collection efficiency cannot be larger than $6.25\,\% \times 30.8\,\% \approx 2\,\%$.

3.8 BAND STRUCTURE

Simplifying the cross section of the disks to a one-dimensional problem (ignoring contacts) as illustrated in fig. 25 some considerations of the band structure can be made. Figure 26 shows a sketch of the band structure for a *pn* junction [90]. The most important observation is that the *n*-InAs region would act as a strong trap for holes while the electrons have a barrier between the *n*-InGaAs and the *n*-InAs region. Although the *n*-InAs region also acts as an electron trap, this barrier will effectively increase the electron accumulation in the *n*-InGaAs region.

When biasing the junction, there is one important effect which must be considered and that is the geometry of the disk and the contacts. With annular or hexagonal contacts as applied here, the field can-not be uniform across the junction. For a uniform semiconductor disk with this geometry, the applied static

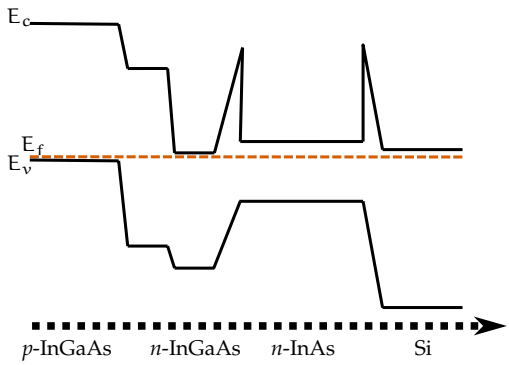

Figure 27: Sketch of band structure of ideal InGaAs *pin*-junction.

electric field must increase linearly from the *p*-contact on the edge towards the inner *n*-InAs core. Thus, the active region should—in the case of a lateral junction—be placed as close as possible to the core. As we will see in chapter 5 this matches nicely with the mode of a photonic crystal laser and is beneficial.

If the band diagram is simplified by ignoring the interface conditions a *pin* structure could have the band structure in fig. 27. The exact location of the un-doped InGaAs regions valence and conduction band depends on any background doping.

Considering the ideal structure depends on the application. A straight LED would be best with a vertical junction where the top *p*-layer is as thin as possible to suppress re-absorption of photons. In the case of a photonic crystal laser however, the ideal structure ensures maximum overlap with the laser mode. In any case the insertion of barrier material around the active region would be desired to improve confinement.

4 PHOTONIC CRYSTALS

Figure 28: Opal gemstones owe their brilliant colors to natural photonic crystal structures. (Photo by J.J. Harrison [9].)

photonic crystals (PhCs) are periodic structures in a material that affect the propagation and generation of light. In nature, they give rise to brilliant colors and can be found in birds feathers, butterfly wings and—as illustrated in fig. 28—minerals such as opals. These colors stem from the reflection of frequencies which lie within the so-called photonic bandgap. The photonic bandgap (PBG) is a band, or range, of frequencies for which the PhC is perfectly reflecting for all incident directions (i. e. it has a unity reflection coefficient.) It stems from the periodic nature of the material which causes multiple reflections of light to interfere constructively with each other outside the material while inside the material reflections interfere destructively. When this is true for all directions in a band of frequencies, this band is a PBG. For frequencies within the PBG all light is reflected perfectly and thus cannot exist within the crystal.

In one dimension, the PBG effect has been known at least since the 1880s when Lord Rayleigh derived the existence of a

frequency band gap in periodic structures and used this to explain *brilliant* reflection from periodic stacks of potassium chlorate crystals [91–93].

In contemporary usage, however, the term photonic crystal is usually limited to structures periodic in two and three dimensions, excluding one-dimensional structures such as Bragg gratings. In this respect, PhC research got its start in 1987 with two seminal papers. Eli Yablonovitch [94] showed that spontaneous emission of photons of certain energies is inhibited in a three-dimensional periodic structure (i. e. a 3D-PhC). Shortly after, Sajeev John [95] showed how photons can be confined by a defect in such a 3D-PhC. Both of these lay the foundation for the creation of photonic crystal cavity (PhCC).

A complete treatment of PhCs is beyond the scope of this dissertation, but a few key concepts will be presented here in order to enable better understanding of the following chapter.

4.1 DEFINITION

Fundamentally, a PhC is a periodic structure in one, two or three dimensions with wavelength-scale periodicity. The different dimensionalities (1D, 2D and 3D) are illustrated in figs. 29a to 29b with fig. 29d representing the special case of PhC slabs. PhC slabs are easily fabricated in for example SOI substrates where they can be formed by etching holes or pillars in the high-refractive-index device layer. Between 3D PhCs, 2D PhCs and PhC slabs, the latter is arguably the most practical for PhC devices in the optical regime.

PhCs structures can be expressed formally as

$$\overline{\overline{\epsilon}}(\mathbf{r}) = \overline{\overline{\epsilon}}(\mathbf{r} + \mathbf{R}) \tag{13}$$

$$\overline{\overline{\mu}}(\mathbf{r}) = \overline{\overline{\mu}}(\mathbf{r} + \mathbf{R}) \tag{14}$$

where $\mathbf{r}$ is a position vector; $\mathbf{R}$ is a translation vector which for an N-dimensional PhC is given by

$$\mathbf{R} \equiv \sum_{i=1}^{N} m_i \mathbf{a}_i \quad \text{for} \quad m_i \in \mathbb{Z}, \tag{15}$$

where $\mathbf{a}_i$ are the lattice vectors; $\overline{\overline{\epsilon}}$ is the complex dielectric permittivity tensor; and $\overline{\overline{\mu}}$ the complex magnetic permeability tensor. Unless otherwise stated, this dissertation assumes that all

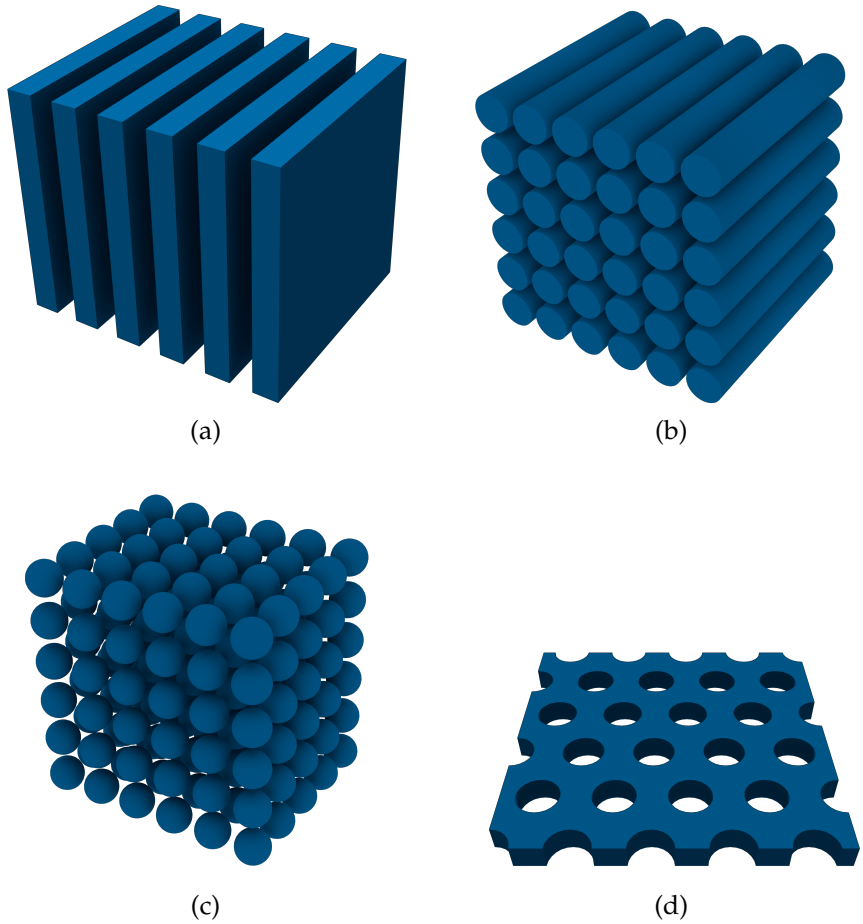

Figure 29: Different dimensionality for PhC structures: (a) 1D, (b) 2D, (c) 3D, and (d) slab PhC where confinement in the out-of plane direction is achieved by total internal reflection.

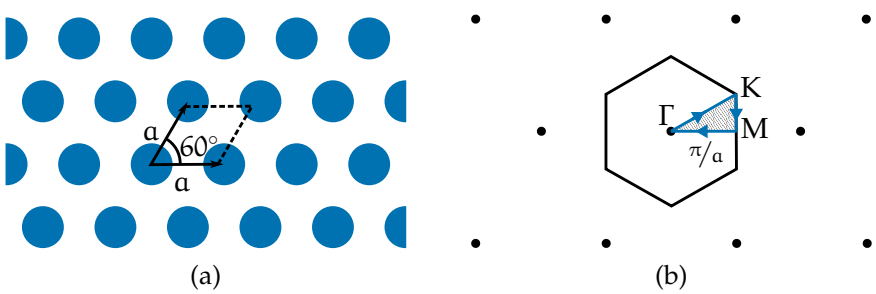

Figure 30: (a) 2D hexagonal PhC lattice with indicated unit cell and unit vectors and (b) corresponding Brillouin zone (black line) with path (blue) on which the ω-$\mathbf{k}$ dispersion relationship is calculated. The shaded region is the first irreducible Brillouin zone.

materials have scalar permittivity and that all materials are non-magnetic. That is

$$\overline{\overline{\epsilon}}(\mathbf{r}) = \epsilon(\mathbf{r}) \tag{16}$$

$$\overline{\overline{\mu}}(\mathbf{r}) = \mu_0 \tag{17}$$

4.2 PHOTONIC BANDS AND BAND GAP

Unsurprisingly, the unique optical properties that emerges from the periodic nature of PhCs are fundamentally governed by Maxwell's equations

$$\nabla \cdot \tilde{\mathbf{B}} = 0 \qquad \nabla \times \tilde{\mathbf{E}} + \frac{\partial \tilde{\mathbf{B}}}{\partial t} = 0 \tag{18, 19}$$

$$\nabla \cdot \mathcal{D} = \rho \qquad \nabla \times \tilde{\mathbf{H}} - \frac{\partial \tilde{\mathbf{D}}}{\partial t} = \mathbf{J}, \tag{20, 21}$$

where $\tilde{\mathbf{E}}$, $\tilde{\mathbf{D}}$, $\tilde{\mathbf{H}}$ and $\tilde{\mathbf{B}}$ are the complex electromagnetic field components. $\mathbf{J}$ is the current density and ρ is the charge density. It is convenient to assume that the materials are charge free. In materials where polarization and magnetization are linearly dependent on the $\tilde{\mathbf{E}}$- and $\tilde{\mathbf{H}}$ fields, the field components are related to each other by the permittivity tensor $\overline{\overline{\epsilon}}$ and the permeability tensor $\overline{\overline{\mu}}$ via the constitutive relations

$$\tilde{\mathbf{D}} = \overline{\overline{\epsilon}}\tilde{\mathbf{E}} \tag{22}$$

$$\tilde{\mathbf{H}} = \overline{\overline{\mu}}^{-1}\tilde{\mathbf{B}}. \tag{23}$$

For a source free ($\mathbf{J} = 0$ and $\rho = 0$), non-magnetic ($\mu = \mu_0$), loss less and isotropic ($\overline{\overline{\epsilon}}(\mathbf{r}) = \epsilon$ is real and scalar) dielectric material the following master equation can be derived [96]

$$\nabla \times \left(\frac{1}{\epsilon(\mathbf{r})} \nabla \times \mathbf{H}(\mathbf{r}) \right) = \left(\frac{\omega}{c} \right)^2 \mathbf{H}(\mathbf{r}). \tag{24}$$

Identifying this as an eigenvalue problem with $\nabla \times \left((\epsilon(\mathbf{r}))^{-1} \nabla \times \cdot \right)$ as the operator, we recognize $\tilde{\mathbf{H}}(\mathbf{r})$ as an eigenvector which defines the spatial field distribution, or *mode*, with a corresponding eigenvalue $\omega^2 c^{-2}$.

In accordance with Bloch's theorem, [97, 98] in a periodic medium such as PhCs (cf. eqs. (13) and (14)) the modes/solutions to eq. (24) must take the form

$$\tilde{\mathbf{H}}_k(\mathbf{r}) = e^{i\mathbf{k}\cdot\mathbf{r}} \tilde{\mathbf{u}}(\mathbf{r}), \tag{25}$$

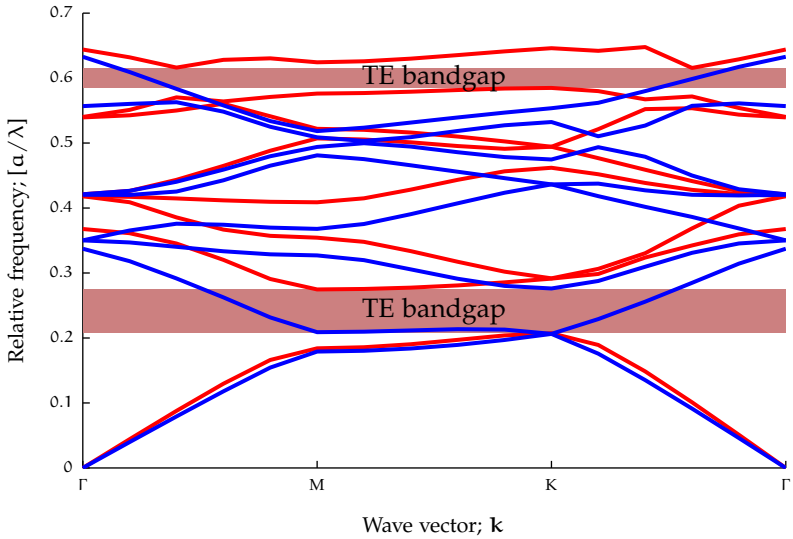

Figure 31: Example band diagram with TE bands in red and TM bands in blue. Calculated for a hexagonal 2D lattice of holes.

where $\mathbf{k}$ is the wave vector and $\mathbf{u}(\mathbf{r})$ is function with the same periodicity as the medium, that is

$$\tilde{\mathbf{u}}(\mathbf{r}+\mathbf{R}) = \tilde{\mathbf{u}}(\mathbf{r}). \tag{26}$$

In eq. (25), the subscript $_k$ has been introduce to indicate which wave vector the solution is valid for. This subscript can also be applied to the eigenvalues of eq. (24) to indicate the corresponding mode frequency ω_k. This relationship between eigenfrequency and wave-vector (i. e. $\omega(\mathbf{k})$) known as the dispersion relation and can be plotted. For a homogeneous, isotropic medium with refractive index n, this relationship is simply

$$\omega(k) = k\frac{c}{n} \quad \text{where} \quad k = |\mathbf{k}|. \tag{27}$$

A consequence of the Bloch theorem is that all solutions can be reduced to the so-called first irreducible Brillouin zone. [96] This zone exists in the reciprocal $\mathbf{k}$-space and for a two dimensional hexagonal lattice it is sketched in fig. 30b. Any solution for a $\mathbf{k}$-vector outside this zone is equivalent with a solution within the zone. This causes a folding of the dispersion relationship into this zone which gives rise to discrete bands in the dispersion relation. These can be enumerated such that for a given wave vector $\mathbf{k}$ there is a discrete, but infinite, number of modes $H_{k,m}$ with corresponding eigenfrequencies $\omega_{k,m}$.

When plotting the band diagram it is sufficient to consider the edge of the first irreducible Brillouin zone which can be

traced between the high symmetry points Γ-M-K as illustrated in fig. 30b. Any **k**-vector within can be decomposed into a sum of **k**-vectors along the boundary. In general eq. (24) with the requirement of eq. (25) and eq. (26) cannot be solved analytically. Solutions can be obtained computationally using methods such as finite-difference time-domain (FDTD) simulations or plane wave expansion method (PWEM). Doing so reveals the band structure. Figure 31 shows a typical presentation of the band structure with the wave-vector on the horizontal axis and the relative frequency on the vertical axis. The figure shows clear banding and the occurrence of a bandgap. Here only TE bands are shown, but an equivalent figure could just as well be made for TM bands.

Due to the scale invariance of Maxwell's equations eqs. (18) to (21) there is no inherent length scale and it is common and convenient to use the lattice constant a as the fundamental length unit. It is also common and convenient to use relative frequency in units $[a/\lambda]$, where λ is the free-space wavelength. Conversion from a relative frequency f_{rel} to actual frequencies f and free space wavelength λ follows

$$f = \frac{c}{a} f_{rel} \tag{28}$$

$$\lambda = \frac{a}{f_{rel}}. \tag{29}$$

Throughout following work the word "frequency" and the symbol f are used synonymously for for "relative frequency" and f_{rel} unless specifically noted.

4.3 PHOTONIC CRYSTAL SLAB STRUCTURE

In the special case of two-dimensional photonic crystal slab structures there is no translational symmetry in the out-of-plane direction and thus no PBG effect to provide vertical confinement. In stead, light is confined to the slab by total internal reflection.

The PhC dispersion relationship can be found by three-dimensional (3D) PWEM. Since this method requires periodicity in all dimensions the domain is extended above the slab and absorbing boundary layers are inserted. Light is confined in the slab if the in-plane wave vector $\mathbf{k}_{\parallel}$ fulfills the requirement

$$|\mathbf{k}_{\parallel}| < \frac{\omega_k n_{clad}}{c}, \tag{30}$$

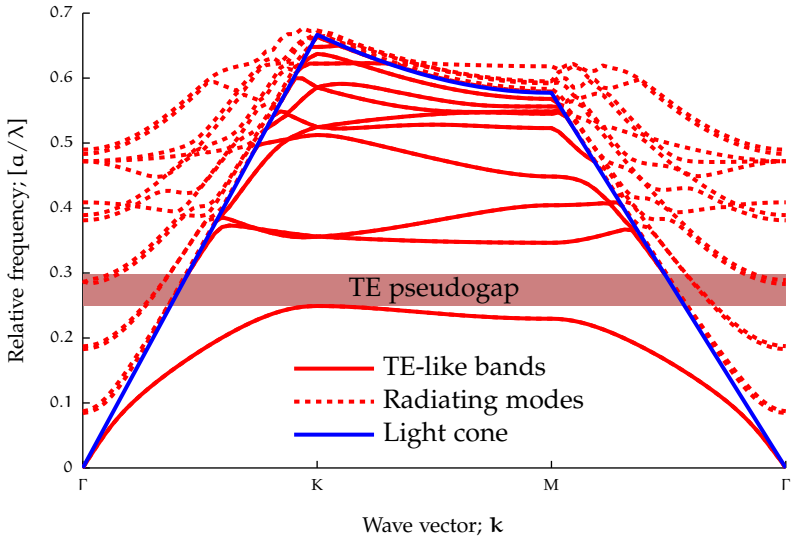

Figure 32: TE-like band structure for hexagonal slab PhC.

where n_{clad} is the refractive index of the cladding. This requirement is simply the dispersion relation of the cladding which for a uniform air or oxide cladding would follow is eq. (27). Thus, by solving the dispersion relation using PWEM and plotting along the edge of the first irreducible Brillouin zone as before, band diagrams for PhC slab structures can be obtained. The total internal reflection condition in eq. (30) can be visualized by overlaying it on the band diagram. Figure 32 shows the TE-like band structure of a slab with the light-cone drawn in. Strictly speaking, as the figure illustrates, the bands extend beyond the light cone, but becomes lossy. Under these conditions it is possible to obtain a band gap for all modes where $\mathbf{k}$ meets the total internal reflection condition of eq. (30). However, in the strictest sense it is only a pseudo bandgap since there are radiating modes inside the light-cone.

3D-PhC is the only truly physically rigorous form of PhCs which can have a complete band gap (i. e. there is a discontinuity in $\omega(\mathbf{k})\forall\mathbf{k}$.) The disadvantage of such structures is that they are difficult to fabricate, although that is an area of continuing research. [99–101] All structures considered here will be PhC slab structures and as such, from here on out the term PhC will be taken to mean PhC slabs.

4.4 CONFINEMENT AND CAVITIES

Cavities formed by defects in photonic crystal (PhC) slabs have demonstrated high Q-factor and sub-wavelength-scale mode

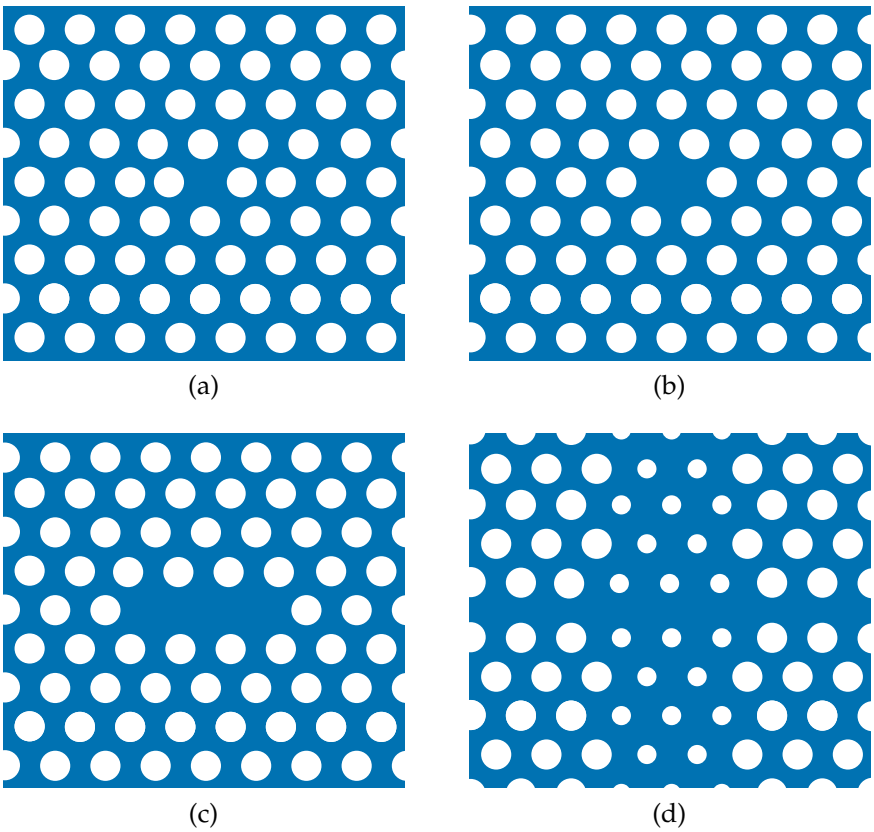

Figure 33: Example cavities in hexagonal 2D photonic crystal lattices that are assumed to extend into infinity. These are named (a) H0, (b) H1, (c) L3, and (d) Hetero structure line-defect.

volumes [102] making them attractive for applications such as cavity quantum electrodynamics [103, 104], low-threshold [105] and high-speed lasers [106]. For more than two decades, PhC technology has been maturing. Optically pumped PhC lasers were demonstrated at the end of the last century [107] and in recent years, electrically pumped PhC lasers have also been demonstrated [108–110].

Confinement in PhC structures can be achieved by photonic crystal cavitys (PhCCs). A PhCC can be constructed by introducing a defect into a PhC lattice, breaking the translational symmetry of the lattice. This can introduce one or more localized defect states/modes. Being localized implies that the mode's electromagnetic field decays to zero away from the defect.

The eigenfrequency and distribution of a mode can practically be found either using PWEM or FDTD calculations. Using the PWEM method, it is common to make a superlattice such as the one illustrated in fig. 0. If the supercell is sufficiently large

then coupling between adjacent cells is negligible and the solution on the super-cell is a good approximation of the cavity mode.

4.5 Q-FACTOR

One of the most important parameters for micro- and nano-cavities is the quality factor or Q-factor which is defined as

$$Q \equiv \omega \frac{\langle E_{cav} \rangle}{\langle P_{loss} \rangle}, \tag{31}$$

where ω is the angular resonance frequency, E_{cav} is the energy stored in the cavity and P_{loss} is the power loss, and $\langle \cdot \rangle$ indicates the time average over one cycle of the optical field. As can be understood from eq. (31), the Q-factor is a measure of relative energy loss. A high-Q cavity retains energy better than a low-Q cavity.

The Q-factor is also related to the resonance spectrum as the Q-factor is proportional to the line-width, through the relation

$$Q = \frac{\nu}{\delta\nu} \approx \frac{\lambda_0}{\delta\lambda}, \tag{32}$$

where ν is the eigen-frequency of the resonant mode with a corresponding free-space wavelength λ_0. $\delta\nu$ and $\delta\lambda$ are the FWHMs of the resonance spectrum in the frequency and free-space wavelength domains, respectively. The last approximation is valid when $\delta\nu \ll \nu$, which is true for all cases considered in this dissertation.

There are several methods for deriving the Q-factor from FDTD simulations. One is to monitor power loss through the simulation boundary and applying the definition of Q-factor eq. (31)

Another method is to monitor the energy at a

In general the Q-factor can be decomposed into arbitrary, independent loss vectors Q_i^{-1} in the manner

$$Q^{-1} = \sum_i Q_i^{-1}. \tag{33}$$

For instance, it is convenient to decompose the Q-factor into radiative losses Q_{rad}^{-1} (i. e. imperfect confinement) and material absorption Q_{abs}^{-1}

$$Q^{-1} = Q_{rad}^{-1} + Q_{abs}^{-1}. \tag{34}$$

For silicon photonics and telecommunication wavelengths, specifically C- and O-band, it is common to assume $Q_{abs} = \infty$ as these wavelengths correspond to energies lower than the silicon bandgap energy and thus ideally have zero absorption.

4.6 COMPUTER MODELLING AND SIMULATIONS

For non-trivial systems it is not possible to obtain analytical solutions to neither Maxwell's equations eqs. (18) to (21) nor the derived master equation eq. (24). Thus computational techniques are employed. Two popular methods are plane wave expansion method (PWEM) and finite-difference time-domain (FDTD). The former is suitable for periodic systems and gives steady-state solutions while the latter can be utilized to simulate in time domain any system where Maxwell's equations are valid.

The software used is the commercially available *CrystalWave* package version *4.8.2* from *Photon Design LtD* which implements both PWEM and the FDTD method.

4.6.1 *Plane wave expansion method*

The plane wave expansion method (PWEM) is a spectral method for solving certain differential equations with periodic constraints. It is commonly applied to solve the electromagnetic eigenvalue problem in eq. (24) for 2D and 3D PhCs. [111, 112]

The method utilizes the Bloch theorem (cf. eqs. (25) and (26)) and Fourier expansion of distribution of the dielectric permittivity in real space as well as the electromagnetic field in $\mathbf{k}$-space to construct a linear eigenvalue problem that can be solved using common numerical techniques.

Application on a PhC lattice typically gives band structures such as the ones previously shown in fig. 0. However, the technique can also be applied to super cells. In the next chapter, for instance, it is used to find the dispersion relationship along a line defect. Supercells work when the field is strongly located and the coupling between cells would be negligible (e. g. no travelling waves.) For slab PhC structures this supercell technique is exploited by setting the unit cell to the slab PhC plus some cladding and an absorbing layer, suppressing any non-negligible out-of-plane waves. [112, 113]

4.6.2 *FDTD*

To solve dynamic electromagnetic problems, the finite-difference time-domain (FDTD) method is commonly used. This method goes back to a seminal paper by Yee in 1966 [114]. In that paper and in the FDTD method, the simulation domain is defined by a discrete distribution of permittivity, permeability and conductivity on a staggered, regular mesh. To run the simulations Maxwell's equations are discretized into form that can be solved for each time step, at each grid point.

If the relationship between the time step and grid resolution is chosen correctly, the FDTD method is provable stable. [0] The main disadvantage of the FDTD method is an inherent anisotropy due to the rectangular grid. However, by using a sufficiently high resolution grid compared to the minimum feature size of the geometry and the wavelength of the electro-magnetic fields, it is possible to achieve a result that converges on the true solution of the problem.

The FDTD method is employed extensively in the following chapter for finding the mode distribution, mode volume and Q-factors.

4.6.3 *Cavity characterization*

The most pertinent parameters for a cavity are related to the spectral response. This can be obtained using either FDTD or PWEM. To utilize PWEM, a supercell technique can be used in a similar way as when calculating the band structure of a slab PhC. I. e. the cavity is assumed to be the atom of a periodic structure. By using a large enough supercell the coupling between neighbouring cavities is negligible and cavity modes will appear when calculating the band diagram. The disadvantage of this method is that while it does give on mode frequencies and mode profiles, it does not give any information on mode dynamics. For instance the Q-factor, which is a measure of energy loss from the cavity, can not be obtained. To obtain the mode dynamics, FDTD is a suitable option.

4.6.3.1 Q-*factor calculation*

The Q-factor is obtained by FDTD calculations recording the cavity response to a pulsed excitation. The excitation can be achieved using dipole sources, plane wave sources or any other

wave source. Which modes get excited depends on the overlap between the source's field and the mode field. For instance, a dipole placed at a node of a certain mode does not excite that particular mode. Using a broad bandwidth source, the entire spectral response of the cavity can be derived. Conversely, a narrow bandwidth source would enable targeted examination of a single mode. The disadvantage of this is that as the bandwidth decreases, the temporal pulse width increases which results in longer running times. Using dipole sources, it is also possible to tailor the excitation to maximize overlap with a specific mode-of-interest. For the simulations performed for this dissertation, dipole sources with sinusoidal pulse shape were used. Calculations were performed on the temporal field after the initial pulse. I. e. if the pulse had a duration t_p then any calculations such as discrete Fourier transform (DFT) would be performed for time $t > t_p$.

Although the spectral response can be calculated using DFT the spectral resolution is poor. Due to this, a Padé approximation with Baker's algorithm [115] (built into *CrystalWave*) was used. This algorithm ensure significantly higher spectral resolution than DFT for resonance spectrums at the cost of computation time.

5 PHOTONIC CRYSTAL CAVITY DESIGN AND OPTIMIZATION

Chapter 2 show that it is possible to realize InGaAs-on-silicon disk LEDs with wavelengths suitable for optical communication and silicon PICs. However, electrically pumped laser operation is necessary for InGaAs disks to be considered as a potential on-silicon light source. To achieve this, a first step is to consider the design and optimization of a suitable laser cavity. In this chapter the design and optimization of a compact photonic crystal cavity is considered.

Cavities formed by defects in photonic crystal (PhC) slabs have demonstrated high Q-factor and sub-wavelength-scale mode volumes [102] making them attractive for applications such as cavity quantum electrodynamics [103, 104], low-threshold [105] and high-speed lasers [106]. For more than two decades, PhC technology has been maturing. Optically pumped PhC lasers were demonstrated at the end of the last century [107] and in recent years, several electrically pumped PhC lasers have also been demonstrated [108–110, 116].

Despite small mode volumes, high-Q PhC cavities generally require a large number of PhC periods to provide strong confinement. This makes PhC cavities less suited for applications with strict area restrictions. Some designs such as PhC microdisks [117] and PhC nano-beams [118, 119] offer highly compact designs, but the geometry of these do not necessarily fit all applications. Recent simulation studies have investigated compact PhC cavities in optically thick slabs for electrically pumped laser applications [120]. Optically thick cavities can provide very high in-plane coupling efficiency for lasers [121]. However, as previously argued, thick laser devices may prove impractical for silicon photonics since silicon photonics is commonly implemented in thin device layers; typically 200~300 nm thick.

5.1 KEY CONSIDERATIONS

If the ultimate goal of a monolithic integration of a III/V laser with silicon is to be achieved using the InGaAs-on-silicon technology described in chapters 2 and 3, then it is necessary to

design a cavity which accommodates this geometry. To make an informed decision, a few key parameters should be established:

1. Disk geometry
2. Active region geometry
3. Figures of merit

These three will now be discussed individually.

5.1.1 *Disk geometry*

The disks presented in chapter 2 have a thickness of 1.0~1.5 um and diameter of approximately 8 um. However, this is arguably not an ideal size. Section 2.5 described the limitations on the InGaAs disk geometry in terms of the diameter 2A and the thickness h. Based on this, it is assumed reasonable that a diameter of 8 µm is achievable with a thickness in the range 200~300 nm. This thickness range is ideal for integration with silicon photonics as silicon photonic devices are most commonly implemented in SOI wafers with thin device layers. The most common thickness is 220 nm, but other thicknesses on the order of 200~300 nm are used and in several foundry processes multiple etch depths are allowed in the same chip. [122]Intuitively, by having the same or similar thickness, higher coupling efficiencies can be achieved than if there is a mismatch due to better overlap in the vertical direction between modes (e. g. InGaAs cavity to Si waveguide.) In summary, any cavity design aimed at InGaAs disks integrated with silicon photonics should meet the two requirements in table 8.

Table 8: Geometrical constraints of cavity.

Max. diameter	8 µm
Thickness	200 nm to 300 nm

5.1.2 *Active region geometry*

As illustrated in fig. 34, there are two options when it comes to the design of the device's active region. One is to grow a disk laterally to the desired size followed by vertical growth of the active region with a capping and contact layer on top. This

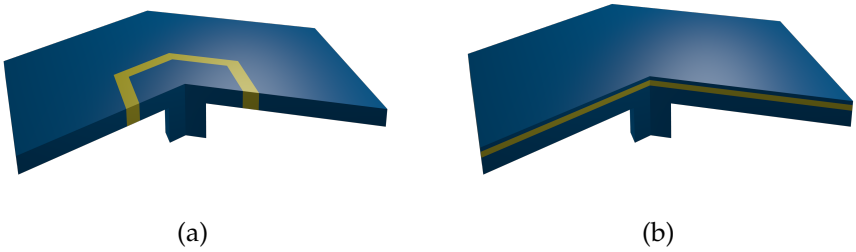

Figure 34: Cut-through sketch of the possible active region designs. The active region is indicated in yellow and the two possibilities are: (a) exclusively lateral growth to form a *vertical junction* and (b) lateral growth followed by vertical growth to form a *planar junction*.

gives a disk with a planar active region as shown in fig. 34b. The disadvantage of this junction geometry is that it would be perforated by the PhC holes creating a large surfaces of unterminated crystal bonds in the active regions. Even with perfect trapping of carriers in the active region (i. e. carriers are rapidly swept into the region without recombination) this could lead to significant non-radiative recombination near the surface. This is a recognized problem within the field of PhC lasers. [123]

The second option is to grow the disk laterally with a vertical active region with the result shown in fig. 34a. An initial growth of a basic *pn*-junction by S. Watanabe [90] showed that such junctions can be achieved. The advantage of such a junction is that the active region will not be penetrated by holes. Also, since the active region is more localized it should be possible to engineer a cavity with better mode overlap than for a lateral junction.

5.1.3 *Figures of merit*

For micro and nano laser performance there are many pertinent parameter such as Q-factor, mode volume, mode frequency, output coupling, and material parameters which are all interrelated and determine the laser performance in terms of threshold power, slope efficiency, wall-plug efficiency, line width, tunability and modulation speed. PhCC lasers have been hailed by some as the ultimate system for nano-lasers [105] (where *nano* refers to the mode volume more so than the total device size.)

For mm-range communication, the goal is to achieve the lowest energy cost per bit.

The focus here is solely on the design of a passive cavity for the potential future application in micro-disk lasers. As such, the pertinent, passive cavity parameters are Q-factor and mode volume. These are also the two very common figures of merits when designing PhCCs as is evident by a review of contemporary PhCC research.

One common reason for focusing on these parameters is due to the spontaneous-emission enhancement factor—also known as the Purcell factor after E. M. Purcell [124]. Based on assumptions of an ideal emitter in an ideal micro-cavity this factor can be derived from Fermi's golden rule to be

$$F = \frac{3}{4\pi^2}\left(\frac{\lambda_0}{n}\right)^3 \frac{Q}{V}, \tag{35}$$

where λ_0 is the free-space effective emission wavelength and n the refractive index in the cavity. Phenomenologically, the Purcell factor enhances the spontaneous emission rate $R_{sp} = \tau_{sp}^{-1}$ by

$$R'_{sp} = FR_{sp}. \tag{36}$$

Thus, the Purcell factor implies that increasing Q while decreasing V should increase the spontaneous emission rate and consequently lower the threshold current while increasing the modulation speed. However, due to the broad linewidth of bulk semiconductors, such as the as-grown InGaAs disks, the assumption of an ideal emitter is far from satisfied. It is argued that in such cases the Q-factor is not simply determined by the cavity value Q_{cav}, but should be replaced by [125]

$$Q^{-1} = Q_{cav}^{-1} + Q_{em}^{-1}, \tag{37}$$

where Q_{cav} is the cavity Q-factor and Q_{em} is the Q-factor of corresponding to the emission linewidth; that is $Q_{em} = \lambda_0 \delta\lambda_{em}^{-1}$. In such cases V will clearly be the dominant factor. The fact that V dominates the spontaneous emission rate has also been shown by Ni and Chuang [126] without the phenomenological application of the Purcell factor. They instead derived rate equations and a model for metal cavity nano-lasers directly from the Fermi's golden rule and show that the effect of the Q-factor does saturate. Interestingly their theoretical results indicate that the Q-factor has a larger effect on the threshold current in bulk

and quantum well (QW) lasers than in quantum dot (QD) lasers due to the relatively larger surface recombination lifetime used in their QD model. They also show that for high speed direct modulation, the modelled QD systems are optimal in terms of speed, but not necessarily in terms of energy per bit. Furthermore, saturation of Q-factor occurs at Q_{cav} values on the order of $10^2 \sim 10^3$ which is one to two orders of magnitude larger than $Q_{em} \sim 10^1$. This suggests that eq. (37) somewhat underestimates the effect of cavity Q-factor on spontaneous emission enhancement for systems where the emission linewidth is significantly broader than the cavity resonance linewidth.

Following this, a nano-laser with strong quantum effects is best realized by embedding narrow linewidth QD in the active region. However, it is not clear that QD are required for a practical nano-laser.

For mm-range communication, taking a desired bit-error rate of 10^{-9} and considering the thermal noise of the receiver gives a minimum energy per bit on the order of $\sim 1\,\mathrm{fJ}$. [41] Electrically pumped photonic crystal lasers are approaching this limit with Takeda et al. [116] having demonstrated a PhCC laser with $4.4\,\mathrm{fJ\,b^{-1}}$ at $10\,\mathrm{Gb\,s^{-1}}$. To achieve this regrowth forming a buried heterostructure was employed to alleviate thermal challenges. The cavity was a line defect type cavity with a Q-factor on the order of $\sim 10^5$ and mode volumes on the order of $(\lambda/n)^3$. This gives a good target for both the required Q-factor and the required mode volume for a practical laser. Another important aspect of this laser is a small active region volume and high current injection efficiency.

Consider the expression for the threshold power P_{th} of an optically pumped micro laser [41]

$$P_{th} \approx E_p \frac{N_0}{\tau_{carrier}} \left(\frac{V_{eff}}{\gamma_g \tau_{ph}} + V_a \right), \tag{38}$$

where E_p, N_0, $\tau_{carrier}$, τ_{ph}, γ_g, V_{eff} and V_a are the absorbed pump energy, transparency carrier density, carrier lifetime, photon lifetime ($\propto Q^{-1}$), characteristic gain rate, effective mode volume and the active region volume, respectively. From this it is clear that as in the Purcell relationship, maximizing Q/V is important. However, we note that a small active region is also important.

Another important consideration for waveguide coupled lasers is the waveguide coupling efficiency which can be defined as

$$\eta_{wg} \equiv \frac{\langle P_{wg} \rangle}{\langle P_{rad} \rangle}, \tag{39}$$

where P_{wg} is the power coupled into the waveguide mode and P_{rad} is the total radiated power from the cavity, and $\langle \cdot \rangle$ indicates the time average over one cycle of the optical field. Naturally, ideal coupling, $\eta_{wg} = 1$, is when all energy radiated from a laser cavity is coupled into the mode or modes of a photonic waveguide.

Looking at slab PhCCs the waveguide coupling coefficient depends on cavity geometry and the corresponding mode profile. It is often the case that the radiated light does not match the waveguide mode very well and consequently couples very weakly to waveguides. As such it is necessary to engineer the mode to better match the desired waveguide mode. This is can be done by introducing near the cavity a PhC line defect near with a transmission band overlapping the desired resonant cavity mode [127, 128]. This introduces a new loss vector as energy can flow into the line defect and be guided elsewhere. Assuming that the cavity without any waveguide to couple to has an intrinsic Q-factor Q_0 and that the introduction of a line defect introduces an energy loss vector quantified by Q_{wg} then the total, measured Q-factor should, according to eq. (33), be given by

$$Q^{-1} = Q_0^{-1} + Q_{wg}^{-1}. \tag{40}$$

By the definition of waveguide coupling efficiency η_{wg} in eq. (39) and Q-factor in eq. (31) we easily see that the coupling efficiency can be written in terms of Q-factor as

$$\eta_{wg} = \frac{Q}{Q_{wg}}. \tag{41}$$

However, since Q_{wg} cannot be measured directly, it is convenient to rewrite eq. (41) using eq. (40) yielding

$$\eta_{wg} = 1 - \frac{Q}{Q_0} \tag{42}$$

As argued and demonstrated by Faraon et al. [128], this equation is convenient as Q is the measured Q-factor of a coupled

cavity and Q_0 can be measured from an un-loaded reference cavity or a cavity where the waveguide coupling is negligible, but measurable.

It is clear from eq. (42) that in order to maximize coupling (i. e. all radiated optical energy is captured), it is necessary to minimize Q/Q_0 which implies $Q_0 \gg Q$. Moreover, regardless of the required Q, the ideal case is when Q_0 tends toward infinity.

It is worth noting that this derivation is not general but only applies to cavities where eq. (40) is valid. That is, where Q_0 and Q_{wg} are independent. Here, independent means that there is no configuration where a non-negligible amount of power can couple into a waveguide while the cavity Q-factor remains unperturbed (i. e. $Q = Q_0$.) This is a good assumption for PhCCs as they often have an omnidirectional radiation pattern in the plane, but there are other geometries where this is not the case.

One example is conventional FP ridge waveguide cavity lasers. In such cavities, the imperfect reflectivity of the mirror facets is the major contributor to radiative loss. Thus in a geometry with laser and PIC waveguides butt coupled, careful mode matching between the laser and PIC waveguide can enable high coupling efficiency. On the micro- and nanometer scale, metal nano cavities often have metal on five out of six sides and thus radiates into one hemisphere and efficient coupling can be achieved in theory as it is intuitively easier to engineer the collection of radiation from such a directional source rather than an omnidirectional source—practical implementation though remains challenging. Kim et al. [129] have presented simulations of metal cavities and silicon waveguides with coupling efficiencies of 78 % with Q-factor of 630. It is important to note that this *coupled* Q-factor is comparable to the reported intrinsic value of $Q_0 = 1700$. As will be evident shortly, this is an advantage of metal cavities compared to compact PhCC. These values clearly illustrates a case where the previously derived formalisms do not applied as this Q_0 and η_{wg} would, according to eq. (42) imply a loaded Q-factor of

$$Q^{metal} = Q_0(1 - \eta_{wg}) \approx 370, \tag{43}$$

which is significantly lower than the reported $Q = 630$. Conversely, to achieve a coupling efficiency of 78 % and $Q = 630$ in a PhCC by the introduction of a line defect it is necessary to design a cavity with an intrinsic Q-factor of

$$Q_0^{PhCC} = \frac{Q}{1 - \eta_{wg}} \approx 2900. \tag{44}$$

This illustrates the importance of Q-factor in PhCCs geometries compared to metal cavities when considering coupling efficiency.

There are other areas where is important such as in dense wavelength division multiplexing (DWDM) applications where Q-factor is one of the factors determining how closely wavelength division multiplexing (WDM) channels can be packed. State-of-the-art DWDM standards and systems have channel spacings as tight as 12.5 GHzwhich around a center wavelength of 1550 nm corresponds to a channel width of 0.1 nm. Even in the optimistic case where the channel width corresponds to the allowable source linewidth this would imply loaded Q-factors greater than 7.5×10^3.

Although this section has not provided a definite answer for the desired Q-factor or mode volume, simply the coupling argument should make it clear that it is desirable to maximize it regardless. Practical applications may require high Q-factors. With regards to the quantum effects, mode volume is the dominant factor and should be minimized. However, mode volume is more of a product of the cavity design and corresponding mode profile and it will not be a major focus of optimization.

5.2 THE HYBRID CAVITY

Despite small mode volumes, high-Q PhC cavities generally require a large number of PhC periods to provide strong confinement. This makes PhC cavities less suited for applications with strict area restrictions. Some designs such as PhC microdisks [117] and PhC nano-beams [118, 119] offer highly compact designs, but the geometry of these do not necessarily fit all applications. Recent simulation studies have investigated compact PhC cavities in optically thick slabs for electrically pumped laser applications [120]. Optically thick cavities can provide very high in-plane coupling efficiency for lasers [121]. However, for some systems, such as silicon photonics, thick laser devices may prove impractical since silicon photonics is commonly implemented in thin device layers; typically 200~300 nm thick.

Figure 35 shows a novel PhCC design which aims to address the challenges of fabricating a cavity in the InGaAs system. It is inspired by heterostructure line-defect cavities which have the largest reported theoretical Q-factors of any PhCC with $Q \sim 10^9$[130]. However, since these are line defect heterostruc-

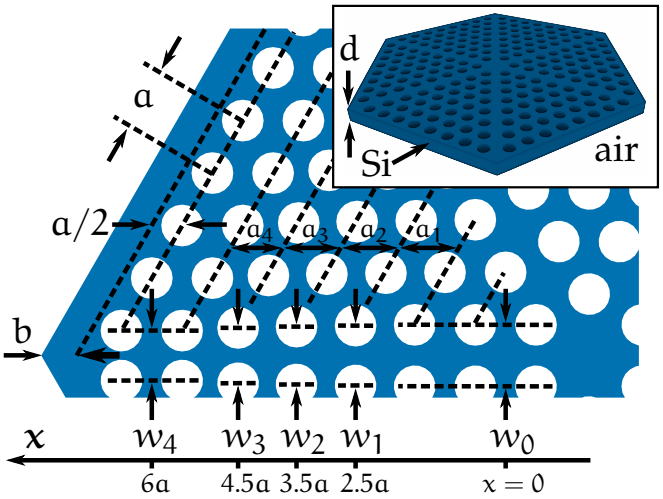

Figure 35: Schematic of cavity corner with full cavity model in inset. Confinement is achieved by modulating the line-defect widths $w_0 \ldots w_4$ at the indicated x positions. By perturbing the the separation $a_1 \ldots a_4$ between the indicated hole arrays, six-fold rotational symmetry is maintained.

ture cavities, they would intersect with the central post of the InGaAs islands. This is considered a major disadvantage for a few reasons. First of all, the center is InAs which has a narrower bandgap than InGaAs, with band-to-band recombination emitting light at 3.5 µm. Due to this InAs post, the slab symmetry is also broken in this region, this modifies the PhC band diagram and even- and odd- modes become indistinguishable (i. e. they seize to be transverse electric (TE) and transverse magnetic (TM) approximations.) This causes excessive losses. [131] Intuitively this can be considered to be due to the InAs post being near impedance matched to the InGaAs and thus acts as a low-impedance leak path for the optical field, weakening confinement.

Furthermore, to best exploit the island's limited area, the cavity symmetry should match the island's six fold rotational symmetry. Since the H1 cavity matches the island symmetry better, we sought to combine these two designs into a novel hybrid design. Effectively, this design is created by combining three photonic crystal line defects, intersecting at 60° separation in the center of the island. We call this a hybrid cavity due to the similarities with both line-defect cavities and hole-defect cavities. A hetero-structure can be formed by modulating $b_1, b_2, \ldots, b_N$ in the direction perpendicular to the island edge while keeping the hole spacing a constant in the parallel

direction. As illustrated, this is also equivalent to modulation of the waveguide width w.

5.3 SIMULATION TOOLS

The simulations presented here were carried out using the commercial software tool *CrystaWave 4.8.2* from *Photon Design LtD*. This tool supports both FDTD and PWEM simulations in both two and three dimensions. All FDTD simulations were performed on a square mesh with a resolution of $a/30$.

5.4 BASIC PARAMETERS

To simplify the optimization process and to stay within the conventions of PhC research, a simplified model of the disks is used. First, the refractive index is chosen as $n_{slab} = 3.48$ which matches silicon at a free-space-wavelength of 1.55 µm. Since the composition of InGaAs is not yet well understood and thus the exact refractive index is unknown, silicon is assumed as a prototype analogue to InGaAs.refractive index of

For the first part, the cladding and holes are assumed to be air/vacuum with the refractive index $n_{clad} = 1$. This is a rather un-physical model as it assumes a silicon disk suspended in air. If there is a central post or some other support that have minimal effect on the cavity mode, then this air clad structure could still be realized although the break in symmetry is expected to affect the cavity properties. The case of a glass cavity will be discussed later in section 5.9.

5.5 LATTICE

The PhC lattice was chosen to be a hexagonal lattice with circular holes filled with the same material as the cladding. This matches the lattice previously illustrated in fig. 30a. One reason for choosing this lattice is that it has the same six-fold rotational symmetry as the hexagonal disk. Also, in two dimensions, a hexagonal lattice with circular air holes has a significantly larger TE bandgap than a comparable square lattice with circular air holes [96, Appendix C]. More exotic hole and pillar shapes have been investigated for various purposes and circular holes do not necessarily represent the optimal structure

for maximizing the bandgap [132, 133]. However, circular holes and pillars remain common due to ease of fabrication.

The hole radius is set to $r = 0.323a$. These parameters were chosen to give a large relative bandgap around the common C-band wavelength $\lambda = 1.55\,\mu m$ when $d = 260\,nm$. At the same time, scaling to these dimensions, the cavity has a corner-to-corner diameter $2A$ of less than $8\,\mu m$. This scaling is used as a reference here, but note that scaling to a more common thickness of $220\,nm$ would yield a resonance in the O-band at $1.31\,\mu m$ wavelength and a diameter of less than $6.8\,\mu m$.

5.6 OPTIMIZATION

From the definition eq. (31), the Q-factor is maximized by minimizing the radiative loss. For a slab PhCC it is convenient to decompose the Q-factor into

$$Q^{-1} = Q_{\perp}^{-1} + Q_{\parallel}^{-1}, \tag{45}$$

where $Q_{\perp}^{-1}$ represents the out-of-plane loss and $Q_{\parallel}^{-1}$ represents the in-plane loss. The optimization strategy is to first consider out-of-plane loss by the application of the gentle confinement method and then in-plane loss by boundary considerations.

5.6.1 *Gentle confinement method*

It is well understood that the vertical loss from a PhC slab can be minimized by minimizing the components that fall inside the light cone in k-space [134] which is obtained by the spatial Fourier transform of the field distribution at the surface [135, 136]. A general gentle-confinement method has been established for designing ultra-high-Q line-defect cavities [130, 137]. Since the cavity as shown in fig. 0 can be considered composed of three crossed line-defects, it seems natural to utilize this method of optimization.

This method minimizes the components within the light cone by ensuring that the electric field at the cavity surface has a Gaussian envelope $E_{env} \propto e^{-Bx^2}$, thus reducing out-of-plane loss. This is achieved by recognizing that non-propagating waves decay according to $E_{env} \propto e^{-qx}$. Equating these two expressions we see that a mode with a Gaussian envelope is formed when

$$q = B|x| \tag{46}$$

is satisfied. Here, x is the position along the line-defect and B determines the sharpness of the Gaussian envelope. Practically, this means that a cavity with a Gaussian mode profile can be constructed from sections of line defects where the central section supports a propagating mode ($q = 0$) at the desired resonance wavelength while the surrounding sections attenuate with an attenuation coefficient which satisfies Eq. (46).

Taking the method as presented by Tanaka et al. [130] and Welna et al. [137], we refine it into the following five-step algorithm:

1. Choose slab thickness, lattice constant and hole radius
2. Calculate dispersion relation $f_w(\mathbf{k} = k\hat{\mathbf{e}}_x)$ for various line-defect widths w, where $\hat{\mathbf{e}}_x$ is parallel to the defect, k is the wave number and f_w the optical frequency.
   - For each $f_w(k)$, fit a polynomial that is symmetrical around $k = \pi a^{-1}$
3. Substitute $k = (\frac{1}{2} - iq)2\pi a^{-1}$ to get $f_w(q)$ [130].
4. For the desired resonance frequency f_{res}, extract the $q(w)$ that satisfies $f_w(q(w)) = f_{res}$
   - Fit polynomial on $q(w)$ for analytical expression.
5. The inverse relationship $w(q = B|x|)$ fulfills eq. (46) and gives $w(x)$.
   - $w_0 = w(0)$ given where $q = 0$

This algorithm is illustrated by fig. 36 where the plane wave expansion method (PWEM) is used with the domain in fig. 36a to calculate the dispersion relation corresponding to item 2. By fitting with a symmetric polynomial around around $k = \pi a^{-1}$ only the zero dispersion waves at the Brillouin zone boundary are accounted for. Furthermore, since $f_w(k)$ from item 2 is symmetrical around πa^{-1}, the substitution $k = (\frac{1}{2} - iq)2\pi a^{-1}$ gives a purely real expression which gives $f_w(q)$: the general relationship between frequency and attenuation for waves at the Brillouin zone edge. This is illustrated in fig. 36c. To perform item 4, a horizontal line is drawn through this figure. The line is placed at the desired design resonance frequency and gives $q(w)$: the attenuation of a wave decaying along a line defect with width w at the resonance frequency. This relationship is plotted in fig. 36d.

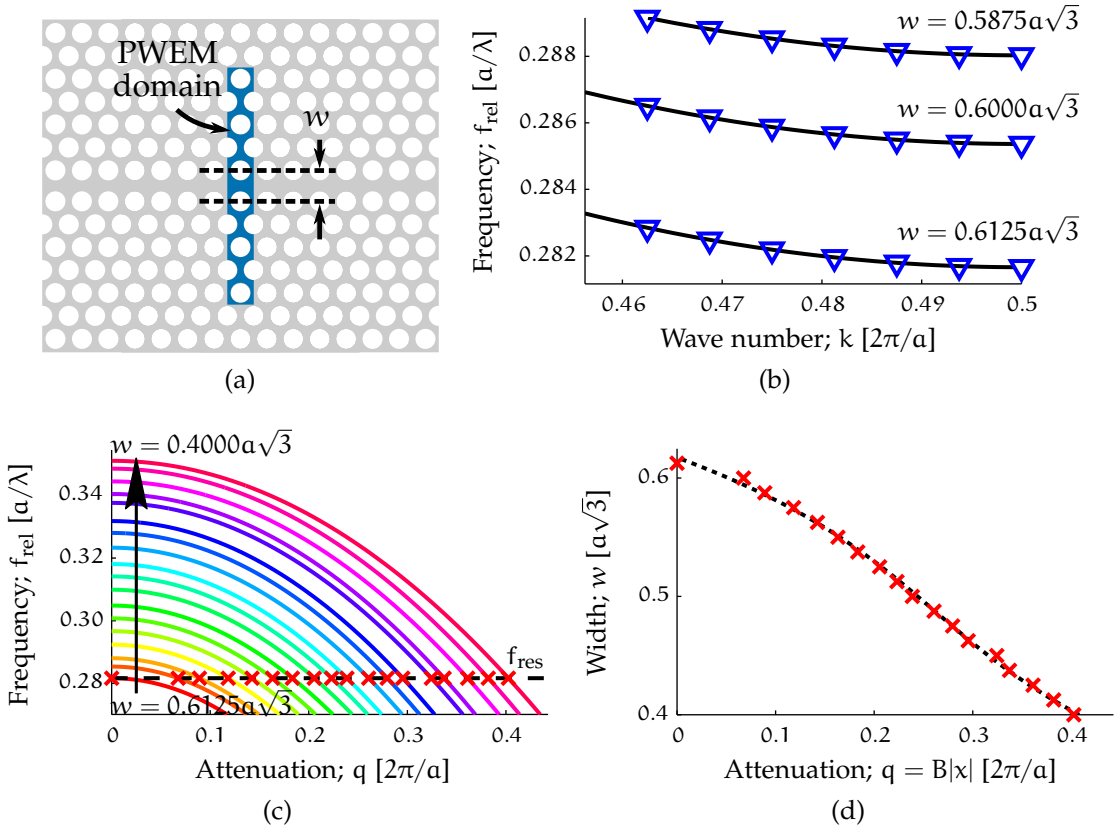

Figure 36: Algorithm for gentle confinement method on line-defect hetero structures. (a) the idealized domain used for the PWEM to calculate (b) the dispersion relation for various widths w. This gives (c) the attenuation relation with the horizontal line indicating the desired resonance frequency; the intersection points give (d) the design equation.

The final item 5 is trivial and gives $w(x)$ with a free design variable B which determines the envelope shape. w_0 can be directly read from fig. 36d as the zero-attenuation point $w_0 = w(x = 0) = w(q = 0) \approx 0.617\sqrt{3}a$. Choosing a value for the free design variable B in $w(x)$ is equivalent to fixing one of the variables $w_1 \ldots w_4$. It is convenient to use w_4 and to refer to this as tapering strength since choosing $w_4 = w_0$ gives no tapering from w_0 to w_4 (and $B = \infty$) while smaller values of w_4 give progressively steeper tapering of $w_0 \ldots w_4$. The effect of tapering strength will be investigated and discussed.

This algorithm is general to heterostructure line-defect cavities and not specific to this cavity design. Furthermore, it is not limited to optimization on the line-defect width w. It can be utilized with any parameter that modifies the dispersion relation (e.g. hole shift [137], lattice constant [130], refractive index modulation [138] etc.) This algorithm is based on the work of Tanaka et al. [130] and Welna et al. [137], but it differs in that it does not assume constant coefficients (i.e. independent of w) for the fitted dispersion-relation polynomial.

5.6.2 *Boundary optimization*

Next, to maximize the total Q-factor we optimize the in plane confinement by finding the optimum boundary width b. Previous research [121] has used coupled mode theory to explain the dependence of Q-factor on boundary width in optically thick slabs with an incomplete photonic bandgap (PBG) where the mode is dominated by plane waves in the Γ-M directions. This view shows some promise, but relies on an unknown phase factor and it is not directly transferable to cavities which rely on the PBG for confinement.

To reduce the optimization search space for optimal b a simplified model as shown in fig. 37 is used. This figure shows the boundary region and the surrounding PhC and air regions. In the PhC region, the approximated position of the cavity mode's nodes are indicated based on qualitative observations of the mode profile of published heterostructure line-defect cavities [130, 139]. For the phase to be conserved along the interface between the PhC and boundary regions, any propagating or standing waves in the boundary region must be perpendicular to the interfaces. This gives rise to a Fabry-Pérot (FP) resonance as indicated in the figure. Consequently, as is known for FP cavities, the cavity loss is maximized when the cavity round trip

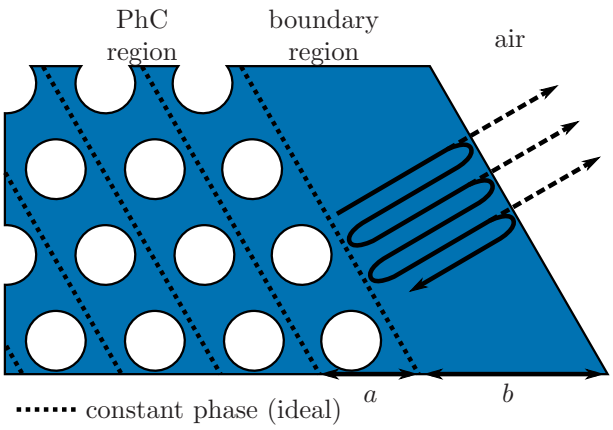

Figure 37: Simplified Fabry-Pérot model of the boundary region.

length is an integer multiple of the wavelength. Thus the first minimum occurs at a boundary width of

$$b_{poor} = \frac{2}{\sqrt{3}} \times \frac{\lambda_s}{2}. \tag{47}$$

The first term is a geometrical term relating the boundary width b to the actual propagation length while the second term ensures one wavelength phase shift per round trip.

Conversely, the best case for the confinement of light corresponds to minimized transmission through the FP structure. Conventionally this corresponds to a round trip distance of $m\frac{1}{2}\lambda_s$ where m is odd. Thus, the first optimum should occur at a boundary width of

$$b_{opt} = \frac{2}{\sqrt{3}} \times \frac{\lambda_s}{4}. \tag{48}$$

The wavelength λ_s in the boundary region is derived under the assumption that the effective refractive index in this region corresponds to that of the fundamental mode of an air-clad silicon-slab waveguide with thickness $d = 0.6a$. Such a slab can easily be shown to have a fundamental mode with a wavelength of approximately $1.2a$ for a free space wavelength of $\lambda_0 = 3.55a$ (cf. f_{res} in fig. 36c) [42]. This gives in numerical terms

$$b_{opt} \approx 0.35a \tag{49}$$

and

$$b_{poor} \approx 0.69a, \tag{50}$$

for the presented case.

5.7 OPTIMIZATION RESULTS

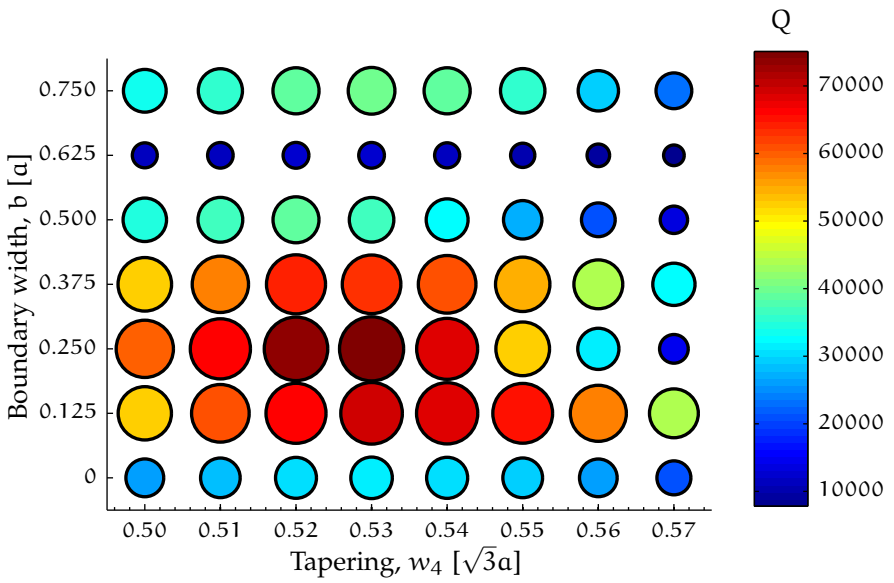

Figure 38: Q-value as a function of tapering w_4 and boundary width b.

The number of design parameters has now been reduced to two, w_4 and b. These determine the tapering of the line defect and the boundary width, respectively (cf. fig. 35). We calculate the Q-factor using FDTD for various values of w_4 and b and map the result in fig. 38. This figure shows strong dependence of Q on both w_4 and b with a peak value of $Q = 75\,100$ at $w_4 = 0.53\sqrt{3}a$ and $b = 0.25a$. This is comparable to other cavities of similar size [121]. A minimum $Q = 7500$ is found at $w_4 = 0.57\sqrt{3}a$ and $b = 0.625a$.

To elucidate these results we estimate the out-of-plane $Q_\perp$ of the cavity by surrounding it with lattice matched PhC and calculating the Q-factor. The Q-factor can then be decomposed into $Q_\parallel$ and $Q_\perp$ according to eq. (45). Our approximation of $Q_\perp$ is valid as long as the field distribution is not significantly perturbed which we believe to be a reasonable assumption. However, even in the case of the field being significantly perturbed, the separation of Q into $Q_\parallel$ and $Q_\perp$ according to eq. (45) is still valid, but the interpretation of the parameters changes. $Q_\perp$ should then be considered a measure of ideal confinement, while $Q_\parallel$ represents the induced losses due to the boundary. These losses are not necessarily confined to the plane.

Figures 39a and 39b shows the dependence of the decomposed Q-factors on w_4 at $b = 0.625a$ and $b = 0.25a$, respec-

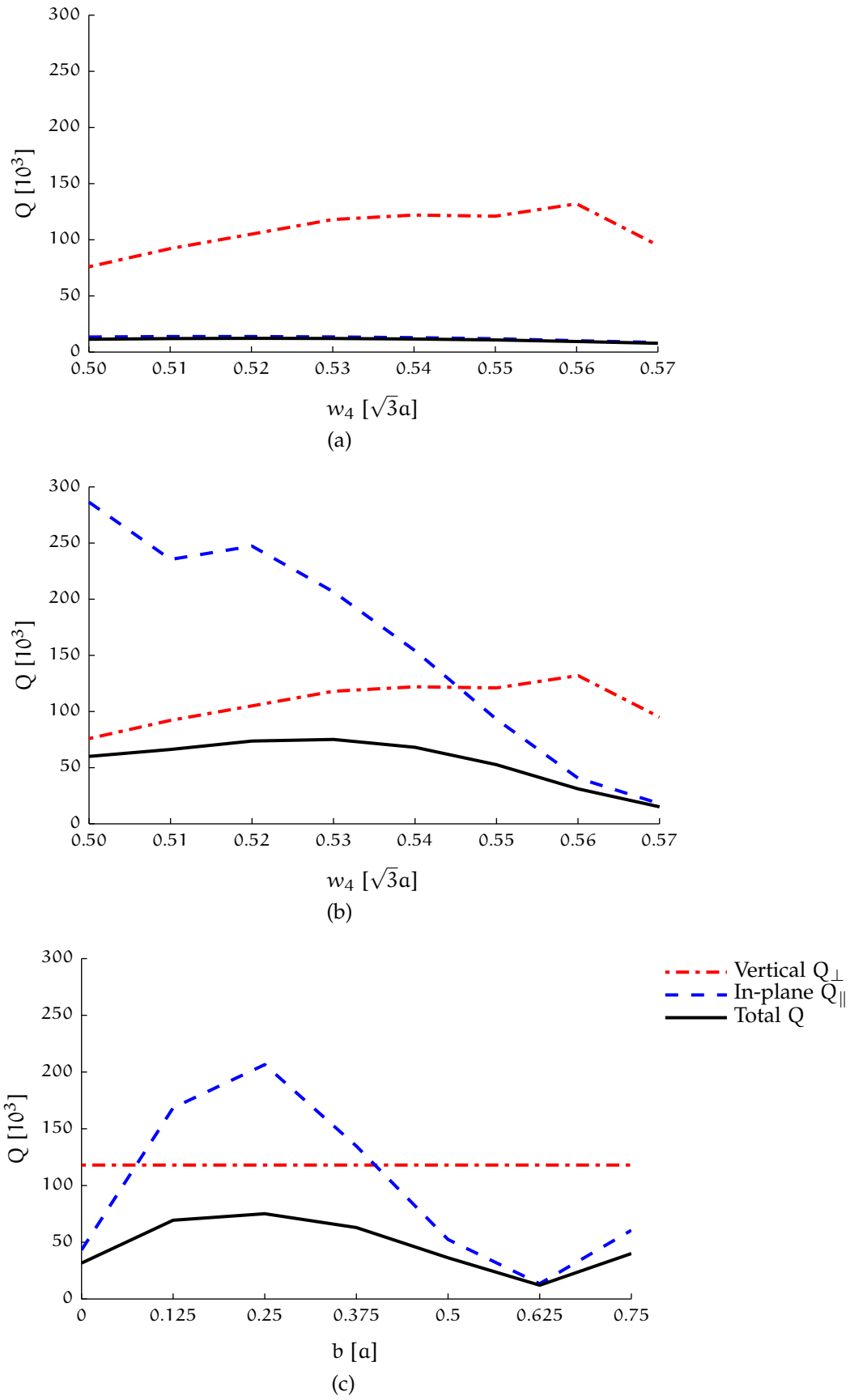

Figure 39: Total Q-factor decomposed into $Q_{\parallel}$ and $Q_{\perp}$ as a function of w_4 for (a) the low-Q case of $b = 0.625a$ and (b) the high-Q case of $b = 0.25a$; and (c) as a function of b in the high-Q case of $w_4 = 0.53\sqrt{3}a$.

tively. Both show that there exists an optimum w_4 between the extremes. This seems reasonable as a small value should result in a sharp envelope which, according to gentle confinement theory, should have larger losses. On the other hand, for large values of w_4, the field is not sufficiently confined and there should be significant scattering loss at the corners. This is supported by the high-Q case in fig. 39b which shows strong dependence of $Q_{\|}$ on w_4.

Next, fig. 39c shows the dependence of $Q_{\|}$ on b when $w_4 = 0.53\sqrt{3}a$. The shape of this curve is reminiscent of that for Fabry-Perot cavities and indicates support for the periodic nature of both of the proposed approaches. Peak $Q_{\|}$ is found at at $b = 0.25a$ and a minimum at $b = 0.625a$. This is smaller than the predicted values of $0.35a$ in eq. (48) and $0.69a$ from eq. (47), respectively. This is a significant deviation, however, taking the difference between the first maximum and minimum:

$$\Delta b = b_{poor} - b_{opt}, \tag{51}$$

we get $0.34a$ the FP model and for the simulation $0.375a$. This is a relatively small deviation of 10% which suggest that the FP model has some merit. The inaccuracies of the model can be attributed to the definition of $b = 0$. Defining it at the midpoint between two rows of holes seem intuitive, but is fundamentally arbitrary. This would shift the absolute values of b_{opt} and b_{poor}. Furthermore, at the PhC/boundary-region interface a phase shift of 0–180° depending on the complex wave vector of the cavity mode is to be expected [140]. This would modify the effective round trip length reducing both b_{opt} and b_{poor}. Finally, the FP model is only suggested as a first approximation as it is fundamentally one-dimensional disregards the complex geometry of the boundary region as well as the complex mode profile of the PhC cavity mode. However, both the model and the simulation results show the same trend of $Q_{\|}$ increases as b increases from $b = 0$ to a maximum before a minimum. By taking this into account when performing boundary optimizations it is possible to greatly reduce the optimization search space of b.

Figure 40 should further clarify the mechanism behind the boundary loss. It shows the logarithm of the optical intensity distribution ($I \propto |E|^2$) at the cavity surface. Comparing the high-Q cases of $b = 0.25a$ in Figure 40a–c with the low-Q cases of $b = 0.625a$ in Figure 40d–f, it appears that there is an increased optical intensity in the boundary region which gives rise to in-

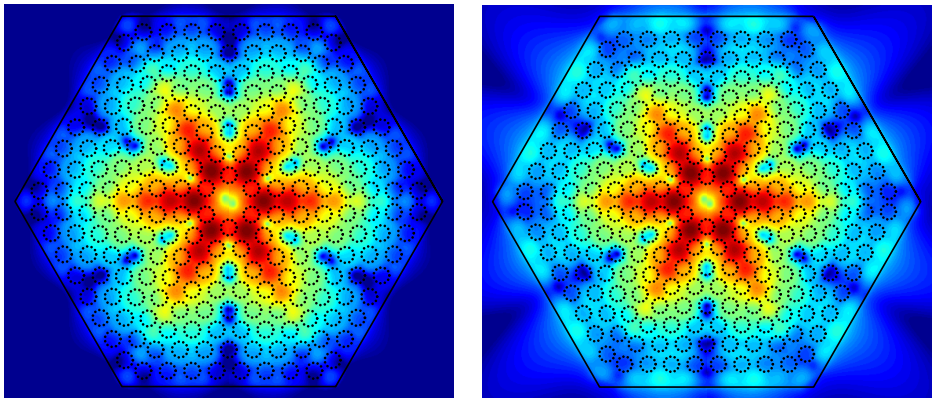

(a) Q = 60 000

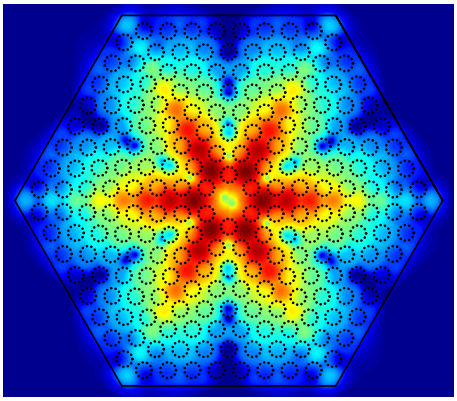

(b) Q = 75 100

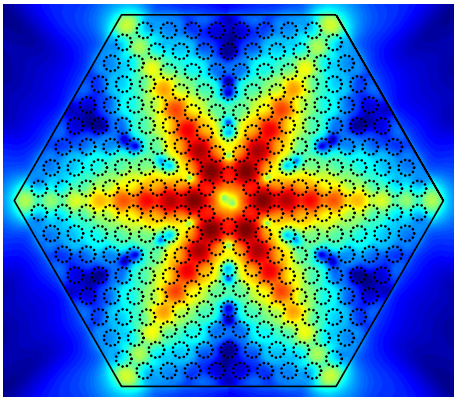

(c) Q = 15 100

(d) Q = 11 400

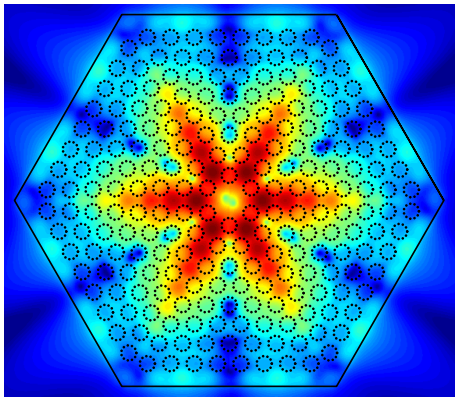

(e) Q = 12 100

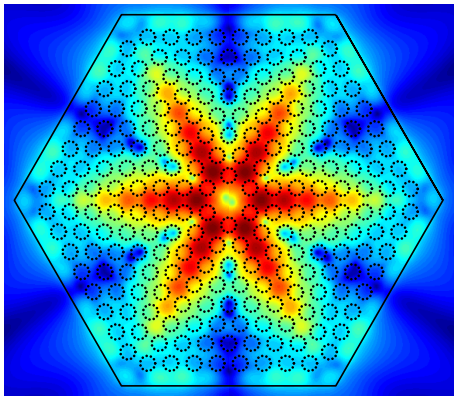

(f) Q = 7800

Figure 40: Logarithm of the optical intensity at the surface of the cavity for the high-Q cases of $b = 0.25a$ with (a) $w_4 = 0.50\sqrt{3}a$, (b) $w_4 = 0.53\sqrt{3}a$, and (c) $w_4 = 0.57\sqrt{3}a$; as well as the low-Q cases of $b = 0.625a$ with (d) $w_4 = 0.50\sqrt{3}a$, (e) $w_4 = 0.53\sqrt{3}a$, and (f) $w_4 = 0.57\sqrt{3}a$.

creased losses. Looking only at the high-Q case of $b = 0.25a$ in fig. 40b and fig. 40c it also appears clear that when the boundary thickness is optimal, increasing w_4 weakens the mode localization, increasing the field strength near the corners which in turn increases scattering loss. While scattering from the corners is not confined to the xy-plane, it is accounted for in the $Q_{\|}$-term in eq. (46). This explains why $Q_{\|}$ decreases when w_4 increases in fig. 39b.

Finally, to properly verify that the gentle confinement method is effective, it is useful to study the k-space distribution of the field. Figure 41 shows this distribution in three different cases for the three field components H_z (out-of-plane), and E_x and E_y (in-plane). The indicated circles mark the boundary of the light cone and it is clear that the optimization method is effective in reducing the field components lost to total internal reflection. It is interesting to note though that there is no significant discernible difference between the case of $b = 0.250a$, $w_4 = 0.57\sqrt{3}a$, $Q = 15\,100$ in figs. 41a to 41c and the case of $b = 0.250a$, $w_4 = 0.53\sqrt{3}a$, $Q = 75\,100$ in figs. 41d to 41f. This indicates that the major cause of loss in the low-Q case would be induced scattering and not de-localization of the mode.

5.8 WAVELENGTH PREDICTABILITY

One key advantage of the gentle confinement method is wavelength predictability. Figure 42 shows frequency as a function of tapering strength w_4. The error bars indicate the maximum deviation when changing the boundary width. This deviation is less than 0.04% for all values of w_4. This corresponds to less than 0.5 nm deviation when the cavity is scaled to a design resonance wavelength of 1538 nm.

At peak Q ($w_4 = 0.53\sqrt{3}a$) the simulated cavity has a relative resonance frequency of $f_{res} = 0.2802$ which is lower than the design target of 0.2817. This 0.5% deviation corresponds to a wavelength error of 8 nm when the cavity is scaled to a design resonance at 1538 nm.

This deviation can be explained by three effects. First, as Figure 36d shows, there is a small discrepancy between the calculated $w(q)$ and fitted $w(q)$ at $q = 0$. This introduces an error as it is the fitted $w(q)$ which is used for the design. Second, the PWEM calculations on the super-cell in fig. 36a assumes that the domain is infinitely periodic in all three dimensions and has a constant lattice constant a and defect width w. This is not

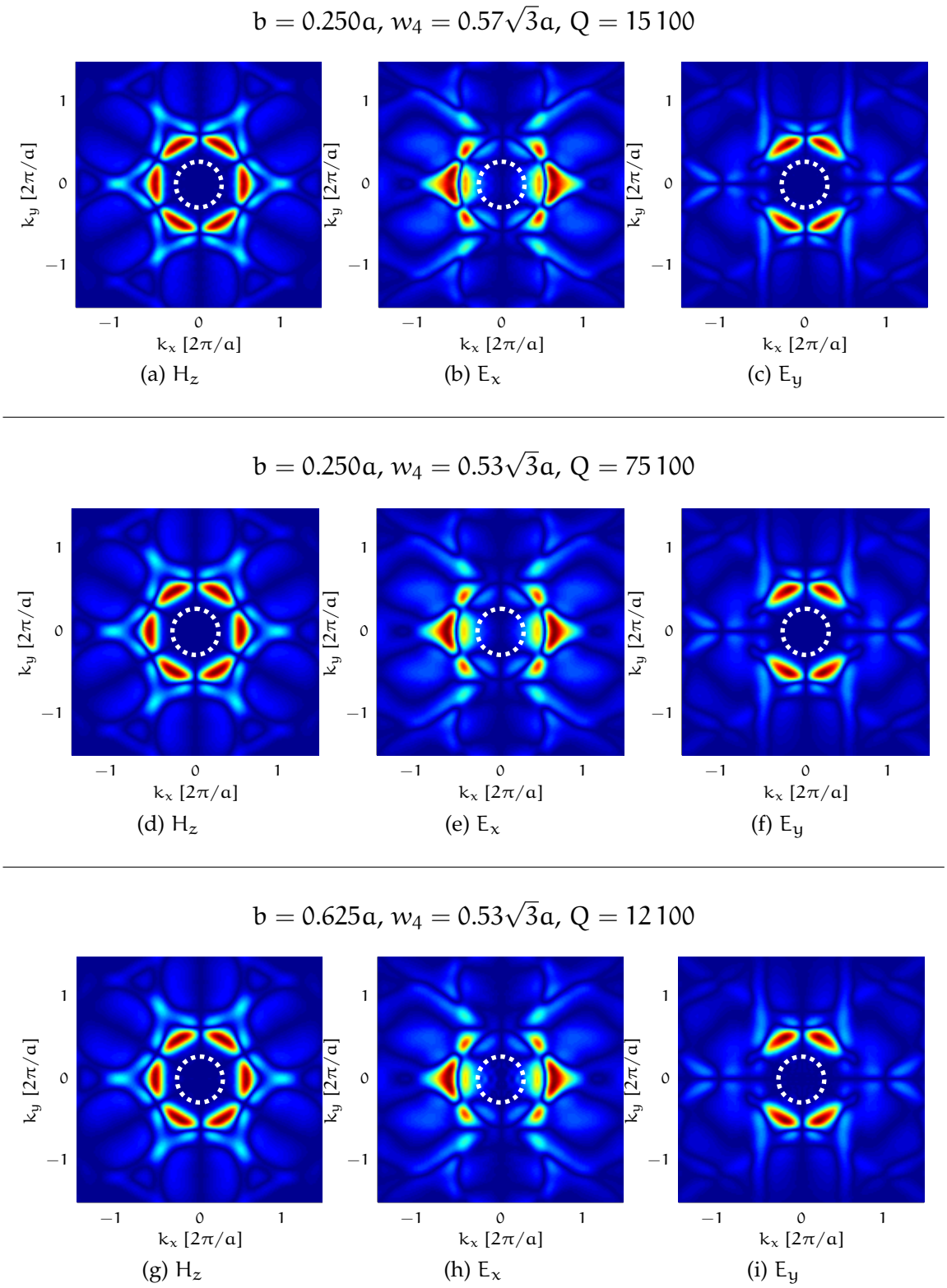

Figure 41: k-space distribution of field components E_x, E_y, H_z at the surface for (a)–(c) a low-Q case with optimum boundary, (d)–(f) the high-Q case and, (g)–(i) the case of high $Q_\perp$ and low $Q_\parallel$.

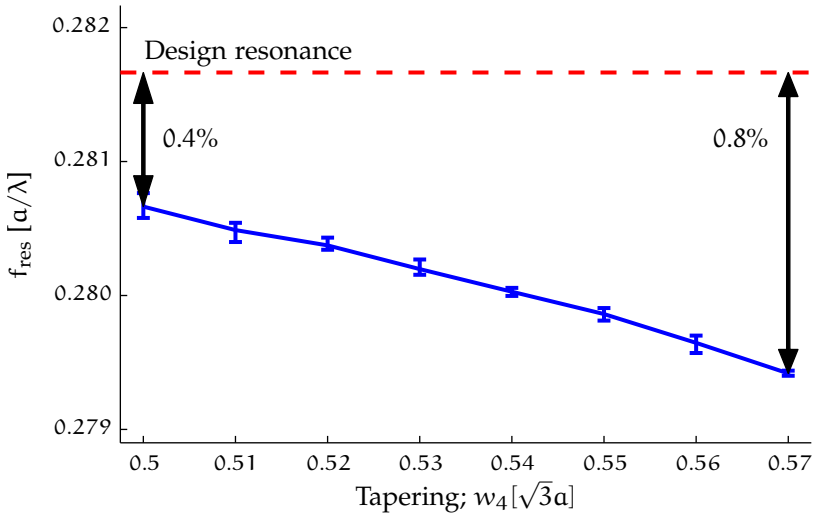

Figure 42: Relative resonance frequency as a function of tapering; the vertical bars around each point indicate maximum deviation over the range of investigated values of boundary width b.

accurate for the cavity illustrated in fig. 35 as it has finite extent and the lattice is not constant due to the perturbations $a_1 \ldots a_4$. This also explains the increased de-tuning of the resonance frequency for increasing w_4 as the change in geometry increases the lattice perturbation. Finally, even though PWEM and FDTD generally converge [113], the choice of parameters can explain small numerical differences between the design resonance as calculated by PWEM and the cavity's resonance as calculated by FDTD.

5.9 GLASS CLAD CAVITY

The previous section has demonstrated that this cavity geometry is capable of providing high Q-factors within a limited geometry when air-clad. However, a more practical implementation would be a cavity buried in SiO_2, i. e. a glass clad cavity. By burying it in SiO_2, the cavity is mechanically protected and stabilised from impact, dust and scratches. It is also possible to integrate it in a layered structure either for 3D integration of circuitry or simply crossing metal interconnects.

The basic parameters chosen for the glass clad cavity are given in table 9. The choice of these parameters follows the same reasoning as for the air-clad cavity (cf. section 5.4.)

For a chosen design resonance frequency of $f_{res} = 0.2828ac^{-1}$, the same method as for the air-clad cavity in section 5.6.1 is

Table 9: Simulation parameters for glass-clad cavity.

Parameter	Symbol	Value
Radius	r	0.346 a
Slab thickness	d	0.6 a
Slab refractive index	n_{slab}	3.48
Cladding/hole refractive index	n_{clad}	1.45

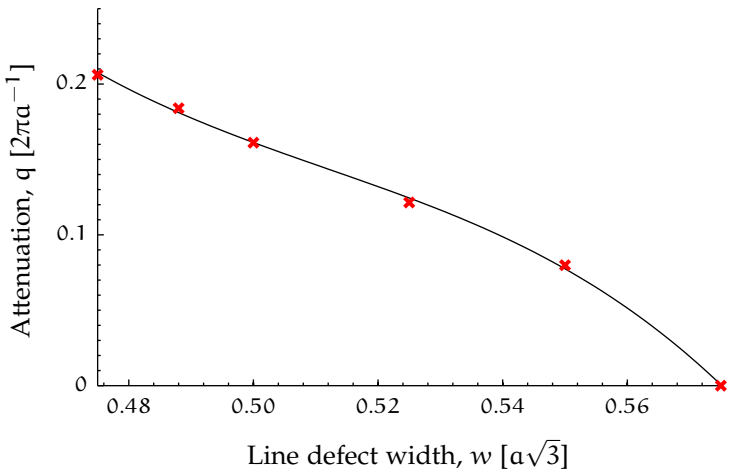

Figure 43: Attenuation as a function of line defect width in a glass clad slab photonic crystal with hexagonal holes.

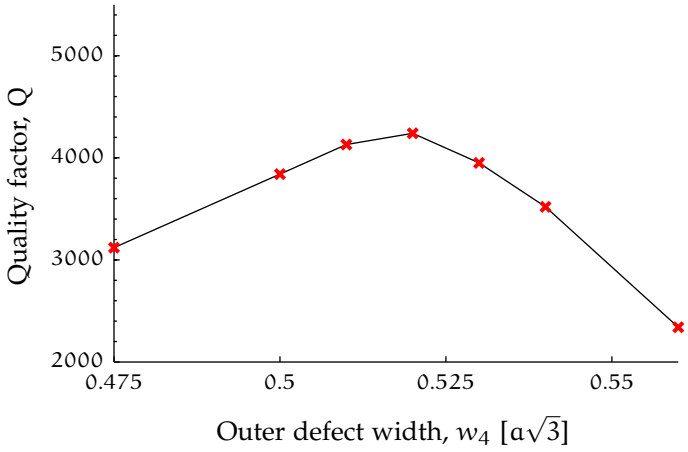

(a)

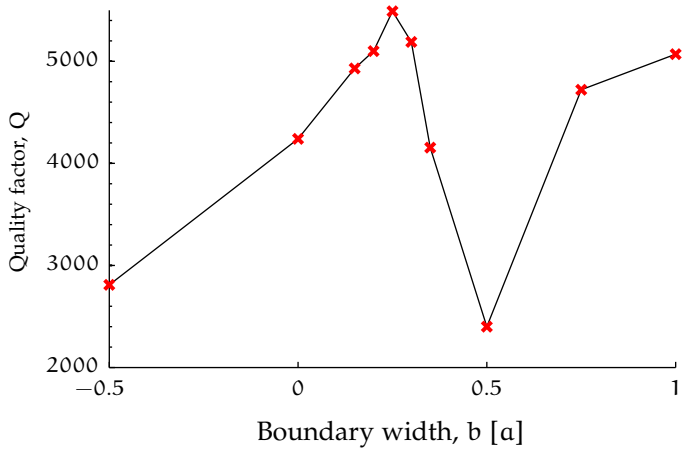

(b)

Figure 44: For a glass clad cavity, (a) dependence of Q on tapering strength w_4 when $b = 0$ and (b) dependence of Q on boundary width b at optimal tapering strength $w_4 = 0.52\sqrt{3}a$.

applied to derive an expression for the attenuation/waveguide-width relationship $q_{glass}(w)$.For $q(w) = 0$, the inner waveguide width $w_0 = 0.575\sqrt{3}a$ is found. Scanning over a range of tapering strengths w_4 with a boundary width $b = 0$ gives the relationship in fig. 44a. This clearly follows the same trend as in the air-clad case of the previous sections. Peak Q is found at $w_4 = 0.52\sqrt{3}a$. At this tapering strength the dependence of Q on b is plotted in fig. 44b. This figure again confirms the trends observed in the previous section with a maxima followed by a minimum followed by an increase in Q as b is increased. Peak Q is found at $b = 0.25a$ with a value of 5490; the minimum is found at $b = 0.5a$.

Compared to the air-clad-case, the Q-factor of the glass-clad case is reduced by more than an order of magnitude. This is as expected since the lower index contrast ($n_{slab} - n_{clad}$) increases the size of the light cone and thereby increases the out-of-plane losses. The reduced index contrast also generally reduces the band-gap size which weakens confinement.

5.9.1 *Mode volume*

Besides Q-factor, the mode volume is an important parameter for micro-cavities due to its significance in lowering the threshold [105] and increasing the modulation speed. [106] For this cavity, we find the mode volume V_m to be largely independent of the optimization parameters w_4 and b. For optimal tapering $w_4 = 0.53\sqrt{3}a$, simulations yield mode volumes of $V_m = 1.40(\lambda/n)^3$ for both optimal boundary $b = 0.25a$ and sub-optimal boundary $b = 0.625a$. For the case of optimal boundary $b = 0.25a$ with sub-optimal tapering $w_4 = 0.56\sqrt{3}a$ the mode volume increases to $V_m = 1.46(\lambda/n)^3$. This slight increase is attributed to to weakened confinement by the heterostructure.

A mode volume of $1.4(\lambda/n)^3$ is relatively large compared to conventional H0, H1 and L3 cavities which can have mode volumes on the order of $0.2{\sim}1(\lambda/n)^3$. [141] It is, however, comparable to line-defect, heterostructure cavities which have reported mode volumes on the order of $1.2{\sim}1.3(\lambda/n)^3$. [130, 137] As such, the compact design does not contribute to the reduction in mode volume, but qualitatively, the mode volume can not be considered too large. This is supported by the fact that this mode volume is on the order of that employed to create both fJb^{-1} photonic crystal lasers [41, 116] and high performance silicon Raman lasers [49] where in both cases Q-factor and small mode volume is essential.

5.10 MODE COMPETITION

When simulating the full cavity, there is one potential issue which arises. The full spectrum calculated based on the $H_\perp$ component of the high Q cavity with $w_4 = 0.53\sqrt{3}a$ and $b = 0.25a$ is shown in fig. 45. This shows that there is are other significant modes within the bandgap. The free spectral range to the closest mode is $\Delta f = -0.005a/\lambda$. When scaled to a resonance around $1.55\,\mu$, this corresponds to an energy difference of $\Delta E = 16\,eV$ which is quite narrow compared to the FWHM

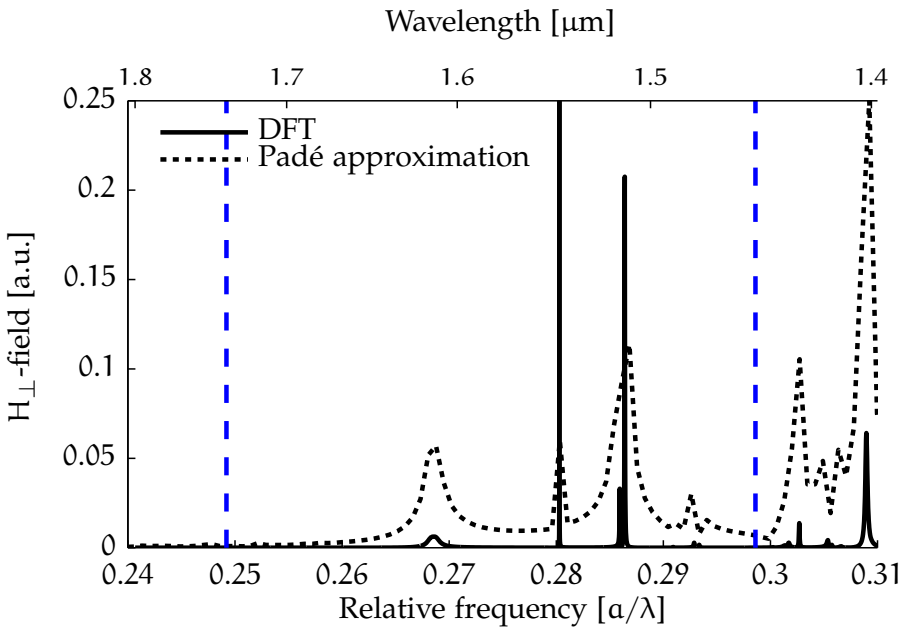

Figure 45: Full spectrum for $H_\perp$ field in high Q cavity shown calculated both with discrete Fourier transform (DFT) and Padé approximation. A TE-like photonic bandgap exists between the dashed blue lines.

of he spontaneous emission from EL for quantum wells. The Q-factor of this mode is one order of magnitude smaller than the design mode, but nonetheless mode competition may become a problem and it must be considered when designing a laser junction and contacts for injection. For TM-like mode, no significant modes were found and need not be considered.

5.11 OUTPUT COUPLING

In order for this cavity to be considered practical, it must be possible to couple it to some external device. As shown in eq. (42), the coupling efficiency η depends solely on the ratio between the the loaded Q-factor Q and the intrinsic Q-factor Q_0. For instance, to achieve $\eta = 80\,\%$ the ratio should be $Q/Q_0 = 0.2$. This gives great flexibility in design, but with a trade off between high-Q and high coupling efficiency. The question is how to achieve this coupling.

In this case we follow the technique used by Faraon et al. [128] with shoulder coupling. Figure 46 shows a disk with 3 arbitrarily chosen output waveguides. With this geometry, the coupling efficiency can be controlled by filling holes in line with the output waveguides. With N as the number of filled

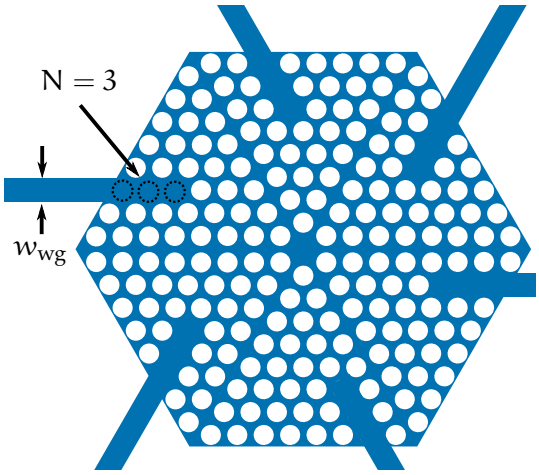

Figure 46: Waveguide coupling concept; here with coupling to six output waveguides with N = 3 holes filled to control the coupling efficiency.

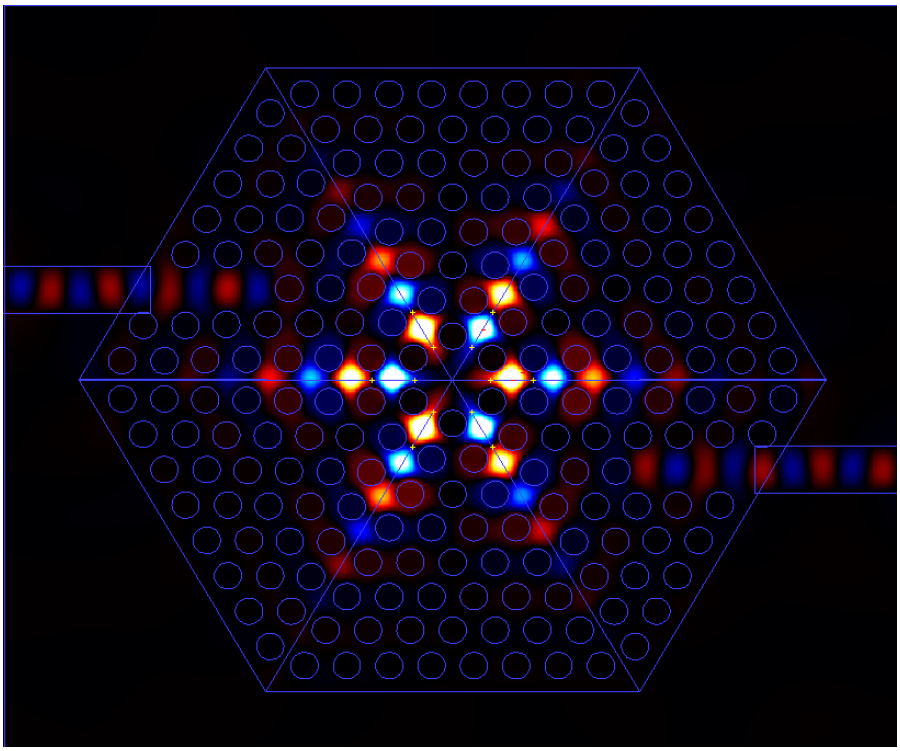

Figure 47: Field distribution ($H_\perp$) when coupling into two waveguides.

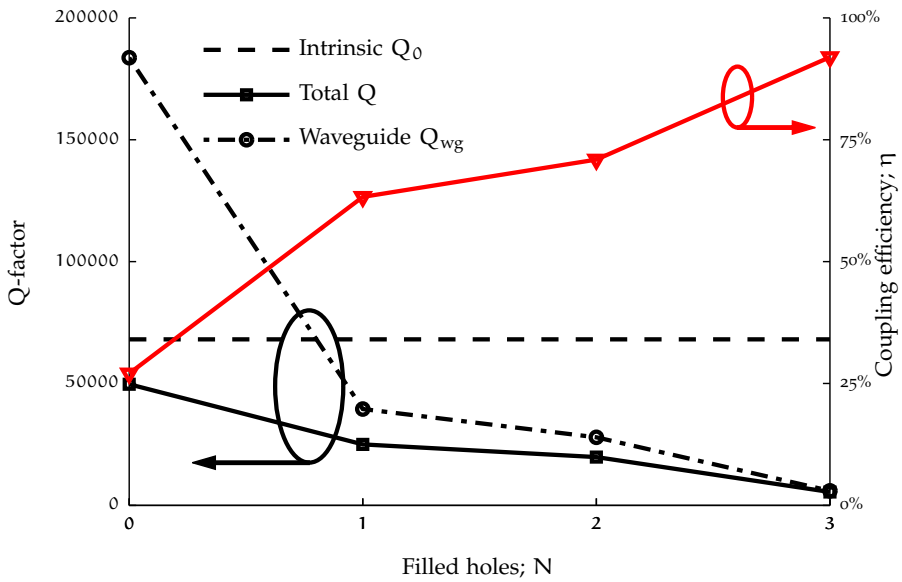

Figure 48: Decomposed Q-factor and accumulated coupling efficiency to six output ports.

holes, the illustration shows the geometry for $N = 3$. Naturally, it is possible to use any arbitrary configuration of waveguides. For the case of two parallel, offset and opposing output waveguides and $N = 3$ fig. 47 shows the field distribution. This qualitatively verifies this method as a valid output coupling strategy.

For a high-Q cavity with $w_4 = 0.54\sqrt{3}a$ and $b = 0.25a$ with an intrinsic $Q_0 = 68\,100$ with six output waveguides of width $w_{wg} = 500\,nm$, changing the number of filled holes N reduces the Q-factor as shown in fig. 48. As can be seen in the figure, merely the introduction of the waveguides without otherwise modifying the cavity reduces the Q factor from 68 100 to 49 700. This is expected since the waveguides represent a new loss path compared to the reflective, high-index contrast boundary between the disk and cladding.

Increasing N increases the coupling efficiency monotonically from 27 % at $N = 0$ to 92 % at $N = 3$. From eq. (41), and as illustrated in fig. 48, this corresponds to an decreasing Q and increasingly dominating Q_{wg}. At $N = 3$, $Q_{wg} \approx 5500$ dominates $Q \approx 6000$.

If only a single waveguide is used, the reduction in Q is not as severe as with six output waveguides. At $N = 3$, coupling to a single waveguide reduces Q to 37 400. This reduction in measured Q-factor corresponds to $Q_{wg} = 83\,000$ and $\eta = 45\,\%$. The difference between this single waveguide case and the six

waveguide case supports that the reduction in Q is due to coupling to the waveguide and that it is not merely due to a perturbation of the lattice inducing losses.

Although these numbers of η are presented as coupling efficiency, they do not necessarily correspond to the coupling efficiency into the fundamental mode of the waveguides. If the PhC extended infinitely in all directions with only a line defect then this number would more accurately represent coupling as light could only propagate along the defect due to the PBG. The only other possible loss factor for reducing Q would be increased out-of-plane losses, but these should be negligible as long as the cavity perturbation is small and conserves the mode profile.

Here, however, we must consider that not all induced losses are coupled into the fundamental mode of the output waveguides. These modes of the output waveguide do not necessarily match the modes of the line defects. Furthermore, at the disk-cladding-waveguide intersection there could be induced scattering losses.

By creating a simple FDTD simulation where a light is coupled from the fundamental mode of a waveguide, into a line defect and then back to another waveguide, the coupling loss from waveguide to PhC line defect is estimated to be $\eta_{\mathrm{PhC}\to\mathrm{wg}} \approx 0.7\,\mathrm{dB} = 0.85$ at the resonant wavelength. As a first approximation, the total coupling efficiency η' would then be

$$\eta' = \eta_{\mathrm{PhC}\to\mathrm{wg}} \cdot \eta = 38\,\%. \tag{52}$$

Considering the argument of section 5.1.3 the achieved Q-factor for the loaded cavity should be sufficient for the implementation of a fJ laser while achieving coupling efficiencies of 30 % and more. However, the glass clad cavity may not be sufficient for this application as its unloaded Q-factor is below that of comparable electrically pumped lasers. [116] Loading it for in-plane extraction of radiation would necessarily further reduce the Q-factor.

6 CONCLUSION

This dissertation has explored two aspects of monolithic on-silicon light sources. Previous works that have established growth of InAs/InGaAs micro disks on (111) silicon by micro selective-area growth using metalorganic chemical vapor deposition. This dissertation expands on this work by the growth of doped InGaAs disks and the fabrication of a near-infrared light emitting diode by contacting ensembles of *pin* InGaAs micro disks. At room temperature, the observed electroluminescence spectrum from these InGaAs micro-disk ensembles shows peak luminescence at 1.78 µm with a local maxima at 1.65 µm. Comparison of individual disks within a single ensemble and considerations of the known band-gap narrowing effect in InGaAs suggest that the long wavelength region stems from recombination in the doped regions of the disks while the shorter wavelength stems from recombination in the un-doped region. As a first approximation, this un-doped region band-gap corresponds to a indium composition of 47% in the intrinsic region.

In addition to electroluminescence, the InGaAs disk ensembles were also shown to have potential as near-infrared (NIR) detectors. Under NIR illumination with wavelengths corresponding to energies smaller than the silicon bandgap energy, a distinct, reproducible photo current was observed. This photo current was quite weak which is attributed to poor collection efficiency and small device area.

These luminescent structures are intended as proof-of-concept for monolithically integrated InGaAs-on-Si micro disk light emitting diodes (LEDs). Further work is required to create practical, efficient devices. It is suggested that wide band-gap barrier layers are necessary to improve carrier confinement. Furthermore, preliminary investigations of disk morphology suggest that the addition of zinc by the use of dimethylzinc (DMZn) precursors has a significant effect on disk thickness.

If optimized, this technology can potentially bring monolithically integrated light sources to silicon photonics as well as provide the basis for low cost InGaAs NIR sensors due to the lower substrate cost and the potential of monolithic integration

of complementary metal-oxide-semiconductor (CMOS) circuitry with InGaAs detectors and light sources.

Having established the possibility of monolithic InGaAs-on-Si disk NIR LED, the challenge of designing a photonic crystal cavity which will fit within the geometrical constraints of the InGaAs-disks is approached by the introduction of a novel photonic crystal cavity. The cavity design is motivated by the limitations imposed by the InGaAs-on-silicon disk's geometry.

The design and optimization shows that for compact photonic crystal cavities in thin photonic slabs, both the out-of-plane loss as well as the in-plane, boundary loss must be considered. To reduce the out-of-plane loss, a gentle confinement method is applied and it is shown that it is effective even when the area is strictly limited and that it can also be applied in a quasi one-sided fashion. For reduction of the in-plane losses, this investigation suggests that a classical Fabry-Pérot model of the boundary region can give a first-order estimate of the optimum boundary width by minimizing Fabry-Pérot transmission. Thus for this photonic crystal cavity (PhCC) design, optimization of Q-factor is a two dimensional problem on w_4 and b where the former is determines the line defect shape and the latter the boundary width. We conclude that it is not necessary to perform exhaustive searches as $Q(w_4, b)$ appears smooth with a maximum within the region of interest. In addition, w_4 is bounded and optimum b can be estimated by trivial calculation making it a prime target for common optimization strategies.

For the case of an air-suspended PhCC with slab refractive index $n_{slab} = 3.48$, full three-dimensional (3D) finite-difference time-domain simulations of the cavity yield a maximum Q-factor of 75 100. For the more practical case of a cavity embedded in glass with $n_{clad} = 1.45$ peak Q-factor was found to be 5490.

One advantage of the developed optimization strategy is that it provides wavelength predictability. That is, resonant wavelength can be chosen during the design stage using only the computationally, relatively cheap plane wave expansion method. Comparison with full cavity simulations using finite-difference time-domain show an error of only 0.5 %

Although the simulations have considered the idealized case of a uniform silicon disk, the presented method should also be applicable to more realistic cases such as InGaAs disks selectively grown on silicon. In addition, the optimization of this cavity has contributed to the understanding of photonic

crystal (PhC) when the area is limited, especially with regards to the importance of the boundary region. Although in some aspects the merits of this design does not compare favourably to other PhCC, it should represent a useful contribution to the zoo of PhCC designs. In the future it may enable the realization of compact, high-Q lasers tightly integrated with silicon photonics for applications such as on-chip optical interconnects.

Successful demonstration of InGaAs-on-silicon micro-disk NIR LEDs and the design of a compact, high-Q PhCCs tailored to these disks promises a new, monolithic approach to on-silicon light sources. Although significant device modelling, growth optimization and process engineering is still required this research is promising for ultimately realizing an on-silicon light source that is compatible with both CMOS electronics and silicon photonics.

6.1 FUTURE WORK

This dissertation has answered two important questions with regards to the possibility for integrating monolithic III/V light sources with silicon photonics. First it has been shown that InGaAs on silicon can be made to exhibits electroluminescence at wavelengths which are interesting for both optical sensing and optical communication. It is also believed that the growth technology is compatible with CMOS electronics.

Secondly, it has been shown that the constraints posed by the limited area of the as-grown InGaAs disks do not present an insurmountable challenge for fabricating advanced photonic crystal cavitys. This is promising as it allows small mode volumes and large Q-factors to be achieved.

However, this is far from sufficient in establishing InGaAs as a clear candidate for monolithic on-silicon light sources. As such, many questions are still unanswered and there are many interesting questions remaining to be answered.

First of all, although electroluminescence (EL) has been demonstrated, the device was not optimized and the efficiency is unclear. One argument against the use of such InGaAs disks is the fact that the device is a homo-junction device. Conventionally, this is regarded as unsuitable for high efficiency light generation due to a lack of carrier confinement. However, careful electrode design combined with a PhC structure can improve confinement as the electric field becomes highly inhomogeneous. Perhaps it could also be possible to insert layers

of GaAs, $In_{1-x}Ga_xAl_yAs_{1-y}$ or $In_{1-x}Ga_xAl_yP_{1-y}$ compounds with larger bandgaps to improve confinement. This is a problem which should be attacked both theoretically and from a practical growth perspective.

There are two other issues conventionally associated with homo-junctions and that is light confinement and re-absorption of emitted light. In a conventional Fabry-Pérot ridge waveguide laser geometry a heterostructure is usually required to confine light to the active region as the refractive index contrast is significantly larger than for homo-junctions. This is however not an issue for PhCC lasers as the PhC structure provides confinement. The second issue of re-absorption may be more significant, but it depends on the overlap between the active region and the mode distribution. Due to the flexible field tailoring of PhCC this issue may reduced by ensuring a large mode overlap with the active region. Quantifying this effect is an outstanding issue.

A

FABRICATION

A.1 GROWTH TEMPLATE FABRICATION

Before micro selective-area growth (μSAG) can be performed, the following procedure is used to to prepare the substrate for growth:

1. oxidation of Si (111) wafer
2. e-beam lithography of growth pattern
3. pattern etching
4. substrate cleaning

A.1.1 *Oxidation*

To prepare the substrate for μSAG, first an oxide layer must be formed. This is done at high temperature in a fused silica furnace with either a (dry) O_2 atmosphere or a (wet) O_2+H_2O atmosphere. According to the Deal-Grove model for oxidation, the time t required to achieve an oxide thickness of X_o follows

$$t \propto X_o^2. \tag{53}$$

This is intuitive since as the oxide layer grows thicker it shields the underlying silicon layer from reacting with the atmosphere. Thus, the growth thickness is an important consideration as a too thick layer would take a prohibitively long time to form. Comparing wet and dry oxidation, wet oxidation is significantly faster, but produces a worse Si/SiO_2 than dry etching. Oxide formed by wet oxidation is also more porous and than that formed by dry oxidation. Both thick and thin oxide layers have been used for the experiments here for which wet and dry oxidation, respectively, has been employed. The dry and wet oxidation conditions are listed in table 10. Dry oxidation for 1 h formed 80 nm SiO_2 layers while wet oxidation for 1 h formed 1.2 μm SiO_2 layers was formed. The thickness variations are attributed to gradients in temperature and atmospheric composition.

Table 10: Oxidation settings

	Wet	Dry
Oxidation temperature	1050 °C	
O_2 flow rate [$l\,h^{-1}$]	2.5	2.5
Hot-plate temperature	110 °C	n.a.

A.1.2 *E-beam lithography*

Next, e-beam lithography is used to form a hexagonal pattern of 1 µm growth channels with a pitch of 10 µm as illustrated in fig. 9. The resist is applied, exposed and developed according to the following recipe:

1. Spin on OEBR CAP positive e-beam resist
   a) 5 s slope to 500 rpm
   b) 5 s at 500 rpm
   c) 5 s slope to 3000 rpm
   d) 60 s at 3000 rpm
2. Spin on Espacer 300AX conductive polymer to prevent charge accumulation
3. Pre-exposure bake for 2 min at 110 °C
4. Exposure in EB-writer with 8 µC cm^{-2} dosage
5. Rinse of Espacer 300AX in DI water
6. Post-exposure bake for 2 min at 110 °C
7. Develop in 2.3 % TMAH for 60 second
8. Rinse two times in DI water
9. Post-bake for 90 s at 110 °C

A.1.3 *Etching*

Next, the growth channels are etched. For thin oxide layers it is sufficient to use wet etching in buffered hydrofluoric acid (BHF) while for thicker layers anisotropic dry etching in inductively coupled plasma reactive-ion etch (ICP-RIE) is required to achieve

vertical growth channels. To avoid micro-trenching of the Si surface, dry etching is terminated before etching through the SiO_2 layers and the etching is finished off with BHF wet etching.

ICP-RIE was carried out on an L-201D-SLA system from Anelva using an Ar/CHF_3 gas mix. For etching of SiO_2 the system conditions were as listed in table 11.

Table 11: Etch condition for Anelva L-201D-SLA ICP-RIE

SiO_2		
Gas pressure	1.0 Pa	
He flow rate	8.0 sccm	(cooling)
Ar flow rate	5.0 sccm	
CHF_3 flow rate	5.0 sccm	
RF power	60 W	
Bias power	25 W	
Ashing		
Gas pressure	1.0 Pa	
He flow rate	8.0 sccm	(cooling)
O_2 flow rate	10.0 sccm	
RF power	200 W	
Bias power	0 W	

For wet etching, undiluted BHF63 was used giving an etch rate of approximately $1.1\,nm\,s^{-1}$.

A.2 GROWTH TEMPLATE CLEANING

Cleaning of the growth templates serves two purposes. To remove contaminants, especially organic, and to remove the thin native oxide layer which forms on the surface of bare Si when exposed to air.

1. 3 min in acetone with ultrasonic excitation
2. Rinse in isopropyl alcohol (IPA) followed by DI
3. 10 min in 3 : 1 H_2SO_4:H_2O_2 at 140 °C
4. Rinse twice in separate DI beakers
5. 10 min rinse under running DI
6. 40 s in BHF diluted in water to 0.5 %

7. Double rinse in DI, keep in third DI beaker
8. Blow dry with N_2 in direction avoiding contamination

After cleaning, the samples should be kept in a clean container and placed in N_2 atmosphere as soon as possible (i. e. glove-box of MOCVD system.) This cleaning procedure should in principle be performed as close as possible to growth to prevent native oxide forming on the Si surface. In practice, it has been successfully applied one day prior to growth.

A.3 ENSEMBLE DIODE PROCESSING

Fabrication of the diode ensembles followed the following outline of steps:

1. Isolation of ensembles and removal of polycrystalline growths
2. Planarization by spin-on-glass (SOG)
3. Electrode fabrication by lift-off

A.3.1 *Isolation of ensembles and removal of polycrystalline growth*

1. Spin on AZ5214E negative photoresist.
   a) 5 s at 500 rpm.
   b) 5 s slope to 3000 rpm.
   c) 60 s at 3000 rpm.
2. Pre-exposure bake for 60 s at 90 °C.
3. Expose isolation pattern for 3 s.
4. Inversion bake for 120 s at 120 °C.
5. Flood exposure of resist for 7 s.
6. Develop for 60 s in NMD-3 followed by two rinses in DI water.
7. Etch back resist using ICP-RIE ashing recipe in table 11.
   - Approximately 7.5 min.
   - Inspect using optical microscope and re-etch as necessary.

8. Wet etch in 1:15:30 (96 %)H_2SO_4:(30 %)H_2O_2:H_2O for 2 min.
   - Inspect using optical microscope.
   - If a significant number of polycrystalline islands remains, then return to step 7 to further reduce the resist thickness followed by further wet etching.

A.3.2 *Planarization with SOG*

1. Spin on OCD T12 SOG
   a) 5 s slope to 2000 rpm
   b) 30 s at 2000 rpm
2. Bake for 2 min at 80 °C on hot-plate
3. Bake for 2 min at 200 °C on hot-plate
4. Repeat the preceding three steps two more times to form three layers of SOG.
5. Cure for 30 min at 300 °C in N_2 atmosphere.
6. Etch back SiO_2 cover to expose top of islands.
   a) Use Anelva L-201D-SLA ICP-RIE with SiO_2 conditions in table 11.
   b) Etch for 15 min
   c) Inspect using optical microscopy and continue etching if required.
      - Reflection from the islands increases significantly when all SOG has been removed.

A.3.3 *Lift-off metallization*

1. Spin on AZ5214E negative photoresist.
   a) 5 s at 500 rpm.
   b) 5 s slope to 3000 rpm.
   c) 60 s at 3000 rpm.
2. Pre-exposure bake for 60 s at 90 °C.
3. Expose isolation pattern for 3 s.

4. Inversion bake for 120 s at 120 °C.
5. Flood exposure of resist for 7 s.
6. Develop for 60 s in NMD-3 followed by two rinses in DI water.
7. Mount sample in Ulvac electron beam (EB) evaporator
8. Evaporate 10 nm/15 nm/80 nm/300 nm of Pt/Ti/Pt/Au.
9. Place sample in Aceton for several hours.
10. For improved liftoff use 1 min in ultrasonic bath at room temperature.
11. After all gold covered resist has been stripped away, rinse two times in IPA
12. Cover sample with Microprosit S1800 resist for protection.
    - Conditions non-critical
13. Mount sample upside down in thermal evaporator.
14. Evaporate 300 nm of aluminium on the *n*-Si backside
15. Clean off protective resist from sample top-side

After these steps, the sample can be mounted on copper plates using conductive silver paste and contacted using micro probes. They can also be wire bonded if care is taken, but for such purposes a thicker gold layer is recommended.

[9] J. Harrison, "Opal from yowah, queensland, australia," (2009), creative Commons Attribution-Share Alike 2.5 Generic license.

[10] M. Lipson, J. Lightwave Technol. **23**, 4222 (2005).

[11] R. Soref, IEEE J. Sel. Top. Quantum Electron. **12**, 1678 (2006).

[12] B. Jalali and S. Fathpour, J. Lightwave Technol. **24**, 4600 (2006).

[13] R. Soref, Silicon **2**, 1 (2010).

[14] S. Feng, T. Lei, H. Chen, H. Cai, X. Luo, and A. Poon, Laser & Photonics Reviews **6**, 145 (2012).

[15] J. Doylend and A. Knights, Laser Photon. Rev. **6**, 504 (2012).

[16] M. A. Green, J. Zhao, A. Wang, P. J. Reece, and M. Gal, Nature **412**, 805 (2001).

[17] A. Shakoor, R. Lo Savio, P. Cardile, S. L. Portalupi, D. Gerace, K. Welna, S. Boninelli, G. Franzó, F. Priolo, T. F. Krauss, M. Galli, and L. O'Faolain, Laser Photon. Rev. **7**, 114 (2013).

[18] A. Shakoor, R. Lo Savio, P. Cardile, S. L. Portalupi, D. Gerace, K. Welna, S. Boninelli, G. Franzó, F. Priolo, T. F. Krauss, M. Galli, and L. O'Faolain Proc. SPIE **8629**, 862918–862918–6 (2013).

[19] J. Emsley, *Nature's building blocks: an A-Z guide to the elements* (Oxford Univ. Press, 2001).

[20] M. Bass, C. DeCusatis, J. Enoch, V. Lakshminarayanan, G. Li, C. Macdonald, V. Mahajan, and E. Van Stryland, *Handbook of Optics, Third Edition Volume I: Geometrical and Physical Optics, Polarized Light, Components and Instruments(Set)*, 3rd ed. (McGraw-Hill, Inc., New York, NY, USA, 2010).

[21] M. Bruel, Electron. Lett. **31**, 1201 (1995).

[22] G. T. Reed and A. P. Knights, "Silicon-On-Insulator (SOI) Photonics," in *Silicon Photonics* (John Wiley & Sons, Ltd, 2005) pp. 57–110.

[23] C. Gunn, IEEE Micro **26**, 58 (2006).

[24] L. Kimerling, D. Ahn, A. Apsel, M. Beals, D. Carothers, Y.-K. Chen, T. Conway, D. Gill, M. Grove, C.-Y. Hong, *et al.*, in *Integrated Optoelectronic Devices 2006* 2006 pp. 612502–612502.

[25] Y. Vlasov, IEEE Commun. Mag. **50**, s67 (2012).

[26] University of Delaware, "OpSIS - Silicon Photonics Foundry Service," Retrieved December 2013.

[27] "ePIXfab - Silicon Photonics Foundry Service," Retrieved December 2013.

[28] P. Dumon, W. Bogaerts, R. Baets, J.-M. Fedeli, and L. Fulbert, Electron. Lett. **45**, 581 (2009).

[29] M. Hochberg and T. Baehr Jones, Nature Photon. **4**, 492 (2010).

[30] T. Baehr Jones, R. Ding, A. Ayazi, T. Pinguet, M. Streshinsky, N. Harris, J. Li, L. He, M. Gould, Y. Zhang, A. E.-J. Lim, T.-Y. Liow, S. H.-G. Teo, G.-Q. Lo, S. Ocheltree, C. Hill, A. Pomerene, P. De Dobbelaere, A. Mekis, and M. Hochberg, Proc. SPIE 8252 , 82520G (2012).

[31] M. Hochberg, N. Harris, Ran Ding, Yi Zhang, A. Novack, Zhe Xuan, and T. Baehr Jones, IEEE Solid-State Circuits Mag. **5**, 48 (2013).

[32] Jeff Hecht, *City of Light*, exp. ed. ed. (Oxford University Press, 2004) p. 368.

[33] Wolfgang Briglauer and Klaus Gugler, Telecommun. Policy **37**, 819 (2013).

[34] C. Lam, Hong Liu, B. Koley, Xiaoxue Zhao, V. Kamalov, and V. Gill, IEEE Comm. Mag. **48**, 32 (2010).

[35] C. Kachris and I. Tomkos, IEEE Commun. Surveys Tuts. **14**, 1021 (2012).

[36] Paul Rosenberg, Sagi Mathai, Wayne V. Sorin, Moray McLaren, Joseph Straznicky, Georgios Panotopoulos, David Warren, Terry Morris, and Michael R. T. Tan, J. Lightwave Technol. **30**, 590 (2012).

[37] J. Matsui, T. Yamamoto, K. Tanaka, T. Ikeuchi, S. Ide, S. Aoki, T. Aoki, T. Ishihara, M. Iwaya, K. Kamoto, K. Suematsu, and M. Shiino, in *Optical Fiber Communication Conference and Exposition and the National Fiber Optic Engineers Conference* (2012) pp. 1–3.

[38] Michael R. Tan, Paul Rosenberg, Georgios Panotopoulos, Moray Mclaren, Wayne Sorin, S. MATHAI, Lennie Kiyama, Joseph Straznicky, and David Warren, in *Optical Fiber Communication Conference*, 2014 p. M3E.3.

[39] D. Miller, Proc. IEEE **88**, 728 (2000).

[40] Katharine Schmidtke, Frank Flens, Alex Worrall, Richard Pitwon, Felix Betschon, Tobias Lamprecht, and Roger Krähenbühl, J. Lightwave Technol. **31**, 3970 (2013).

[41] Masaya Notomi, Kengo Nozaki, Akihiko Shinya, Shinji Matsuo, and Eiichi Kuramochi, Opt. Commun. **314**, 3 (2014).

[42] B. E. A. Saleh and M. C. Teich, *Fundamentals of Photonics*, 2nd ed. (Wiley-Interscience, New Jersey, 2007).

[43] Ricardo Claps, Dimitri Dimitropoulos, Yan Han, and Bahram Jalali, Opt. Express **10**, 1305 (2002).

[44] R. Claps, V. Raghunathan, D. Dimitropoulos, and B. Jalali, Opt. Express **11**, 2862 (2003).

[45] Ozdal Boyraz and Bahram Jalali, Opt. Express **12**, 5269 (2004).

[46] H. Rong, A. Liu, R. Jones, O. Cohen, D. Hak, R. Nicolaescu, A. Fang, and M. Paniccia, Nature **433**, 292 (2005).

[47] H. Rong, R. Jones, A. Liu, O. Cohen, D. Hak, A. Fang, and M. Paniccia, Nature **433**, 725 (2005).

[48] H. Rong, S. Xu, Y.-H. Kuo, V. Sih, O. Cohen, O. Raday, and M. Paniccia, Nature Photon. **1**, 232 (2007).

[49] Y. Takahashi, Y. Inui, M. Chihara, T. Asano, R. Terawaki, and S. Noda, Nature **498**, 470 (2013).

[50] Y. H. Lo, R. Bhat, D. M. Hwang, C. Chua, and C. Lin, Appl. Phys. Lett. **62**, 1038 (1993).

[51] H. Wada and T. Kamijoh, IEEE Photon. Technol. Lett. **8**, 173 (1996).

[52] Hyundai Park, Alexander Fang, Satoshi Kodama, and John Bowers, Opt. Express **13**, 9460 (2005).

[53] A. W. Fang, H. Park, O. Cohen, R. Jones, M. J. Paniccia, and J. E. Bowers, Opt. Express **14**, 9203 (2006).

[54] J. Bowers, D. Liang, A. Fang, H. Park, R. Jones, and M. Paniccia, Opt. Photon. News **21**, 28 (2010).

[55] Y. Halioua, A. Bazin, P. Monnier, T. J. Karle, G. Roelkens, I. Sagnes, R. Raj, and F. Raineri, Opt. Express **19**, 9221 (2011).

[56] B. Ben Bakir, A. Descos, N. Olivier, D. Bordel, P. Grosse, E. Augendre, L. Fulbert, and J. M. Fedeli, Opt. Express **19**, 10317 (2011).

[57] M. J. Paniccia, Optik & Photonik **6**, 34 (2011).

[58] J. Michel, J. Liu, and L. C. Kimerling, Nature Photon. **4**, 527 (2010).

[59] R. E. Camacho Aguilera, Y. Cai, N. Patel, J. Bessette, M. Romagnoli, L. C. Kimerling, and J. Michel, Opt. Express **20**, 11316 (2012).

[60] M. Sugo, H. Mori, Y. Sakai, and Y. Itoh, Appl. Phys. Lett. **60**, 472 (1992).

[61] Z. Mi, J. Yang, P. Bhattacharya, and D. Huffaker, Electron. Lett. **42**, 121 (2006).

[62] L. Cerutti, J. B. Rodriguez, and E. Tournie, IEEE Photon. Technol. Lett. **22**, 553 (2010).

[63] Ting Wang, Huiyun Liu, Andrew Lee, Francesca Pozzi, and Alwyn Seeds, Opt. Express **19**, 11381 (2011).

[64] R. Chen, T.-T. D. Tran, K. W. Ng, W. S. Ko, L. C. Chuang, F. G. Sedgwick, and C. Chang Hasnain, Nature Photon. **5**, 170 (2011).

[65] L. C. Chuang, F. G. Sedgwick, R. Chen, W. S. Ko, M. Moewe, K. W. Ng, T.-T. D. Tran, and C. Chang-Hasnain, Nano Lett. **11**, 385 (2011).

[66] T. Hoshii, M. Deura, M. Shichijo, M. Sugiyama, S. Sugahara, M. Takenaka, Y. Nakano, and S. Takagi, in *International Conference on Solid State Devices and Materials* (Business Center for Academic Societies, 2007) pp. 132–133.

[67] T. Hoshii, M. Deura, M. Sugiyama, R. Nakane, S. Sugahara, M. Takenaka, Y. Nakano, and S. Takagi, Phys. Status Solidi C **5**, 2733 (2008).

[68] Momoko Deura, Takuya Hoshii, Mitsuru Takenaka, Shinichi Takagi, Yoshiaki Nakano, and Masakazu Sugiyama, J. Cryst. Growth **310**, 4768 (2008).

[69] M. Deura, T. Hoshii, M. Takenaka, S. Takagi, Y. Nakano, and M. Sugiyama, IEEE International Conference on Indium Phosphide and Related Materials **1**, 48 (2009).

[70] Momoko Deura, Takuya Hoshii, Takahisa Yamamoto, Yuichi Ikuhara, Mitsuru Takenaka, Shinichi Takagi, Yoshiaki Nakano, and Masakazu Sugiyama, Appl. Phys. Express **2**, 011101 (2009).

[71] Yoshiyuki Kondo, Momoko Deura, Yuki Terada, Takuya Hoshii, Mitsuru Takenaka, Shinichi Takagi, Yoshiaki Nakano, and Masakazu Sugiyama, J. Cryst. Growth **312**, 1348 (2010).

[72] M. Deura, Y. Kondo, M. Takenaka, S. Takagi, Y. Nakano, and M. Sugiyama, J. Cryst. Growth **312**, 1353 (2010).

[73] M. Deura, Y. Kondo, M. Takenaka, S. Takagi, Y. Shimogaki, Y. Nakano, and M. Sugiyama, Jpn. J. Appl. Phys. **50**, 04DH07 (2011).

[74] M. Sugiyama, Y. Kondo, M. Takenaka, S. Takagi, and Y. Nakano, J. Cryst. Growth **352**, 229 (2012).

[75] M. E. Groenert, C. W. Leitz, A. J. Pitera, V. Yang, H. Lee, R. J. Ram, and E. A. Fitzgerald, J. Appl. Phys. **93**, 362 (2003).

[76] Andrew Lee, Qi Jiang, Mingchu Tang, Alwyn Seeds, and Huiyun Liu, Opt. Express **20**, 22181 (2012).

[77] Masakazu Sugiyama, Ho-jin Oh, Yoshiaki Nakano, and Yukihiro Shimogaki, Journal of Crystal Growth **261**, 411 (2004).

[78] S. Watanabe, K. Watanabe, A. Higo, M. Sugiyama, and Y. Nakano, Int. Conf. InP Related Mat., 133 (2012).

[79] H. Momose, T. Ohguro, S. Nakamura, Y. Toyoshima, H. Ishiuchi, and H. Iwai, IEEE Transactions on Electron Devices **49**, 1597 (2002).

[80] Min Yang, E. Gusev, MeiKei Ieong, O. Gluschenkov, D. Boyd, K. K. Chan, P. Kozlowski, C. D'Emic, R. Sicina, P. Jamison, and A. Chou, IEEE Electron Device Lett. **24**, 339 (2003).

[81] J. Knickerbocker, P. Andry, B. Dang, R. R. Horton, C. Patel, R. Polastre, K. Sakuma, E. S. Sprogis, C. Tsang, B. Webb, and S. Wright, *58th Electronic Components and Technology Conference*, 538 (2008).

[82] J. M. Fedeli, L. Di Cioccio, D. Marris Morini, L. Vivien, R. Orobtchouk, P. Rojo Romeo, C. Seassal, and F. Mandorlo, Adv. Opt. Techn. **2008**, 15 (2008).

[83] A. Franke, D. Bilic, D. T. Chang, P. T. Jones, T.-J. King, R. Howe, and G. Johnson, *Twelfth IEEE International Conference on Micro Electro Mechanical Systems*, 630 (1999).

[84] S. Sedky, A. Witvrouw, H. Bender, and K. Baert, IEEE Trans. Electron Dev. **48**, 377 (2001).

[85] C. A. Schneider, W. S. Rasband, and K. W. Eliceiri, Nat Meth **9**, 671 (2012).

[86] J. S. Yu, S. Kim, and T. Kim, in *IEEE International Symposium on Compound Semiconductors, 1997* (1998) pp. 175–178.

[87] S. C. Jain, J. M. McGregor, and D. J. Roulston, J. Appl. Phys. **68**, 3747 (1990).

[88] K.-H. Goetz, D. Bimberg, H. Jürgensen, J. Selders, A. V. Solomonov, G. F. Glinskii, and M. Razeghi, J. Appl. Phys. **54**, 4543 (1983).

[89] H.-Y. Ryu, H.-S. Kim, and J.-I. Shim, Appl. Phys. Lett. **95**, 081114 (2009).

[90] S. Watanabe, *Characterization of Crystalline and Electrical Conduction Property of InAs, InGaAs on Si(111) for Monolithic Infrared Photodetectors*, Master's thesis, The University of Tokyo (2013).

[91] L. Rayleigh, Philosophical Magazine Series 5 **24**, 145 (1887).

[92] L. Rayleigh, Philosophical Magazine Series 5 **26**, 256 (1888).

[93] Eli Yablonovitch, Optics and photonics news **18**, 12 (2007).

[94] E. Yablonovitch, Phys. Rev. Lett. **58**, 2059 (1987).

[95] S. John, Phys. Rev. Lett. **58**, 2486 (1987).

[96] J. D. Joannopoulos, S. G. Johnson, J. N. Winn, and R. D. Meade, *Photonic Crystals: Molding the Flow of Light (Second Edition)*, 2nd ed. (Princeton University Press, 2008).

[97] F. Bloch, Zeitschrift für Physik **52**, 555 (1929).

[98] Charles Kittel, *Introduction to Solid State Physics*, 8th ed. (Wiley, 2005) p. 680.

[99] S. Noda, K. Tomoda, N. Yamamoto, and A. Chutinan, Science **289**, 604 (2000) .

[100] S. A. Rinne, F. Garcia Santamaria, and P. V. Braun, Nature Photon. **2**, 52 (2008).

[101] K. Aoki, D. Guimard, M. Nishioka, M. Nomura, S. Iwamoto, and Y. Arakawa, nature photonics **2**, 688 (2008).

[102] Bong-Shik Song, Takashi Asano, and Susumu Noda, New J. Phys. **8**, 209 (2006).

[103] J. Vučković, M. Lončar, H. Mabuchi, and A. Scherer, Phys. Rev. E **65**, 016608 (2001).

[104] T. Yoshie, A. Scherer, J. Hendrickson, G. Khitrova, H. M. Gibbs, G. Rupper, C. Ell, O. B. Shchekin, and D. G. Deppe, Nature **432**, 200 (2004).

[105] Susumu Noda, J. Opt. Soc. Am. B **27**, B1 (2010).

[106] D. Englund, H. Altug, B. Ellis, and J. Vučkovič, Laser Photon. Review **2**, 264 (2008).

[107] O. Painter, R. K. Lee, A. Scherer, A. Yariv, J. D. O'Brien, P. D. Dapkus, and I. Kim, Science **284**, 1819 (1999) .

[108] M. Seo, K. Jeong, J. Yang, Y. Lee, H. Park, and S. Kim, Appl. Phys. Lett. **90**, 171122 (2007).

[109] B. Ellis, M. A. Mayer, G. Shambat, T. Sarmiento, J. Harris, E. E. Haller, and J. Vučkovič, Nature Photon. **5**, 297 (2011).

[110] Shinji Matsuo, Koji Takeda, Tomonari Sato, Masaya Notomi, Akihiko Shinya, Kengo Nozaki, Hideaki Taniyama, Koichi Hasebe, and Takaaki Kakitsuka, Opt. Express **20**, 3773 (2012).

[111] K. M. Ho, C. T. Chan, and C. M. Soukoulis, Phys. Rev. Lett. **65**, 3152 (1990).

[112] D. Prather, *Photonic Crystals, Theory, Applications and Fabrication*, Wiley Series in Pure and Applied Optics (Wiley, 2009).

[113] Shouyuan Shi, Caihua Chen, and Dennis W. Prather, J. Opt. Soc. Am. A **21**, 1769 (2004).

[114] Kane Yee, IEEE Trans. Antennas Propag. **14**, 302 (1966).

[115] Wei-Hua Guo, Wei-Jun Li, and Yong-Zhen Huang, IEEE Microw. Wireless Compon. Lett. **11**, 223 (2001).

[116] K. Takeda, T. Sato, A. Shinya, K. Nozaki, W. Kobayashi, H. Taniyama, M. Notomi, K. Hasebe, T. Kakitsuka, and S. Matsuo, Nature Photon. **7**, 569 (2013).

[117] Yinan Zhang, Christoph Hamsen, Jennifer T. Choy, Yong Huang, Jae-Hyun Ryou, Russell D. Dupuis, and Marko Loncar, Opt. Lett. **36**, 2704 (2011).

[118] J. Zhang, D. Chu, S. Wu, W. G. Bi, R. Tiberio, R. M. Joseph, A. Taflove, C. Tu, and S.-T. Ho, IEEE Photon. Tech. Lett. **8**, 491 (1996).

[119] Qimin Quan, Parag B. Deotare, and Marko Loncar, Appl. Phys. Lett. **96**, 203102 (2010).

[120] S.-H. Kim, A. Homyk, S. Walavalkar, and A. Scherer, Phys. Rev. B **86**, 245114 (2012).

[121] Se-Heon Kim, Jingqing Huang, and Axel Scherer, Opt. Lett. **37**, 488 (2012).

[122] A.-J. Lim, Junfeng Song, Qing Fang, Chao Li, Xiaoguang Tu, Ning Duan, Kok Kiong Chen, R.-C. Tern, and Tsung-Yang Liow, IEEE J. Sel. Top. Quantum Electron. **20**, 405 (2014).

[123] Dirk Englund, Hatice Altug, and Jelena Vučkovič, Appl. Phys. Lett. **91**, 071124 (2007).

[124] E. M. Purcell (1946) pp. 681+.

[125] J.-M. Gerard and B. Gayral, J. Lightwave Technol. **17**, 2089 (1999).

[126] Chi-Yu Adrian Ni and Shun Lien Chuang, Opt. Express **20**, 16450 (2012).

[127] Guk-Hyun Kim, Yong-Hee Lee, Akihiko Shinya, and Masaya Notomi, Opt. Express **12**, 6624 (2004).

[128] Andrei Faraon, Edo Waks, Dirk Englund, Ilya Fushman, and Jelena Vučković, Appl. Phys. Lett. **90**, 073102 (2007).

[129] Myung-Ki Kim, Amit M. Lakhani, and Ming C. Wu, Opt. Express **19**, 23504 (2011).

[130] Yoshinori Tanaka, Takashi Asano, and Susumu Noda, J. Lightwave Technol. **26**, 1532 (2008).

[131] S. G. Johnson, S. Fan, P. R. Villeneuve, J. D. Joannopoulos, and L. A. Kolodziejski, Phys. Rev. B **60**, 5751 (1999).

[132] O. Sigmund and J. Søndergaard Jensen, Philosophical Transactions of the Royal Society of London. Series A:Mathematical, Physical and Engineering Sciences **361**, 1001 (2003).

[133] O. Sigmund and K. Hougaard, Phys. Rev. Lett. **100**, 153904 (2008).

[134] Kartik Srinivasan and Oskar Painter, Opt. Express **10**, 670 (2002).

[135] J. Vučkovič, M. Loncar, H. Mabuchi, and A. Scherer, IEEE J. Quantum Electron. **38**, 850 (2002).

[136] Y. Akahane, T. Asano, B.-S. Song, and S. Noda, Nature **425**, 944 (2003).

[137] K. Welna, S. Portalupi, M. Galli, L. O'Faolain, and T. Krauss, IEEE J. Quantum Electron. **48**, 1177 (2012).

[138] Masaya Notomi and Hideaki Taniyama, Opt. Express **16**, 18657 (2008).

[139] S. Matsuo, A. Shinya, T. Kakitsuka, K. Nozaki, T. Segawa, T. Sato, Y. Kawaguchi, and M. Notomi, Nature Photon. **4**, 648 (2010).

[140] E. Istrate, A. A. Green, and E. H. Sargent, Phys. Rev. B **71**, 195122 (2005).

[141] S. Nakayama, S. Ishida, S. Iwamoto, and Y. Arakawa, Appl. Phys. Lett. **98**, 171102 (2011).